

EXCALIBRATE

Calibration for astrophysical experimentation



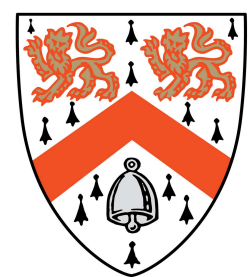
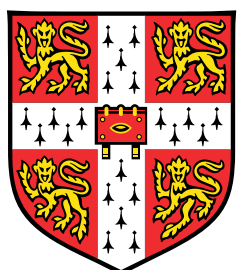
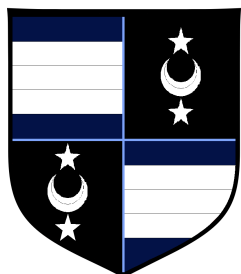
Ian Laurent Van Roque

Department of Physics
University of Cambridge

This dissertation is submitted for the degree of
Doctor of Philosophy

Wolfson College

December 2023



I would like to dedicate this thesis to my loving parents ...

Declaration

I hereby declare that except where specific reference is made to the work of others, the contents of this dissertation are original and have not been submitted in whole or in part for consideration for any other degree or qualification in this, or any other university. This dissertation is my own work and contains nothing which is the outcome of work done in collaboration with others, except as specified in the text and Acknowledgements. This dissertation contains fewer than 60,000 words including summary/abstract, tables, footnotes and appendices.

Ian Laurent Van Roque
December 2023

Acknowledgements

And I would like to acknowledge ...

Abstract

This is where you write your abstract ...

Table of contents

1	Introduction	1
1.1	21-cm astrophysics	2
1.2	The EDGES experiment	5
1.3	The REACH experiment	8
2	Receiver design and development	11
2.1	The REACH receiver	11
2.1.1	Receiver front-end	12
2.1.2	Receiver back-end	40
2.1.3	Automation	50
2.1.4	Deployment	55
3	Receiver calibration	59
3.1	Calibration formalism	60
3.2	Bayesian parameter derivation	63
4	Results	69
4.1	Preliminary laboratory measurements	70
4.2	Results with simulated data	72
4.2.1	Correlation between noise wave parameters	73
4.2.2	Constraints with additional calibrators	75
4.2.3	Optimisation of individual noise wave parameters	75
4.2.4	Application with realistic noise	77
4.2.5	Waiting for REACH: Results with a HERA receiver	79
4.2.6	REACH Results?	83
4.3	Responses	87
4.4	Additional models for incorporation	90
4.4.1	Fixture compensation to improve S-parameter measurements	90

4.4.2	Temperature gradients across calibration cables	93
4.4.3	Temperature gradients across the antenna	94
4.5	Comparison with least squares algorithm	95
4.5.1	Averaging results to bring the noise down	96
4.6	A frequency-by-frequency Bayesian solver	99
5	Conclusions	103
5.1	Future work	104
References		109
Appendix A Supplementary Data		117

Chapter 1

Introduction

Only a year after its invention in 1608, the optical device known as the telescope was first pointed to the sky [17]. In the four hundred years since, the tool has not only been the driver of astronomical research but epitomises the field and its achievements. Aided by the finite speed of light, our place in the Universe is contextualised through glimpses into the past, revealing galaxies up to eight billion years old in the visible spectrum. As we approach the limits of optical telescopes, novel methods of astrophysical observation are for continued advancements in our understanding of the cosmos. One such method is the employment of an instrument used to study information encapsulated in electromagnetic waves beyond the visible regime; the radio telescope [65].

Over the past century, astronomers have pieced together the chronology of the Universe with surveys such as the Hubble Ultra Deep Field which has unveiled galaxies nearly 13 billion years old [10]. Follow-up measurements reveal more information and even older structures using data at longer wavelengths such as the infrared [9] as the wavelength of light from the oldest structures stretches with the expansion of the universe. This phenomenon is known as ‘redshift’ and relates the wavelength of an observed signal to its original wavelength when emitted in the distant past

$$1 + z = \frac{\lambda_{\text{obsv}}}{\lambda_{\text{emit}}}, \quad (1.1)$$

where z is the dimensionless redshift quantity while λ_{obsv} and λ_{emit} represent the signal’s wavelength at the time of observation and creation respectively. Redshift can be related to the extent of universal expansion to show the ages of objects in the sky and it can be shown that information from the earliest stars and galaxies have redshifted out the regime of visible light and into lower wavelengths. Thus, probing the deepest cosmic questions such as the development of galaxies within the first billion years of our Universe requires the use of low-frequency techniques [39].

Since the 1930's, radio telescopes have remained one of the most exciting research areas in contemporary astronomy with their potential to explore the first hundreds of millions of years after the Big Bang through observation of redshifted signals. By the 1950's it was understood that being the most abundant material in the Universe, study of hydrogen's interactions with astrophysical phenomena would trace the bulk evolution of the cosmos as a whole, especially during periods where there is no visible light to be seen such as before the first stars. While the ultimate goal of current experimentation would be to analyse images of primordial hydrogen [35, 57], the limitations of current technology restrict us to an interim objective of spectral measurements from the early universe. An essential tool for astronomers hoping to examine this time period would be to take advantage of hydrogen's finicky preference for specific wavelengths of light (particularly those with a wavelength of 21 centimetres), which manifest as minute changes in temperature profiles where energy is absorbed or released by hydrogen.

1.1 21-cm astrophysics

Following recombination, remnant photons from the Big Bang pervaded the Universe having escaped the frenzied soup of electrons now confined into neutral hydrogen atoms held together in gaseous form [60]. In the present day, the expansion of the Universe has stretched the wavelengths of these relic photons out of the visible spectrum and into microwave frequencies which have been measured as the cosmic microwave background (CMB)^a. These hydrogen atoms interact restrictively with the CMB via photons of wavelength equal to 21 centimetres [68]. Hydrogen atoms absorb these 21-cm photons and gain their energy causing the orientation of ground state electrons to flip relative to their associated nuclei [38]. This marginally higher-energy hydrogen atom is said to be in an 'excited' state compared to its natural orientation.

Initially, the transfer of electrons between the neutral hydrogen gas and the CMB was in equilibrium preserving the CMB spectra predicted by the Planck formula at radio frequencies. During this time, the orientation of electrons in hydrogen atoms, also referred to as the spin state, were continuously swapped in equal proportion. For every 21-cm photon absorbed by the CMB, another was emitted by some nearby hydrogen atom as it decays from an excited state. Soon afterwards but before the existence of the first stars, hydrogen atoms in dense pockets collide to temporarily form hydrogen molecules in a process known as collisional coupling [57]. The combination of two atoms mixes the orientation of the constituent electrons which, through the Universe's natural preference for low-energy states, leads to

^aIn this text, the relic photon field and the CMB will be referred to interchangeably.

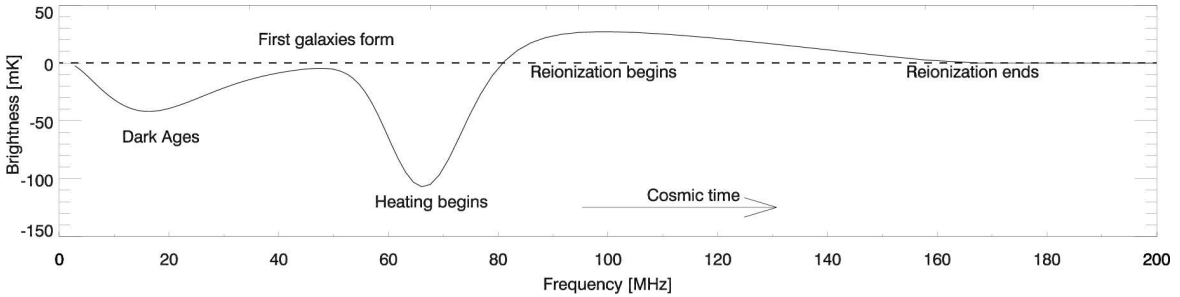


Fig. 1.1 A simulation of the expected 21-cm hydrogen signature based on typical models as a measurable brightness temperature (solid line) relative to the CMB temperature (dashed line). The turning points made from crests and troughs detail various stages of cosmic evolution such as the Dark Ages, the arrival of the first stars and galaxies, maturation of luminous sources and the Epoch of Reionisation. Image taken from Pritchard and Loeb [56].

a net de-excitation of electrons when the pairs dissociate. This sweeping reset of electron orientations down to their lowest energy configuration breaks the equilibrium state as more de-excited hydrogen atoms are free to absorb 21-cm photons from the CMB. This loss of 21-cm photons by the CMB should be seen as minute deviations from the spectrum predicted by the Planck equation allowing us to timestamp the construction of dense hydrogen pockets that would eventually coalesce into the first stars. This collisional coupling is only temporary though, as the expansion of the universe cools hydrogen adiabatically returning the primordial gas to equilibrium with the CMB as shown in fig. 1.1 [57]. This collection of processes in the absence of luminous sources is referred to as the Dark Ages.

The hydrogen gas in the most dense pockets eventually condenses into the first stars during Cosmic Dawn where ultraviolet (UV) radiation is generated for the first time since the Big Bang. Within this band of UV radiation are photons with a frequency of 2470 GHz known as a Lyman- α photon. These Lyman- α photons will bring the neutral hydrogen atoms to an energetic state beyond the spin flip which promptly decay down to the de-excited ground state, effectively cooling the gas and allowing for more absorption of CMB photons. This process, called the Wouthuysen-Field Effect, should yield an even stronger absorption trough than the collisional coupling as seen in fig. 1.1 [73, 26]. This first generation of stars will eventually mature into the first black holes and neutron stars producing even stronger radiation such as X-rays and gamma rays which will saturate the hydrogen gas and ionise them during an Epoch of Reionisation [35]. The inability of hydrogen gas to continue absorbing photons will heat the gas past the CMB temperature leading to an emission profile as seen in fig. 1.1.

It is evident that CMB absorption and emission by primordial hydrogen gas traces early astrophysical processes that remain unconstrained by observation. Theory suggests that this

may be measured as a differential brightness temperature relative to the predicted CMB profile and redshifted to radio frequencies between 50 and 200 MHz which can be represented by the equation

$$T_{21}(z) \approx 0.023K \times x_{\text{H}_I}(z) \left[\left(\frac{0.15}{\Omega_m} \right) \left(\frac{1+z}{10} \right) \right]^{\frac{1}{2}} \left(\frac{\Omega_b h}{0.02} \right) \left[1 - \frac{T_R(z)}{T_S(z)} \right], \quad (1.2)$$

and is dependent on many characteristics of the early universe such as the fraction of hydrogen gas that is neutral $x_{\text{H}_I}(z)$, the matter and baryon densities with respect to the critical density of the Universe Ω_m and Ω_b as well as Hubble's constant h [15]. Also present in the equation is the temperature of the background radiation T_R and the spin temperature T_S which represents the relative populations of excited and de-excited electrons^b. Qualities of early luminous sources such as the efficiency of star formation or the mean free path of ionising photons will affect heating and alter the profile of the differential brightness temperature, producing a unique 21-cm brightness temperature such as the models shown in fig. 1.2 where each individual line corresponds to a possible cosmic history [18]. Working backwards from an observed signal would provide constraints to these parameters narrating the influence of the first structures on the primordial hydrogen.

With the potential to provide such a wealth of information, many experiments have attempted to measure the 21-cm signature by taking long spectral integrations averaged over the entire sky, also known as a ‘global’ measurement. This method has been employed in projects such as the Broadband Instrument for Global Hydrogen Reionisation Signal (BIGHORNS) [66], the Large-Aperture Experiment to Detect the Dark Ages (LEDA) [55], the Shaped Antenna Measurement of the Background Radio Spectrum (SARAS) [51] and the Sonda Cosmológica de las Islas para la Detección de Hidrógeno Neutro (SCI-HI) [70]. Another method of observation is the utilisation of interferometric arrays to measure spatial fluctuations in the sky brightness temperatures on the scales of megaparsecs which would give details on individual luminous sources. This technique is used in experiments such as the Low-Frequency Array (LOFAR) [68], the Precision Array for Probing the Epoch of Reionization (PAPER) [50], the Hydrogen Epoch of Reionization Array (HERA) [21] as well as the future Square Kilometre Array (SKA) [22].

Despite the developments in radio astronomy, a definitive detection of the 21-cm signature is yet to be made due to the difficulties that arise from such a measurement. One hindrance to experimentation are astrophysical foregrounds that may be up to five orders of magnitude higher than the proposed hydrogen signal at radio frequencies. These foregrounds include radiation produced from cosmic ray electrons moving through magnetic fields in our galaxy

^bThe factor of 0.023 K comes from atomic-line physics [15]

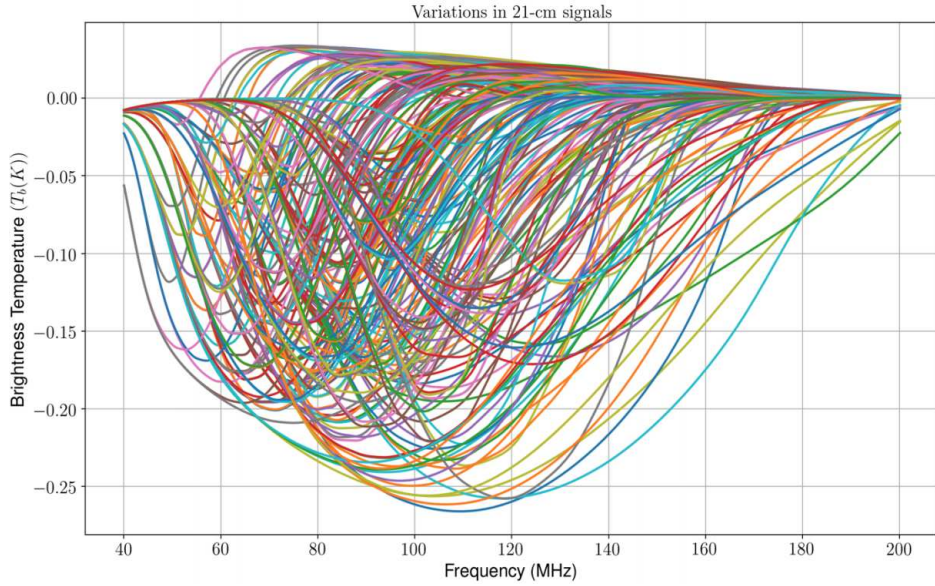


Fig. 1.2 Numerous simulations of plausible hydrogen signatures each representing a possible cosmic history. Various parameters such as the precise arrival of the first stars and galaxies will alter the hydrogen signal which when compared will allow theoreticians to identify models most representative of our early Universe. Data for image taken from Cohen et al. [18].

known as galactic synchrotron radiation, or the emission of photons when electrons scatter off the presently-ionised hydrogen nuclei known as free-free emission [61, 44]. Fortunately, it is thought that the various crests and troughs of the 21-cm signature, known as ‘turning points’, allow the hydrogen signal to be distinguishable from the foregrounds which are smooth at radio frequencies and approximated by simple power law equations [15]. Another point of concern are TV and FM radio broadcasts which are emitted at the frequencies relevant to 21-cm experiments [20]. Earth’s atmosphere is also known to be refractive at radio frequencies causing any potential signal to wander around the sky as ionospheric patches roll past the telescope’s observational beam [68]. In response to these challenges however, scientists have developed models and methods to mitigate the effects of such impediments enabling continued studies which have provided intriguing results.

1.2 The EDGES experiment

To date, the most significant result in 21-cm experimentation has been made by the Experiment to Detect the Global EoR Signature (EDGES) which aims to detect the sky-averaged 21-cm brightness temperature from the EoR [43]. The project has been conducting multiple

observations from the Murchison Radio-astronomy Observatory in Western Australia since 2006 [43] using multiple dipole-like antennas of metal panels mounted horizontally above a ground plane [15]. Early measurements placed an upper limit on the relative brightness temperature of the redshifted 21-cm signal contribution to their recorded foreground-removed spectrum [14] as well as a lower limit to the duration of the reionisation epoch with $\delta z > 0.06$, the latter result effectively excluding rapid reionisation models [12]. Following the deployment of one high-band and two low-band instruments, EDGES reported the detection of a flattened absorption profile in the radio spectrum centred at 78 MHz with a width of 19 MHz and depth of 0.5 K which they suggest is the 21-cm hydrogen signature [15].

The finding was met with considerable discussion as the detected profile's characteristics did not match theoretical models. The trough centering at 78 MHz (corresponding to a redshift $z \sim 18$) would require more efficient star and galaxy formation at high redshifts [41] while its flattened Gaussian shape suggest a delayed start to X-ray heating after the formation of Lyman-alpha emitting stars, not consistent with models [18]. Most notably however, was the profile amplitude which is more than a factor of two greater than the largest predictions by Cohen et al. [18] as shown in fig. 1.3 which would indicate that either primordial gas was cooler than expected or that the background radiation temperature was hotter than expected [15]. With both the radiation and gas temperatures constrained by the CMB and adiabatic cooling mechanisms, known astrophysical processes are unlikely to account for the observed discrepancy and new physics have been proposed to rectify the inconsistency such as an IGM cooling channel facilitated by dark matter-baryon interactions [15]. Other phenomena such as an excess radio background due to efficient black hole formation obscured by dense hydrogen halos have also been proposed [24].

Alternatively, inaccurate analysis methods or instrumental systematics may also account for the disparity between the EDGES data and theoretical models. Hills et al. [30] showed that the EDGES modelling process implied unphysical foreground emission parameters while Sims and Pober [62] describe systematic calibration errors preferred by the Bayesian evidence under statistical analyses of the publicly available EDGES data^c. The SARAS 3 radiometer measuring radio sky spectra at 55–85 MHz tested for the presence of the EDGES best-fit profile which was rejected from their data at the 95.3% confidence level [63]. Furthermore upper limits on the 21-cm power spectrum set by HERA Phase I observations were found to neither support nor disfavour a cosmological origin to the feature seen by EDGES [1].

The divided interpretation of the profile centred at 78 MHz highlights the need for follow-up experimentation to definitively confirm or refute the findings of Bowman et al.

^cavailable at <http://loco.lab.asu.edu/edges/edges-data-release/>

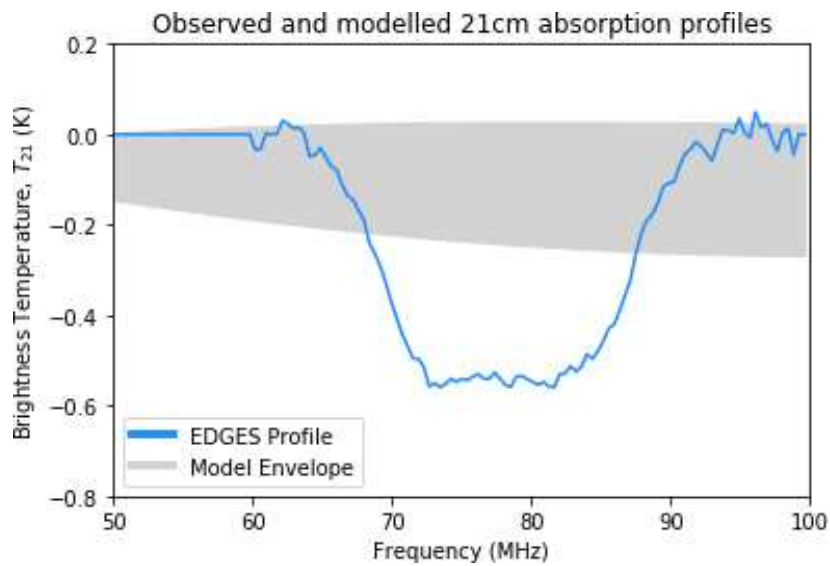


Fig. 1.3 The detected EDGES profile shown in blue [15] over an envelope of models from fig. 1.2 shown in grey. It is evident that the EDGES signal exhibits an absorption trough that is deeper than all of the models shown. If astrophysical, this suggests an increased amount of CMB photon absorption by neutral hydrogen gas than previously expected. Additionally the flatness and width of the absorption trough are also unlike the models shown in fig. 1.2. All of these differences which may require new physics to explain. Data for EDGES signal available in footnote link ^c. Data for model envelope from image by Cohen et al. [18].

[15]. Continued investigations will need to improve on the instrumentation, analysis methods and measurement techniques in order to avoid data of nebulous origin or questionable interpretation. Many projects such as Probing Radio Intensity at high-Z from Marion (PRIZM) [53], Mapper of the IGM Spin Temperature (MIST) [42] and the Dark Ages Polarimeter PathfindER (DAPPER) [16] are spearheading the effort including a certain Cambridge-led collaboration...

1.3 The REACH experiment

The Radio Experiment for the Analysis of Cosmic Hydrogen (REACH) is a Cambridge-led sky-averaged 21-cm experiment of which the author is a member of. The radiometer targeting the cosmic hydrogen signature between 50–170 MHz ($z \sim 7.5\text{--}28$) has a principle science objective of verifying the EDGES detection through a phased deployment at the RFI-quiet Karoo South African radio reserve [20]. A design focus on the identification and removal of residual systematics sets REACH apart from concurrent experiments which typically aim to minimise the chromatic response of the instrument as achromatic antennas mitigate the introduction of spectral components into foreground signals [14, 64]. Relying on such a ‘smooth’ instrument response presents challenges such as with EDGES where the resulting frequency bandwidth ratio is restricted to 2:1 necessitating the use of scaled systems with overlapping bands to cover the full frequency range. REACH alternatively intends to improve on current experiments through the joint detection and characterisation of instrument systematics together with astrophysical foregrounds and the cosmic signature using Bayesian statistical methods [3, 4]. This joint fit between physically-based models is expected to facilitate the detection of correlated systematics and avoid those potentially degenerate with a cosmological signal with unaccounted-for systematics diagnosed using Maximally Smooth Functions [7].

REACH Phase I plans on taking simultaneous observations of the sky using two antennas; the hexagonal dipole (50–130 MHz) and the conical log spiral (50–170 MHz) both of which were chosen from numerous designs for their ability to reconstruct mock 21-cm signals to a high degree of statistical confidence with small root mean square error in simulations [2]^d. The antenna pair will be analysed in parallel to isolate signal components associated with hardware systematics while the contrasting mechanical designs will prevent experimental sensitivity to hardware-specific systematics. The project’s non-reliance on achromatic antennas allows for an ultra-wideband system covering the Cosmic Dawn and EoR (up to 3.5:1 for the conical log spiral) [19]. Using such a large bandwidth, spectral differences

^dWe note that the hexagonal dipole is similar to the rectangular dipole antenna used in the EDGES experiment

between the oscillating 21-cm signature and the smooth power-law foregrounds can be leveraged during data analysis to support a positive detection [20].

The deployment site was also chosen with care after an extensive survey. In the Karoo, REACH will observe the southern hemisphere sky from a remote 4 km wide basin surrounded by hills and mesas offering a reduced FM radio presence. Located near similar experiments such as HERA, MeerKAT [31] and the Square Kilometre Array (SKA)1-Mid instrument [22], the location offers critical support infrastructure including on-site maintenance, staff as well as controlled access through paved roads. A Phase II experiment is planned for the same site which will incorporate additional antenna systems. Scaled versions of the hexagonal dipole and dual polarisation antennas have been proposed.

Simulations run with the above specifications forecast percent-level constraints on astrophysical parameters using REACH and in the case of a non-detection, upper limits on the strength of the absorption feature can be used to bound high-redshift phenomena [20]. We estimate a ~ 500 mK absorption profile consistent with EDGES can be detectable in as little as three hours of integrated data out of approximately 30 hours of observation time ($\lesssim \frac{1}{6}$ th the time necessary to detect more conservative 21-cm signature models at the same redshift), though up to an order of magnitude more time may need to be allocated for the removal of low quality data and calibration measurements. If the data do not support an EDGES-like or high-amplitude 21-cm signal, the experiment will continue to integrate for longer periods in which case REACH will be able to place rigorous constraints on any excess radio background amplitudes and hydrogen cooling mechanisms beyond the typical adiabatic expansion. For the case of a detected 21-cm absorption signature much smaller than the EDGES profile in the high signal-to-noise regime, forward modelling consistent with standard astrophysics and cosmology will be used to constrain parameters such as the low-energy cutoff frequency and power law index of the X-ray spectral energy distribution, the X-ray efficiency of sources, the CMB Thomson-scattering optical depth, the minimum virial circular velocity of star-forming galaxies, the mean free path of ionising photons in the IGM as well as the star-formation efficiency [28, 69, 25].

Contingent on this detection is of course, the measurement accuracy and sensitivity of the instrument as a whole. The contribution to this project by the author is the maximisation of such attributes through the construction of a high quality radio-frequency receiver unit, its seamless incorporation within the overarching system, as well as the development of intelligent software for receiver calibration. In this thesis, we present the designs, motivation, specifications and production of the REACH front-end and back-end receiver unit for deployment in 2023 highlighting its unique architecture and features to aid in instrument characterisation. We also detail an innovative calibration procedure that incorporates a

Bayesian methodology leading to an in-field, rapid algorithm for calibration of the instrument in the same environment as observations, a first of its kind. While presenting the results of the technique, we highlight the challenges of achieving the accuracy needed to detect such minuscule 21-cm signals as well as present a framework for continued advancements in calibration towards the detection of the highly-redshifted global 21-cm hydrogen signature.

Chapter 2

Receiver design and development

Measurements of the radio-sky require an instrument called a ‘radiometer’, a machine that measures incoming radiation. A radiometer usually consists of two main components; an antenna to collect an electromagnetic waves and a device to measure the signal’s power such as a spectrometer. As more advanced instruments are deployed, additional processes are implemented to condition this information before being sent to the spectrometer such as amplification of weak signals and filtering to an frequencies of interest such that a new intermediary device is often introduced as a bridge between the antenna and the spectrometer known as a ‘receiver’.

The addition of components such as a receiver will necessarily produce more complicated forms of systematic noise, through things like reflections spawned from impedance mismatches at connections which hamper the detection and analysis of astrophysical phenomena. Characterising the interaction of the various instrument components as well as the resulting noise is undertaken through auxiliary devices which inform the process of ‘calibration’ in order to ultimately remove systematics and facilitate detection of cosmic signals. Consideration for the ensemble of devices, their control and monitoring is a principle area of experimental instrument design and the development of new architecture and engineering techniques to accommodate the unique requirements of individual experiments is the focus of this next chapter.

2.1 The REACH receiver

The REACH receiver is designed to address concerns brought forth with other experiments regarding residual systematics in their data while permitting the innovative features of the overall radiometer. Primarily, the broad bandwidth used by REACH makes it impractical to develop an achromatic antenna that provides a perfect impedance match between the antenna

and receiver. Reflections spawned from this contact point result in considerable spectral variation across the observational band on the order of tens of Kelvin due to the overwhelming synchrotron foreground at these frequencies. Furthermore, while the method of ‘relative calibration’ was historically used to characterise narrow-band instruments, wide-band radiometers must obtain an absolute flux scale in frequency to measure the frequency-dependent sky-averaged brightness temperature through ‘absolute calibration’, which necessitates a series of additional components and switches.

Another primary focus of the design approach was the ability to calibrate the instrument completely in the field^a as opposed to previous experiments where the devices were characterised in controlled laboratory settings before deployment. The environmental (e.g. temperature and humidity) dependence of the sensitive electronic components provided a challenge to be addressed in the receiver design which requires system and temperature stability in the field as well as full autonomy.

In response to these considerations, the REACH receiver system is comprised of two subsystems, the receiver ‘front-end’ that sits under the raised antenna ground plane and the receiver ‘back-end’, also known as the readout system, which is separated from the front-end by a 100 metre distance connected by a Radio Frequency over Fibre (RFoF) link and powered by solar panels. A conceptual diagram of the radiometer system is shown in fig. 2.1. Many of the environment-sensitive components responsible for calibration and conditioning of the data are included in the front-end, with the back-end containing components for spectral data collection, control and signal processing as detailed below.

2.1.1 Receiver front-end

The front-end contains the most sensitive radiometer components housed in a sealed enclosure to facilitate calibration of the instrument to the highest accuracy. As the maintenance of environmental stability is difficult to achieve over long periods of time in the field, the project’s emphasis on an *in situ* calibration could only be achieved through a conscious effort to minimise the volume of the receiver front-end such that a constant temperature is kept via thermal devices while drawing a sustainable amount of power from the solar panels which are rated to give a maximum of 135 W of power to the front-end. Given this as a primary focus during the design process, nearly all of the components in the front-end were chosen based on a careful balance between their compact size and superior quality.

^aWhile this philosophy was not completely adhered to in the final deployed system, the spirit of this ambition guided the entire receiver development. Please see CHAPTER ON S-PARAMETER CORRECTIONS for more details.

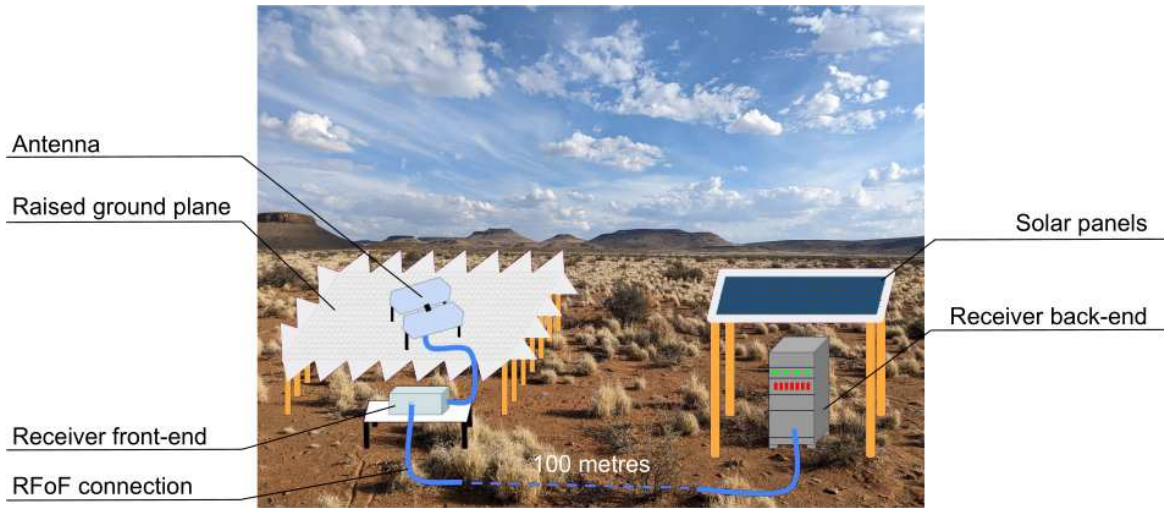


Fig. 2.1 An illustration of the REACH radiometric system showing the hexagonal dipole antenna on a raised ground plane above the receiver front-end linked to the back-end and solar panels by 100 metres of fibre optic cable. The background image is a picture taken of the REACH deployment site located in the South African Karoo Radio Astronomy Reserve.

The front-end enclosure

The entirety of the receiver front-end is contained in a $500 \times 500 \times 210$ mm Rittal AE 1007.600 stainless steel enclosure serving as an RF-shield with category IP 66 protection against dust and water from the outside environment. 20 mm^b of Kingspan Kooltherm K5 External Wall Insulation Board lines the inner walls of the enclosure in order to assist with temperature stability. Original designs used 11 mm Zotefoam for its efficient absorption of infrared radiation as used by the BICEP and Keck Array, but thermal tests showed this material to be less efficient during cooling compared to the $0.021 \text{ W m}^{-1}\text{K}^{-1}$ thermal conductivity of the building-standard Kooltherm sheets. Six connection ports were drilled into the enclosure to interface with external components; one for connection to the antenna sitting directly above the receiver on the raised ground plane via 150 mm Heliax cable, two for control and monitoring via USB over fibre-optical link, one RFoF connection for communication with the receiver back-end, one SubMiniature version-A (SMA) port for the 48 V DC power supply from the solar panels and an additional coaxial SMA port for testing and triage in the field. EMI gaskets were placed around the openings to reduce the impact of self-generated RFI towards the antenna as well as external RFI from feeding into the signal chain. A diagram of the enclosure's external connections is shown in fig. 2.2.

The metal framing of the enclosure also served as a heat dump for the encased electrical components using a custom heat exchanger and fan-assisted heat sink as detailed in the next

^b18 mm in actuality when measured

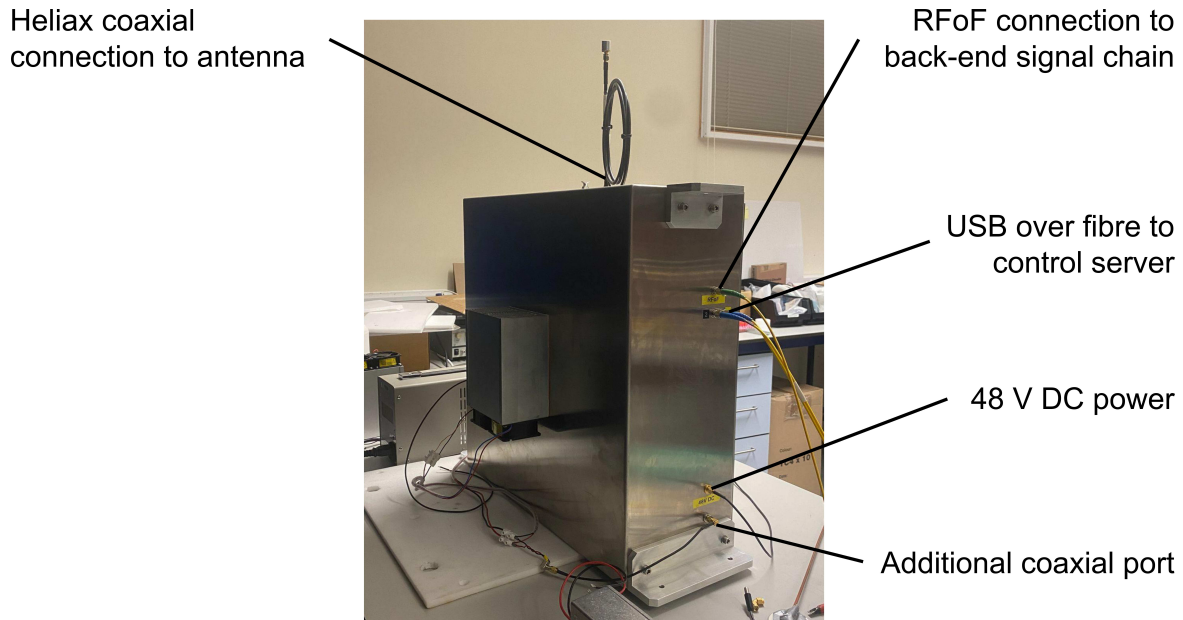


Fig. 2.2 The external connections of the receiver front-end enclosure showing the coaxial antenna connections, USB to fibre connections in blue, RFoF connection in green, power connection and additional port for in-field diagnostics and testing. The orientation shown is the same as during deployment.

section. To assist with the thermal considerations, the receiver front-end components are mounted on a 3 mm baseplate as shown in fig. 2.3 to allow airflow between the plate and the internal heat exchanger.

Front-end thermal management system

Front-end temperature stability is maintained through a stack of components placed below the centre of the baseplate. A 113 watt Laird UltraTEC UT6-24-F1-5555 proportional integral derivative thermoelectric cooler (TEC) drives cooling or heating through the Peltier effect which is coupled to the receiver component baseplate by a $55 \times 55 \times 16$ mm copper stack. A thermal gap pad connects the bottom of the TEC module with a larger copper plate on the enclosure wall allowing heat transfer to an external Fischer LA7 150-1 heatsink and fan for expulsion of heat to the outside environment.

An initial test of this setup was conducted by placing a 40 W 110×110 mm heating source below the receiver component baseplate centre which recorded a 5 K (or 8 K?) temperature gradient over the plate as shown in fig. 2.4. Following the results of this test, a secondary baseplate was installed below the initial baseplate with the two plates separated by a heatsink and an internal fan installed to promote air circulation throughout the front end. A

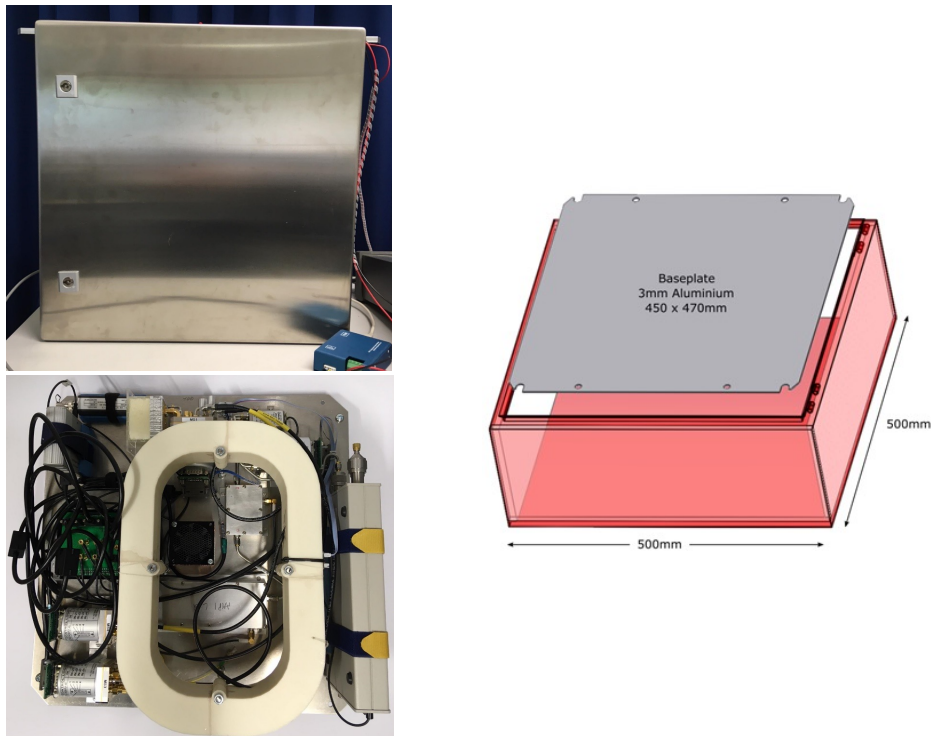


Fig. 2.3 A picture of the front-end enclosure is shown on the top left. The bottom left shows the front-end components bolted onto the 3 mm baseplate. The diagram on the right depicts the baseplate's insertion into the enclosure.

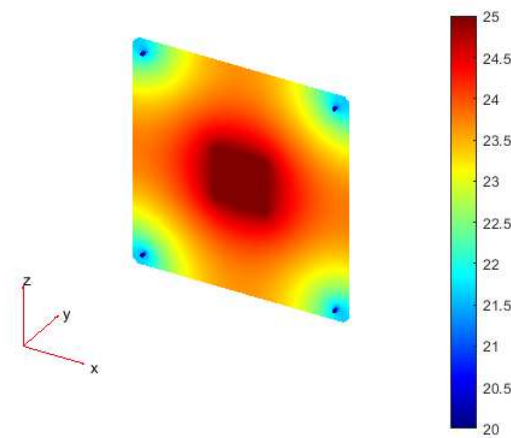


Fig. 2.4 A plot from an initial temperature test showing a 5 K temperature gradient over the receiver component baseplate when heated from below by a 40 W heat source placed at the plate's centre.

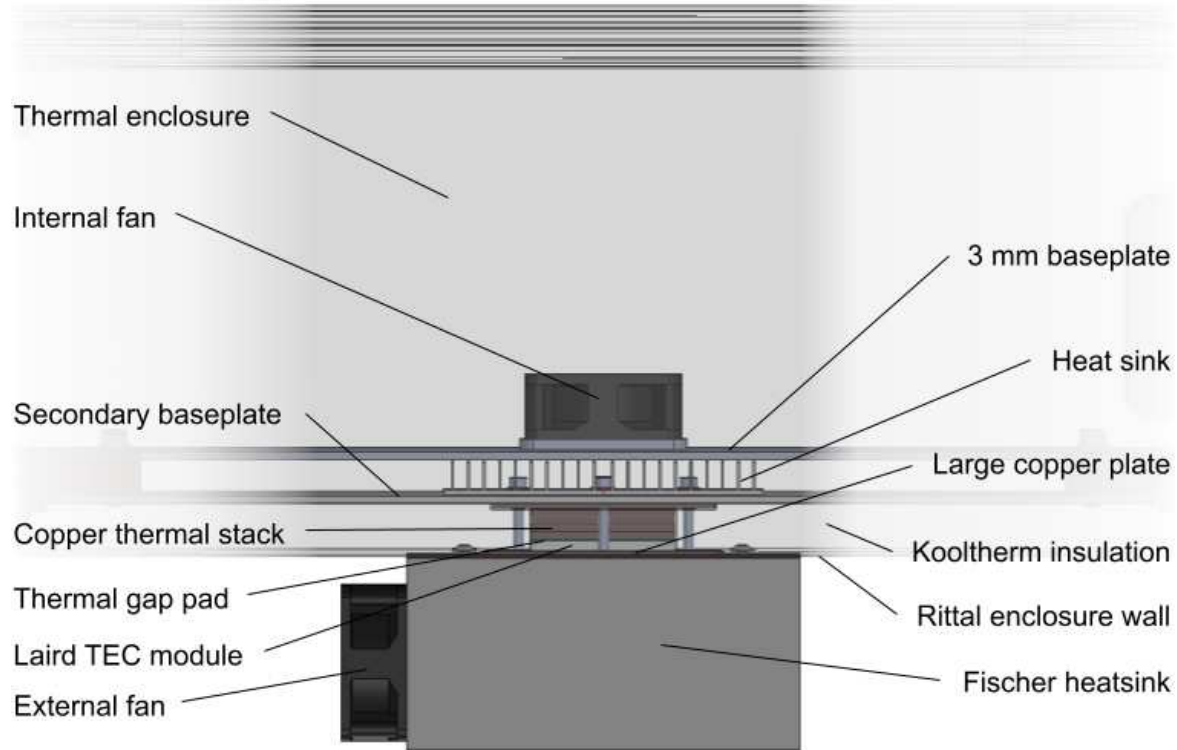


Fig. 2.5 A diagram representing the components for thermal conditioning of the receiver front-end. The vantage point shown is as if the front-end enclosure is laid on its back. It should be noted that the above figure is the MK II version which is slightly updated from the configuration currently deployed in the field.

follow-up test using this configuration returned a temperature gradient of 0.125 K across the component baseplate. A diagram of the completed setup is shown in fig. 2.5

The TEC is controlled by an Electron Dynamics Southampton TC-M-U-10A module and powered by a separate custom-made 22 V power supply unit (PSU) designed to reduce RFI coupling from the very large switch currents produced. The PSU, shown in fig. 2.6, is also configured to automatically power the external fan when the Electron Dynamics controller draws more than 6 W of power to prevent thermal overload.

The effectiveness of the front-end thermal management system was evaluated by testing the performance of the construction on 6 litres of bottled water placed in the empty front-end enclosure at room temperature with the TEC driven at its maximum 88 W and the Electron Dynamics controller instructed to maintain a 10° C setpoint temperature as shown in fig. 2.7 where the endpoint is achieved after about 8 hours of cooling with a steady-state temperature within 0.01 K of the target setpoint. These results suggest that a long, continuous amount of cooling is needed to stabilise the front-end temperature before calibration or observational measurements are made. This may be done in the afternoon or evenings preceding

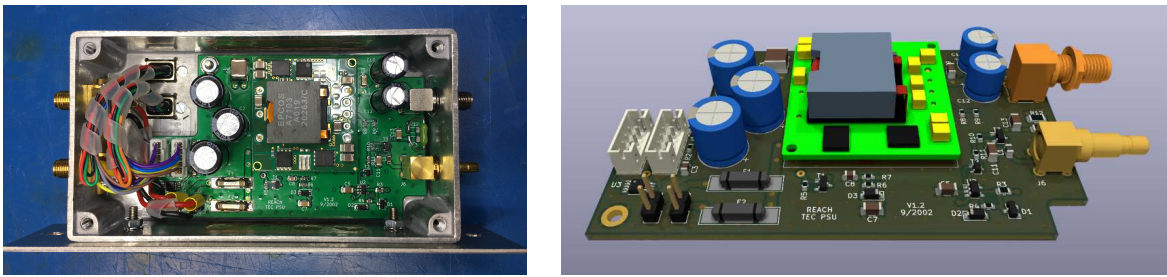


Fig. 2.6 The constructed thermoelectric cooler power supply unit (left) along with its original CAD rendering (right) for perspective.

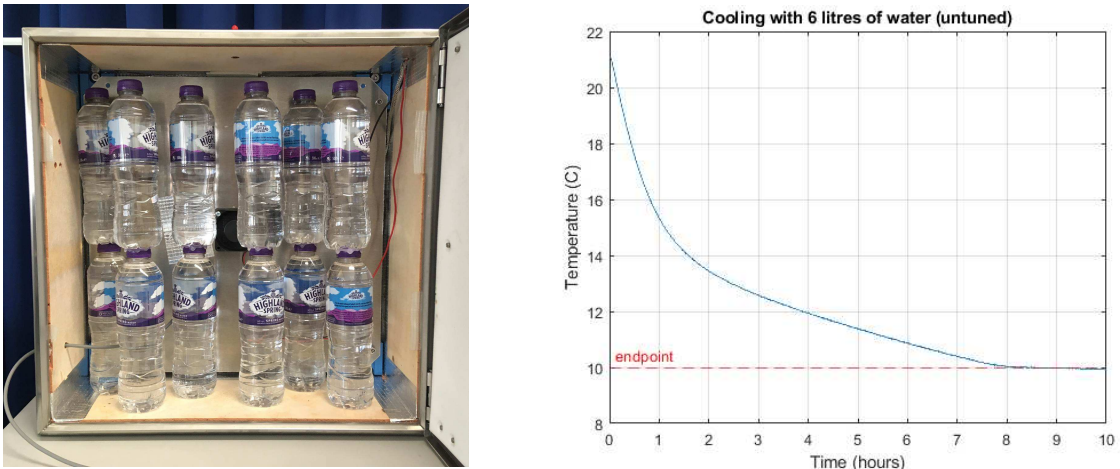


Fig. 2.7 Six litres of water placed in the empty front-end enclosure with the thermal management system installed. The results of this test with the TEC driven at its maximum wattage and the controller setpoint of 10°C is shown on the right. It should be noted that for this test, the proportional, integral and derivative controller values were not tuned beforehand, which reduces efficiency.

an observational run. OR FIND PLOT WITH TIME TAKES TO BRING FINALISED CONSTRUCTION TO SET POINT. An additional comparison of the completed thermal management system installed on the front-end enclosure with its 3D-rendered cross section is shown in fig. A.1 for reference.

Calibration sources

One of the main obligations for thermal stability was to stabilise measurements of passive devices used to calibrate the instrument which we collectively refer to as ‘calibration sources’ or ‘calibrators’. Historically, absolute calibration is undertaken through measurement of each calibration source as part of a three-position Dicke cycle containing a single source, a reference 50Ω load and a reference noise source where comparison of power spectral

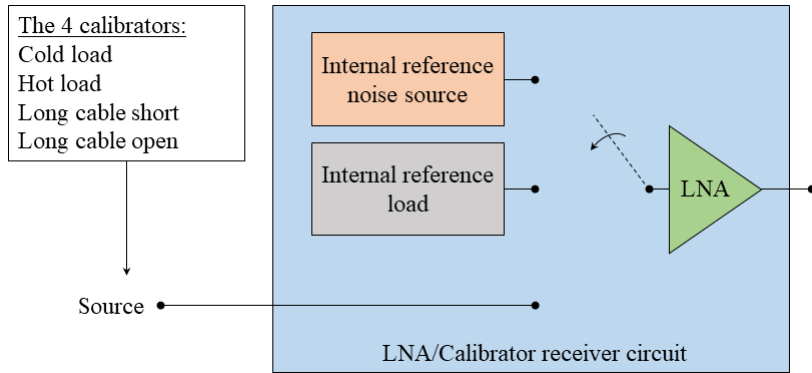


Fig. 2.8 A diagram of the Dicke switching procedure showing the calibrator position, 50Ω reference position and reference noise source position. Here, the four canonical calibration sources are used; the ambient and heated 50Ω loads along with the shorted and open cables. Power spectral measurements of these devices are conditioned by the Low Noise Amplifier (LNA) before being passed on to the spectrometer for initial removal of the time-dependant system gain.

measurements between the source and references serve to calibrate out time dependent system gain as detailed in REFERENCE Q-TERM EQUATION. Usually four sources were used; an ambient-temperature ‘*cold*’ 50Ω load, a 50Ω load heated to high temperature, a cable shorted at one end and a cable left open at one end. The 50Ω loads give the absolute temperature scale in our calibration solution while the cables simulate antennas looking at an isotropic sky with temperatures equal to the cables’ physical temperature. A diagram of the Dicke switching procedure used in calibration is shown in fig. 2.8.

The cold load used was taken from an 85033 50Ω SMA calibration kit certified by Kirkby Microwave. Multiple heated loads were custom made for this experiment. A simple heated load was constructed from a 4-inch RG-405 coaxial cable terminated with a 50Ω load attached to a proportional heater connected to DC power with the temperature directly monitored through contact with a thermocouple. As the heated calibration source is typically heated to ~ 370 K, which could affect the temperatures of nearby ambient components, an improved calibrator was constructed with the 50Ω resistor and thermistor attached to a 4-inch semi rigid cable surrounded with thermal insulation and encased in an acrylic cubic shell. A temperature gradient across the 4-inch cable within the construction is produced by the temperature difference between the heated load and the coaxial end connected to the receiver input. As this changes the temperature ‘seen’ by the instrument, a corrective factor is introduced in our calibration calculations and detailed in REFERENCE TEMPERATURE CORRECTION SECTION. While this advanced heated load was used for some of the results presented in this work such as in FORWARD REFERENCE SECTIONS, the simple

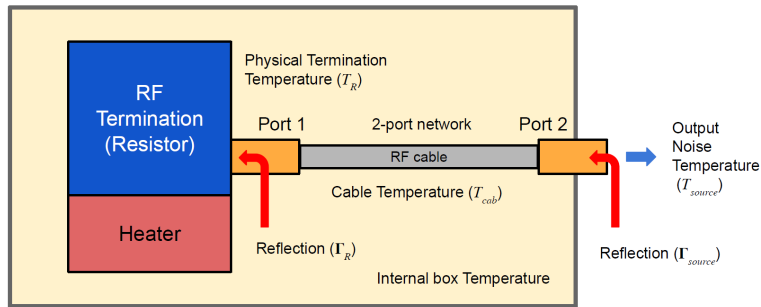


Fig. 2.9 Illustration of the heated load construction for use as a calibration source. The thermally enclosed resistor and powered heater are connected to the input switch via a 4-inch cable as shown in the diagram. These components effectively form a temperature gradient across the calibration device which must be corrected for via the procedure discussed in REFERENCE TEMPERATURE CORRECTION SECTION as T_R , T_{cab} and T_{source} are not necessarily equal.

heated load was the device deployed to the field due to time constraints impacting critical adjustments to reinforce the advanced heated load. A diagram of the advanced heated load is included in fig. 2.9.

Open and shorted coaxial terminations were taken from the same Kirkby 85033 kit and connected to the end of coaxial cables. Over the course of receiver development, many different models and lengths of cables with varied specifications were tried with the final deployed system having the open and shorted ends connected to 10 metre LMC195 coaxial cabling partially built in-house at Cambridge. With the need for more accurate characterisation of the instrument, we have expanded our selection of calibration sources to twelve, maximising the information detailing the instrument response. Additional ambient-temperature 25Ω and 100Ω resistors were included for increased data on non-complex impedance response. The same 10 metre LMC195 cable was also terminated with 10Ω and 250Ω resistors. An additional 2 metres of LMC195 terminated with 27Ω , 36Ω , 69Ω and 91Ω resistors was also included. These additional terminations were all custom made in Cambridge.

The calibration sources and resistances were carefully chosen to permit strategic sampling of the noise waves as a function of impedance. Figure 2.10 demonstrates the extensive scope of frequency-dependent impedances for our calibration sources as well as a simulated impedance of the REACH dipole antenna covering 50–150 MHz. Figure 2.10 also demonstrates measurements of the 25Ω and 100Ω loads as half circles on the Smith chart, which differs from the theoretical points at 25Ω and 100Ω due to the practical limitations of real-world impedance measurement and exacerbated by the additional RF path in our receiver between the sources and the measurement reference plane for the reflection coeffi-

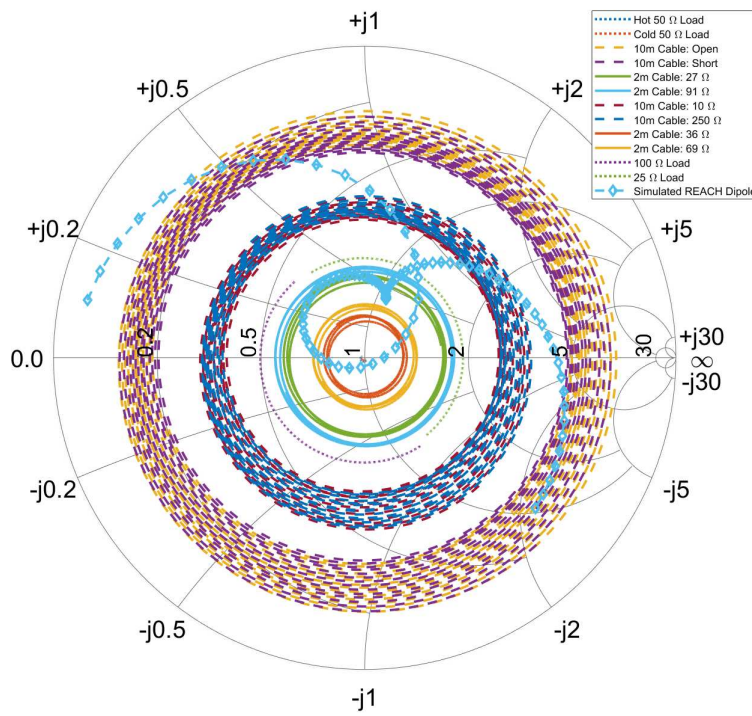


Fig. 2.10 Smith Chart showing the impedance of twelve calibration sources and the simulated REACH antenna (internal variant #0744) with the centre of the plot indicating an impedance of 50Ω . The plot ranges from 50–150 MHz with the antenna curve starting at 50 MHz on the left-hand side. The extensive coverage in impedance space by our calibration standards can be interpreted as a substantial amount of information regarding the characteristic response of the instrument. Note that the impedances of the ambient and heated 50Ω loads lie directly in the middle of the chart and are partially obscured by the antenna plot. Updated from figure included in REFERENCE REACH NATURE PAPER

Frequency	Excess noise ratio	Frequency (contd.)	Excess noise ratio (contd.)
30 MHz	6.05 dB	110 MHz	5.80 dB
40 MHz	6.03 dB	120 MHz	5.77 dB
50 MHz	6.00 dB	130 MHz	5.80 dB
60 MHz	5.94 dB	140 MHz	5.81 dB
70 MHz	5.91 dB	150 MHz	5.83 dB
80 MHz	5.87 dB	200 MHz	5.88 dB
90 MHz	5.84 dB	250 MHz	5.87 dB
100 MHz	5.79 dB	350 MHz	5.87 dB
110 MHz	5.80 dB	500 MHz	5.89 dB

Table 2.1 Manufacturer quoted noise output for the Noisecom NC346A noise diode used as the reference noise source within the Dicke switching procedure as an excess noise ratio. The stability of the noise output within the REACH observational band (50 – 130 MHz) at these scales should be noted, which is beneficial for the removal of time-dependent system gain.

cients. These effects were the motivation for the corrections detailed in REFERENCE S11 CORRECTION MATHS SECTION.

Power spectral measurements are taken of two reference sources for every measurement of a calibration source to divide out the short-time variability in receiver gain as previously stated. Ideally, the reference load would be a separate 50Ω load of high quality such as from an additional certified calibration kit, but due to time constraints in the deployment, a repeated measurement of the ambient load used as a calibration source was taken. As these Dicke switch measurements detail the changing gain of the system and not the absolute differences between the devices used as calibration sources and reference sources, we believe that this degeneracy would not severely impact the quality of the results presented in this work.

The reference noise source used is a Noisecom NC346A. An important distinction must be made here between the heated 50Ω load as a calibration noise source and the Noisecom noise diode used as a reference noise source. While the constant noise power provided by the noise diode is necessary for maximal radiometer measurement accuracy through removal of the time-dependent gain fluctuations via the Dicke switching procedure, the direct and accurate measurement of the heated 50Ω load via thermocouple is beneficial for the removal of systematic noise via accurate noise wave parameter derivation.

Noise output data of the reference noise diode as provided in decibel excess noise ratio by Noisecom is shown in table 2.1. We can convert the noise output values from table 2.1 to

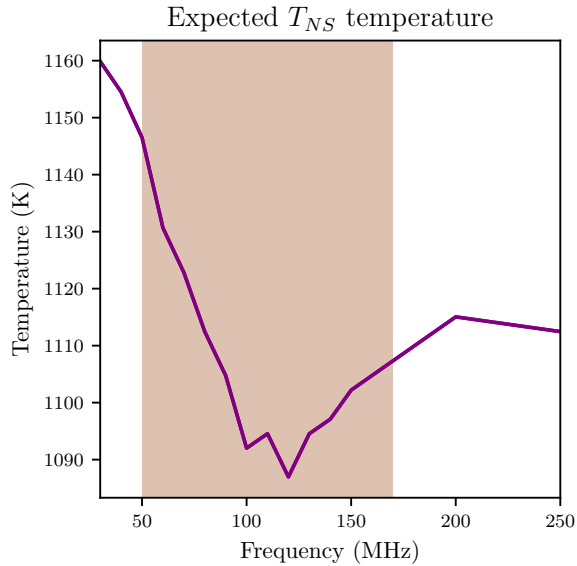


Fig. 2.11 A plot of the reference noise diode output from the datasheet provided by Noisecom. The scale of the plot gives us a value expected of the T_{NS} noise wave parameter from our calibration algorithm. As shown, the output of the diode is essentially stable at these high temperature scales but cannot be measured accurately in the field due to the output being an effective noise temperature from a diode imitating the noise of a black body at such a temperature. The shaded region is the REACH observational band 50–130 MHz.

linear scale using the equation

$$\text{ENR}_{\text{dB}} = 10 \cdot \log_{10} \left(\frac{T - 290}{290} \right) \quad (2.1)$$

with 290 being the standard reference temperature for noise and T as a linear-scale excess noise above ambient temperature (assumed to be 298 K). A plot of the linear noise output of the reference noise diode with ambient temperature subtracted is provided in fig. 2.11 which may serve as a potential sanity check for our calibration algorithm as these values inform us of the approximate values of the T_{NS} noise wave parameter as detailed in REFERENCE RECEIVER MATHS SECTION and verified in fig. 4.20. This value may not be exactly replicated however, due to the additional RF path introduced earlier and again detailed in REFERENCE S11 CORRECTION MATHS SECTION. It should also be noted that these values are exclusive to this particular noise source and the use of different noise diodes in future builds, including identical model numbers, would necessarily be different and require recalculation following the above prescription.



Fig. 2.12 3D printed housing for the 2 metre and 10 metre calibration cables. This unit is affectionately referred to as ‘the stadium’.

Switches

The sizeable battery of calibration and reference sources may seem at first glance to run against the primary goal of having a small-volume receiver. To meet this challenge, a complicated network of mechanical switches was conceived to allow for the myriad components and various signal paths through the instrument. The essential calibration sources mentioned in the previous subsection were gathered on an 8-way switch (referred to as MS1) with switch positions one through six taken up by the antenna, cold load, reference noise source, heated load, 25Ω load and 100Ω load respectively. To avoid the size requirements of having multiple calibration cables with various terminations, a single 2 metre LMC195 cable and 10 metre LMC195 cable were connected to MS1 positions seven and eight with the opposing ends of the cables connected to their own 4-way switch referred to as MS3 and MS4 respectively. These cable switches were connected to the appropriate terminations according to the previous subsection; 36Ω , 27Ω , 69Ω and 91Ω for MS3 positions one through four as well as open termination, shorted termination, 10Ω and 250Ω for MS4 positions one through four for the 2 metre and 10 metre cables. A custom 3D-printed structure was designed to house the two calibration cables within the receiver front-end which is highlighted in fig. 2.12

A schematic block diagram of the switching configuration is shown in fig. 2.13. As shown, a Mechanical Transfer Switch (MTS) facilitates pathways to the Low Noise Amplifier (LNA) and Vector Network Analyser (VNA) for spectral and reflection measurements respectively. MTS position two connects directly to the 8-way switch housing the calibration sources and MTS position four leads to the LNA/spectrometer pathway. The first and third MTS switch

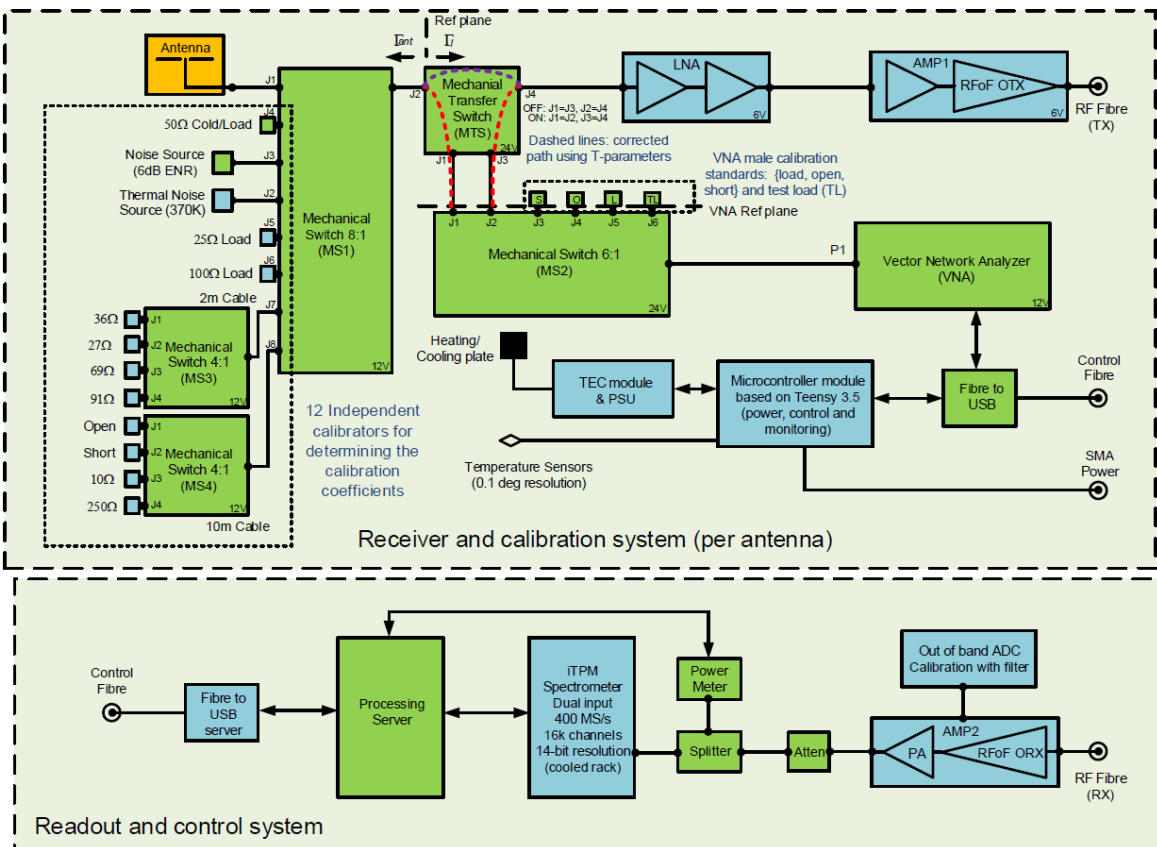


Fig. 2.13 An overview of the REACH radiometer showing calibration sources and the antenna connected to an 8-way mechanical input switch at the receiver input. The green sub-blocks represent off-the-shelf components, whilst blue represent custom designs. Γ_{ant} represents the reflection coefficient of the antenna or calibrator, Γ_l is the reflection coefficient of the low noise amplifier (LNA). The red dashed line represents the extra path measured by the VNA that is not present during spectral measurements while the purple dashed line is the path present exclusively during spectral measurements. Corrections for these additional paths are detailed in REFERENCE SPARAMETER CORRECTION SECTION. ‘ENR’ is the Excess Noise Ratio of a Noisecom NC346A noise source; ‘OTX’ indicates an optical transmitter; ‘TX’ indicates transmission mode; ‘TEC’ stands for Thermoelectric Cooling; ‘SMA’ is a SubMiniature version-A connector; ‘PA’ is Power Amplifier; ‘RX’ indicates reception mode and ‘Atten.’ represents a signal attenuator. Updated from figure included in REFERENCE REACH NATURE PAPER OR NIMA PAPER.

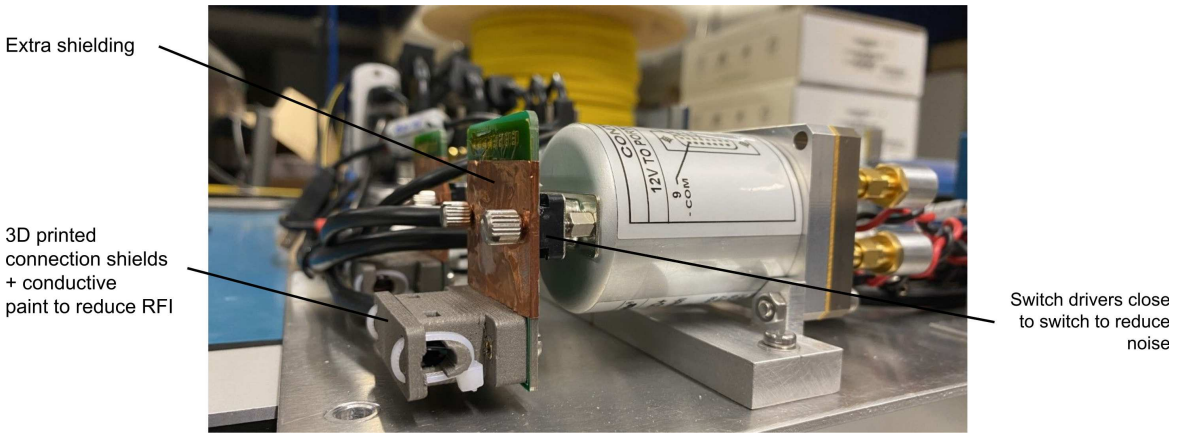


Fig. 2.14 A mechanical switch installed on the front-end component plate showing the extra shielding, 3D-printed housing and close placement of switch drivers.

positions connect to the first two positions of a 6-way switch (MS2) that direct to the VNA. MS2 positions three through six connect to additional calibration standards used to separately calibrate the VNA before measurement as detailed in a following VNA subsection. For all of the connections detailed here, male sources and terminations were connected to female switch connections to avoid reflections that would spawn from the inclusion of male-female adaptors^c

An effort was made to reduce any negative effects presented to the instrument by this network of switches. Mechanical switches were implemented over the alternative electronic switches due to the lower signal loss of the former. The Mini-Circuits absorptive switches chosen exhibit 0.01 dB loss within the REACH observational band with better than 100 dB isolation to reduce the radio-frequency leakage into the rest of the signal chain. Extra shielding was added to the switch drivers to further reduce self-induced RFI as shown in fig. 2.14. The 20 mm trace length of the mechanical switch drivers was mitigated by placing the drivers as close to the switch as possible followed with the inclusion of custom 3D-printed connection covers coated with conductive paint. A table of the mechanical switches used is presented in table A.1 for reference and a table with the contents of each switch connection detailed in table A.2. An mock-up of the switch configuration for a reflection coefficient measurement of the open-ended 10 metre cable is provided in fig. 2.15 for illustrative purposes as well.

^cor ‘worms’ as they are colloquially referred to.

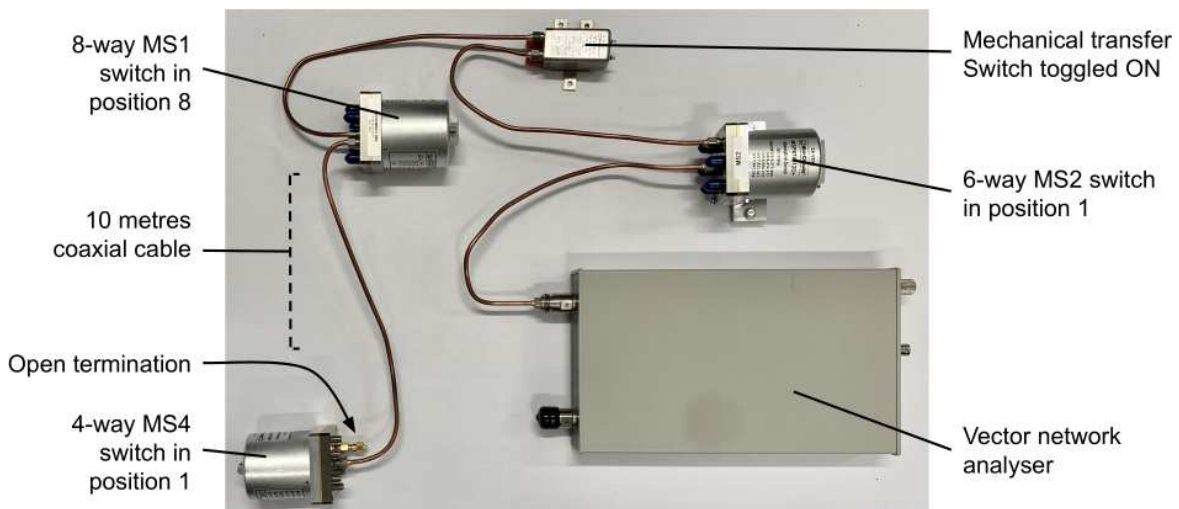


Fig. 2.15 A mock-up of the components and configuration needed for a reflection coefficient measurement of the open-ended 10 metre cable using parts from the receiver (except for the 10 metre cabling which was too long.). For this measurement, the open termination connected to the MS4 switch input port 1 with the MS4 switch toggled to position 1 via command line interface. The MS4 switch output is connected to the 10 metres of LMC195 cabling with the other end of the LMC195 cable connected to the port 8 input of the MS1 switch. The MS1 switch is toggled to position 8 via CLI. The MS1 output connects to the port 2 input of the MTS switch followed by a connection to the port 1 input of the MS2 switch. With the MS2 switch toggled to port 1, the MS2 output should connect to the VNA input allowing for a connection to the opened termination though the MS2, MTS, MS1 and MS4 switches. This configuration allows for a reflection coefficient measurement of the opened termination by the VNA.

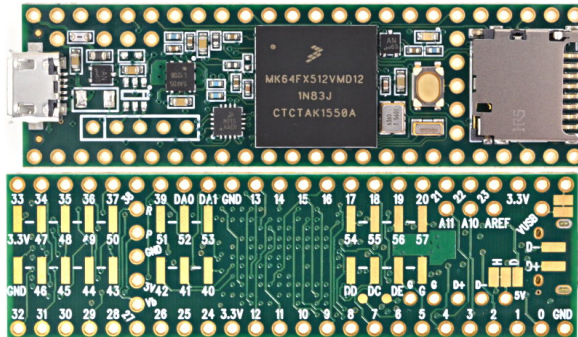


Fig. 2.16 The front and back of the Teensy board is shown in the top and bottom respectively. Along the edges of the board are the input/output connectors (yellow-outlined white circles) which are paired to specific mechanical switch configurations throughout the front-end.

The microcontroller unit

As with most modern instruments, control and monitoring of the receiver front-end and its individual components is overseen by a central device. This control unit is required to initialise the specific switch positions needed for measurements as seen in fig. 2.13. As an unmanned experiment in the South African Karoo, the capability for resetting components, especially during remote triage, is another critical function of the controller unit. With 88 necessary connections to oversee within the receiver front-end, construction of an adequate controller using off-the-shelf components would ordinarily take the space of a standardised 19-inch rack ($\sim 48 \text{ cm}^2$). This along with the low noise requirements and restricted power budget of the REACH experiment prompted the development of a novel control unit design; a miniaturised management device or, ‘microcontroller unit’^d. Much of the compactness of our miniaturised control unit can be attributed to a careful consideration in constituent components however, an innovative stacked dual-board design allowed us to reduce the size by an order of magnitude condensing the microcontroller unit into a $13 \times 12 \times 10 \text{ cm}$ volume.

The first of the two boards in our microcontroller unit is the control board mounted by a PJRC Teensy 3.5 development board^e based on the Arduino infrastructure. The Teensy board, as shown in fig. 2.16 contains 64 digital input/output ports assigned to individual switch configurations facilitating component control through a USB serial interface. The $110 \times 90 \text{ mm}$ control board upon which the Teensy board is mounted to also contains the 48 V power input from the solar panels as well as 12 V and 5 V outputs for front-end components and can be seen in fig. 2.17. The controller board also incorporates RFI filtering and I²C bus

^dAlso abbreviated as ‘μcon’ for short.

^eTeensy 4.X is suggested for any future receiver designs due to the anticipated permanent reduction in supply of the 90 nm silicon MK64FX512VMD12 chips constituent to the Teensy 3.5. Newer Teensy boards boasting 45 nm chips may also provide increased efficiency and capability in subsequent builds.



Fig. 2.17 The microcontroller unit control board with the Teensy board mounted at the left centre. The 48 V in, 12 V and 5 V out can be seen on the right of the board serving a portion of the overall microcontroller unit's power distribution functionality.

subsystems for ancillary device control such as the external fan.

Stacked above the controller board is the breakout board as shown in fig. 2.18 which is primarily responsible for the remaining front-end connections but also a 28 V noise source regulator, 6 V power supply and additional EMI filtering. A CAD rendering depicting the stacked microcontroller unit is also shown as fig. 2.19. The completed unit supplies power to every component within the front-end except for the thermal management system which has its own power supply unit as previously detailed. A combination of switched-mode power supply (SMPS) and linear regulators are employed to optimise both low noise and efficiency with the six DC-DC power supplies having an efficiency of at least 85%. A table detailing the power supplies managed by the microcontroller unit is shown in table A.3. Further conductive gaskets were placed under bulkhead connectors for additional noise reduction and additional DC filtering is provided on the 48 V input supply. A block diagram of the completed microcontroller unit is provided in fig. 2.20. The completed unit demonstrates a high efficiency with a 2 K temperature rise seen within the microcontroller casing with all supplies on at full load.

Temperature measurement via thermocouple

Within the receiver front-end are probes measuring the temperatures of various components needed for calibration. Initial designs utilised eight Microchip Technology MCP9808 temperature sensors that communicate directly with the microcontroller unit using I²C protocol over the Arduino command line interface. Thermal gap pads would be used to thermally bond the 2-centimetre-wide temperature sensors to front-end components yielding an accuracy of

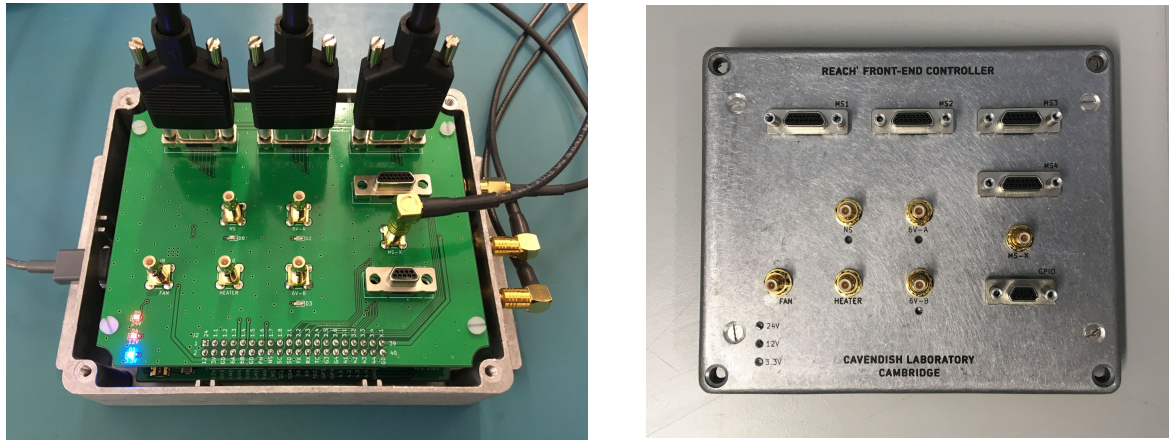


Fig. 2.18 The breakout board of the microcontroller is shown on the right displaying the mechanical switch connections across the top row. The remaining power supply connections can also be seen on the board. The top cover of the completed microcontroller unit is shown on the right with laser markings annotating the connections of the breakout board.

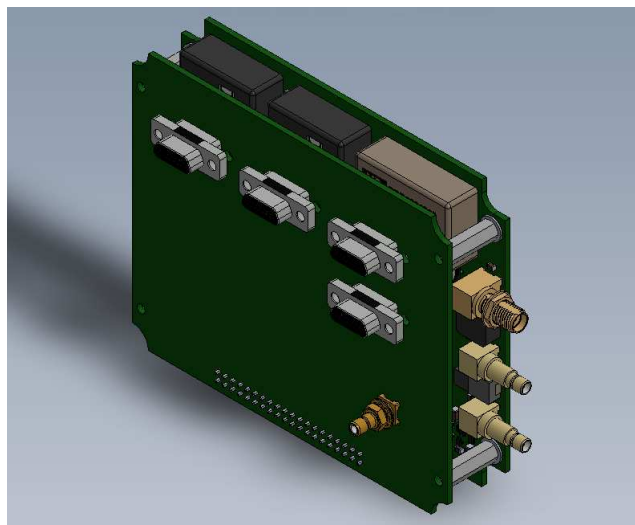


Fig. 2.19 A rendering of the microcontroller assembly showing the breakout board seated above the controller board both outside the microcontroller housing. Also not shown is a heat transfer bracket between the three converter modules. The staked design of the microcontroller allowed for the small form factor required by the REACH experiment.

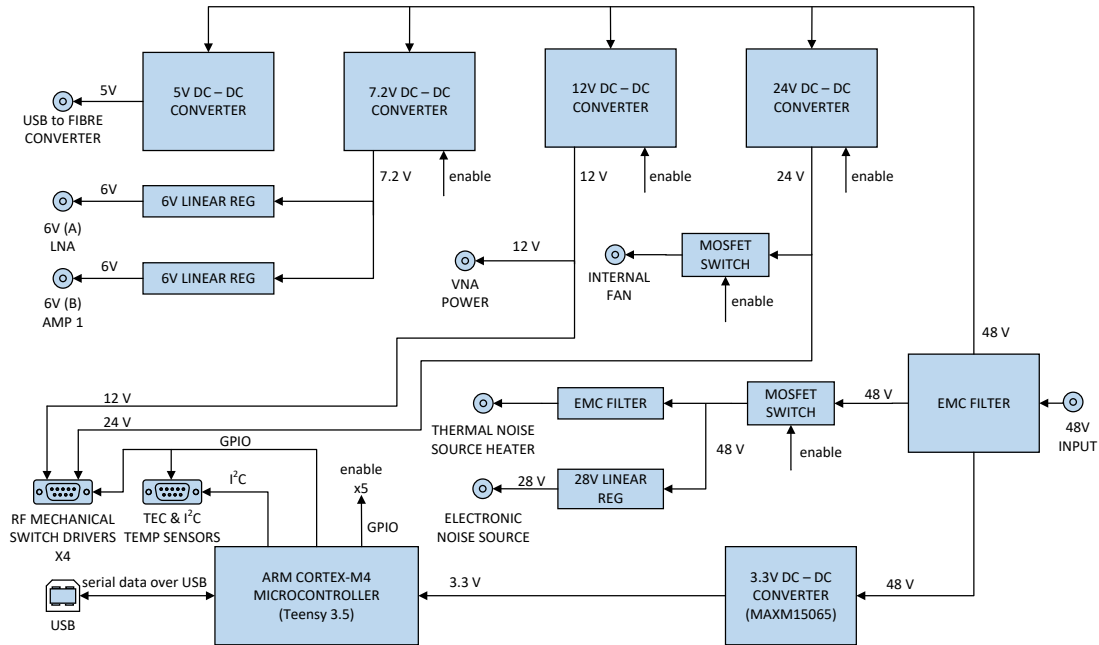


Fig. 2.20 A detailed microcontroller block diagram showing the components, connections and power considerations incorporated into the design.

± 0.5 K and measured with a cadence of I²C MEASUREMENT CADENCE HERE. The I²C sensors' native connection to the microcontroller unit conformed to the space restrictions of the front-end enclosure however, it was decided that smaller probe tips for placement on individual components as well as additional temperature sensors would increase the accuracy of our calibration prescription. A Pico Technology TC-08 Thermocouple Data Logger, shown in fig. 2.21, was employed to accommodate eight more temperature measurements using Pico Technology SE000 K-type thermocouples with TC-08 0.60 mm tip ends thermally bonded to components using RTV Thermally Conductive Oxime made by Electrolube. The simple



Fig. 2.21 The Pico Technology TC-08 Thermocouple Data Logger for use with eight K-type thermal probes.

TC-08 Port Number	Component
Port 0	Cold Junction
Port 1	MS1 switch
Port 2	Heated load thermistor
Port 3	MS3 switch
Port 4	MS4 switch
Port 5	2 metre calibration cable
Port 6	10 metre calibration cable
Port 7	Low noise amplifier
Port 8	Antenna (laboratory)

Table 2.2 The port assignments for the TC-08 connecting to various components within the receiver front-end. The Port 2 thermocouple was attached to the thermistor end of the simplified heated load construction. The Port 5 and 6 probes were connected directly to the outside of the calibration cables for measurement of the physical cable temperature with the terminating sources assumed to be at the same temperature as their respective switches. In the Cambridge laboratory, the Port 8 thermocouple was fed through a small hole drilled through the wall of the front-end enclosure and attached to the end of a makeshift antenna used for testing of the calibration algorithm.

incorporation of the TC-08 with our receiver automation software through the manufacturer’s proprietary Python libraries also factored into our decision to use the device. The TC-08 thermocouples have an accuracy of ± 1.1 K^f for our measurements typically around 300 K and relay information to the back-end server via USB connection at a cadence of one measurement every 10 seconds. A table of the TC-08 Data Logger port assignments is shown in table 2.2^g.

We highlight that Port 0 of the TC-08 lists a “Cold Junction” which is the temperature of the Data Logger unit itself and not the similarly named ambient temperature “cold” load. Furthermore, the position of the MCP9808 I²C temperature sensors were not finalised or thermally bound to anything by the time of deployment in August 2023 though it is envisioned that measurements of additional components needed for the temperature corrections detailed in TEMPERATURE CORRECTIONS CHAPTER are the primary responsibility of the I²C sensors. The temperature stability of various sources recorded by the TC-08 are shown in fig. 2.22.

^fSum of $\pm 0.2\%$ of reading and ± 0.5 K according to manufacturer specifications.

^gThese port assignments are representative of the front-end configuration at the time of shipment to South Africa in December 2022 and are subject to change.

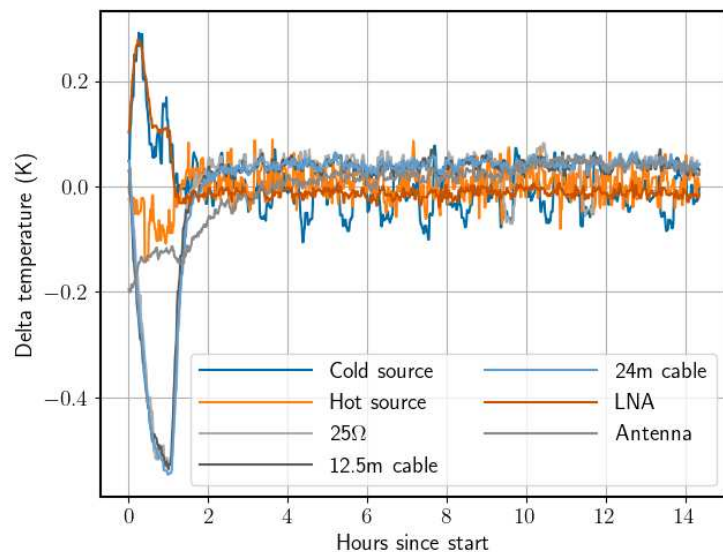


Fig. 2.22 Receiver component temperature stability recorded by the TC-08 Data Logger. The fluctuations seen within the first two hours of the measurements are from mechanical switch stabilisation and the VNA calibration procedure. We highlight the temperature stability of the individual components after environmental stability is achieved. The plot includes measurements of the 12.5 metre and 24 metre calibration cables before being replaced by the 2 metre and 10 metre cables as detailed in Calibration sources subsection.



Fig. 2.23 Copper Mountain Technologies TR1300/1 Vector Network Analyser. Image taken from Copper Mountain Technologies website.

Reflection measurement	Accuracy (Magnitude)
-15 dB to 0 dB	± 0.4 dB
-25 dB to -15 dB	± 1.5 dB
-35 dB to -25 dB	± 4.0 dB

Table 2.3 Manufacturer quoted measurement accuracies for the Copper Mountain Technologies TR1300/1 Vector Network Analyser.

Vector Network Analyser

Reflection coefficients of the calibration sources, LNA and antenna are measured with a Copper Mountain Technologies TR1300/1 2-port 1.3 GHz vector network analyser (VNA) shown in fig. 2.23. The main consideration for including this VNA model was the small $28.5 \times 14.2 \times 4$ cm form factor for inclusion in the front-end enclosure. The VNA measurement accuracy as provided by the manufacturer is shown in table 2.3.

Reflection coefficient measurements of various receiver components is shown in fig. 2.24. Upon inspection of table 2.3, one may note that the VNA is not rated for extremely low reflection measurements below -35 dB such as the ambient temperature and heated 50Ω loads shown in fig. 2.24. In order to quantify the quality of our measurements in this low-reflection regime, we use the manufacturer provided data of table 2.3 and calculate a spread in \pm dBs representing our measurement error for the regions our machine is rated for. We then convert this spread from dB to linear using

$$\text{measurement spread} = 10^{\frac{\text{measurement+error}}{10}} - 10^{\frac{\text{measurement-error}}{10}} \quad (2.2)$$

The linear measurement spreads are plotted in fig. 2.25 where we have fitted the manufacturer provided data with a decaying exponential using SCIPY.OPTIMIZE and extrapolated to the ranges applicable to the 50Ω loads. For reflection coefficient measurements ~ -45 dB, we find a linear measurement spread of 0.002 corresponding to a VNA accuracy of ± 10

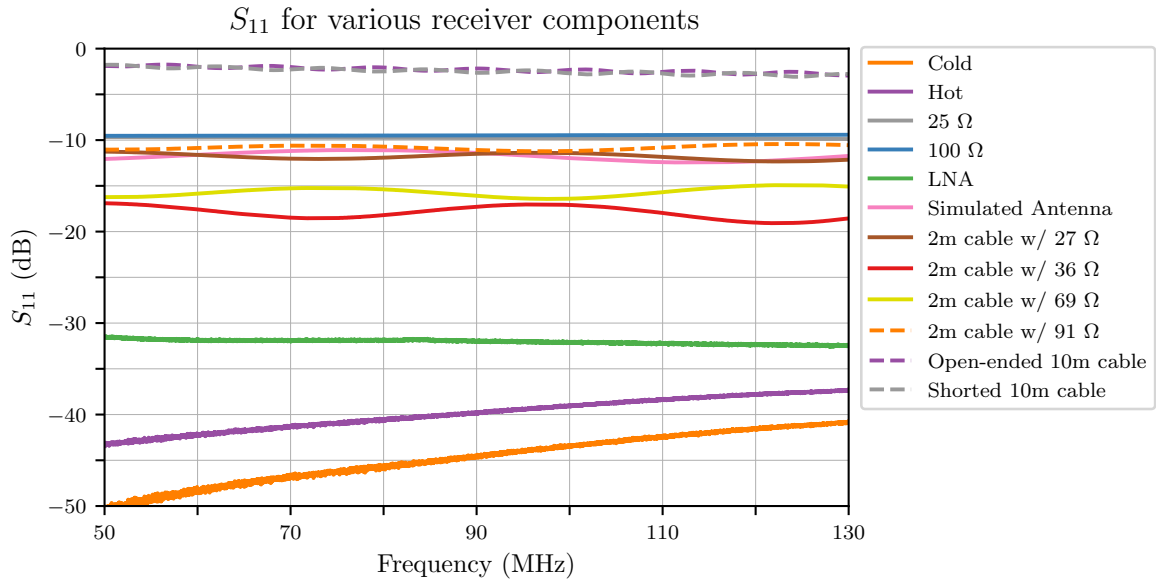


Fig. 2.24 Reflection coefficients for various receiver components including the LNA and simulated antenna.

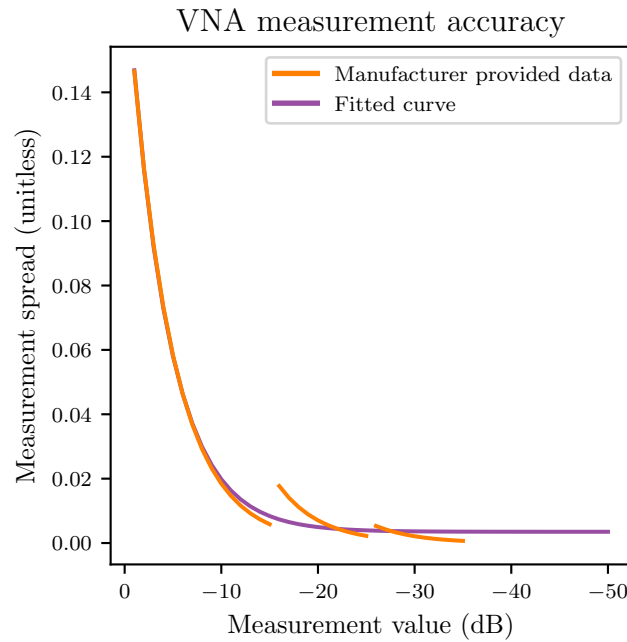


Fig. 2.25 VNA measurement spreads on a linear scale as a fraction of reflected power representing the measurement accuracy of the machine. Manufacturer provided data are shown in orange. A best-fit exponential curve to the manufacturer data is plotted in purple. The fitted curve asymptotes at a value of 0.002.

dB. In the logarithmic scale of dBs, this measurement accuracy is acceptable. A similar exercise of fitting a polynomial curve to the manufacturer provided data in the dB scale gives a similar but less conservative value for extrapolated measurement accuracy. We note that future iterations of the receiver front-end may benefit from inclusion of a VNA rated for low-reflection measurements but the small form factor of the TR1300/1 may be difficult to achieve.

A Python script using SCPI commands was developed in order to interact with and automate the VNA. This included a separate process to calibrate the VNA itself before proceeding with calibration of the receiver. VNA calibration was undertaken using short, open and load (SOL) standards from another Kirkby 85033 50Ω SMA calibration kit to maximise measurement accuracy of the reflection coefficients throughout a 50—200 MHz band. The VNA calibration is tested against an additional 50Ω test load that was measured in Cambridge with a Keysight N5247A PNA-X Network Analyser capable of providing some of the highest quality reflection measurements in the industry^h. A reflection coefficient of the test load measured by the TR1300/1 that deviates from the PNA-X measurement by more than 5% automatically triggers a re-calibration of the VNA before proceeding with calibration of the rest of the instrument.

USB-over-fibre connection

As briefly indicated in previous sections, the relay of instructions and measurement data from front-end components such as the TEC control module, microcontroller unit, TC-08 and VNA requires a USB connection to the satellite-linked server housed 100 metres away in the receiver back-end. To avoid RFI, signal loss or the logistical issues of constructing 100-metre-long shielding for a series of USB cable extenders, a 4-port Icron 2244 USB Rangerⁱ is used to convert USB data into fibre optical signals for transmission between the two nodes at up to 480 Mbps. Opting to mitigate any potential impact of distance-dependent signal dispersion or degradation, a phenomenon commonly observed in multi-mode fibre optic connections spanning over 500 metres, single-mode fibre optical connections were specifically chosen to ensure signal preservation despite the relatively short distance of 100 metres. Powered by the microcontroller unit, the 5 V USB Ranger is held in place by a custom 3D printed bracket and outputs through a single-mode fibre port installed on the front-end enclosure as labelled in fig. 2.2.

^hThe 49 kg PNA-X, with a size of 649 × 482 × 280 mm, unfortunately proves to be too large for in-field deployment.

ⁱAs this model is now a legacy device, the Icron 2344 USB Ranger is expected to be used for any future receiver builds.



Fig. 2.26 Interior of the completed REACH low noise amplifier custom designed for a flat spectral response in both S_{11} and noise.

RF signal chain I: Low noise amplifier

Cosmic radio signals detected by the antenna are generally weak and need to be amplified to measurable levels. Because random electrical noise from instrumental components would also be magnified by across-the-board amplification, several stages of low-level, more precise amplification are needed to preserve any celestial signatures. The primary ‘preamplification’ stage of the RF signal chain is commonly managed by a ‘Low Noise Amplifier’ (LNA) which is tasked with amplifying incoming signals while adding a minimal amount of noise.

An inspection of typical noise figure circles from RF transistor datasheets indicate a general trade-off between maximal noise figure and perfect impedance matching. For REACH, we have opted to prioritise impedance matching in our design to minimise reflections producing the noise waves necessitating calibration. The resulting LNA is therefore not particularly low-noise, but this is anticipated to have a negligible impact on the REACH experiment due to long integration times serving to counteract sensitivity limitations. It is expected that the REACH system will be sky noise dominated in the 60–120 MHz regime where the dipole is best matched with reduced sensitivity at frequencies greater than 120 MHz.

With the design objectives of an amplifier input reflection coefficient (S_{11}) less than -30 dB as well as a low gain variation with temperature, several amplifiers were assessed before ultimately selecting a pair of Mini-Circuits CMA-84+ SMT gain blocks followed by attenuators to realise an exceptional input matching along with a spectrally flat passband response. The completed LNA, shown in fig. 2.26 ultimately achieves a flat 5.1 dB noise figure within the REACH observational band of 50–170 MHz.

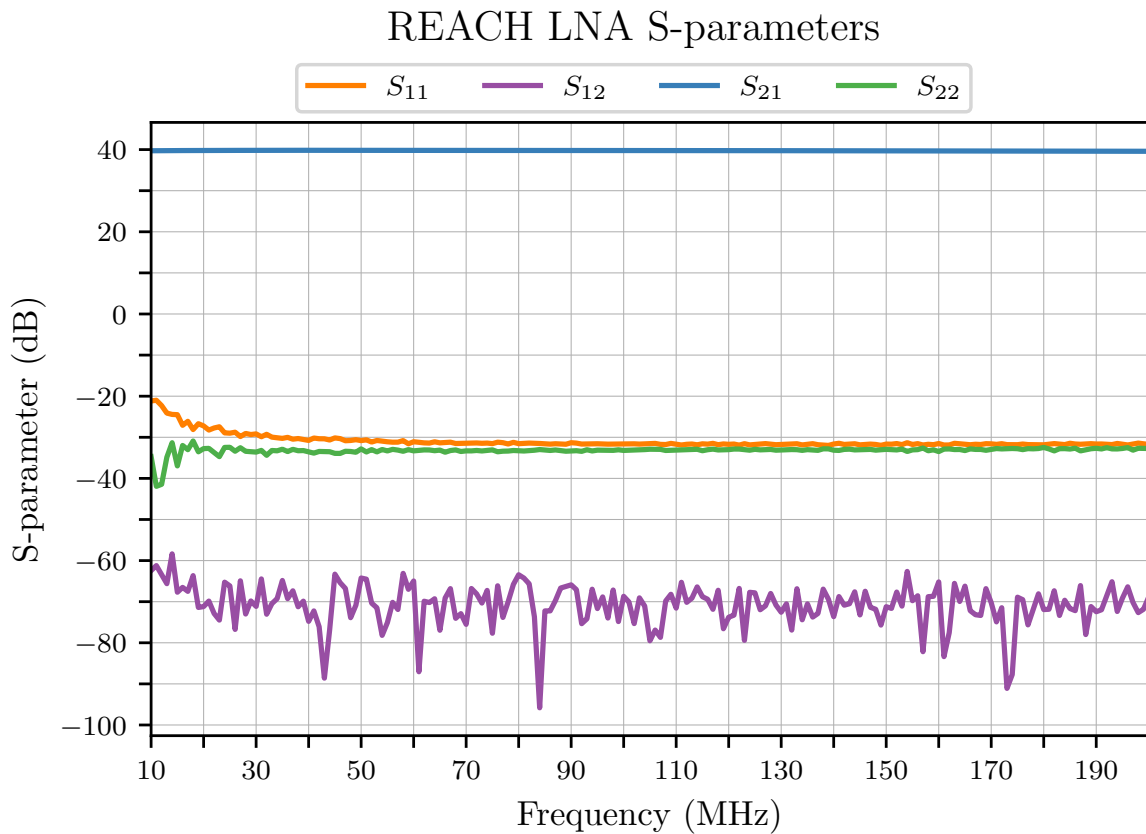


Fig. 2.27 Measured S-parameters of the REACH LNA showing a good match at -30 dB for the S_{11} and S_{22} across the REACH observation band (shaded region) while demonstrating exceptional gain stability (S_{21}).

While an alternative LNA built instead with Mini-Circuits ERA-50SM+ gain blocks exhibited a better noise figure of 3.3 dB, the CMA-84+ construction demonstrated a better stability in both S_{11} and temperature. Reflection coefficients of the finalised LNA are plotted in fig. 2.27 showing the desired S_{11} less than -30 dB which is well matched across the observational band as well as a remarkably flat 40 dB gain response.

RF signal chain II: Amplifier #1

The second stage of spectral data amplification uses another custom module called ‘Amplifier #1’, or AMP1^j. Incoming signals from the LNA are further amplified using a Mini-Circuits GALI-S66+ limiting amplifier and a PHA-13LN+ mid-power amplifier in combination to achieve maximal dynamic range followed by high-pass filtering using a Mini-Circuits RHP-

^jLike all good computer scientists, we have numbered our amplifiers using a zero-based system with the LNA, AMP1 and AMP2 being amplifiers number zero, one and two respectively in the RF signal chain.



Fig. 2.28 The REACH AMP1 module used for further amplification and filtering of signals. Seen on the right end of the construction is the fibre optic conversion printed circuit board connected to the single-mode FC/APC RFoF transmission connector seen in yellow.

44+ filter to attenuate frequencies below the observation band. A 2-stage Mini-Circuits XLF-42M+ monolithic microwave integrated circuit (MMIC) then low-pass filters out-of-band signals above the observation band up to many GHz.

Serving as the internal circuit boundary of the front-end receiver, AMP1 converts signals to Radio-Frequency-over-Fibre for transmission to the receiver back-end minimising the effects of RFI and signal loss that would be typical of alternative connections such as coaxial cables. The passive 1310 nm RFoF converter was made under commission by Polycom according to the specifications for the HERA experiment and has an 18 dB loss due the relative intensity noise of the optical transmission laser which is addressed by 70 dB of upfront gain to reduce the impact of higher noise on the system. The optical transmitter subassembly (as well as the corresponding back-end optical receiver) are printed circuit boards terminated in Fibre Channel/Angled Physical Contact (FC/APC) connectors at the end of a 0.5 metre pigtail as seen in fig. 2.28. The FC/APC connector links to the RFoF port installed on the front-end enclosure as labelled in fig. 2.2 which connects to an extended roll of fibre optical cabling reaching the receiver back-end. Single-mode fibre optics are again used to prevent signal degradation as with the USB-over-fibre connection. We find the radio-frequency loss of the RFoF bridge over the 100 metre distance to be less than 1 dB including the connections at both ends. A full circuit diagram of amplifier #1 including the RFoF transducer is shown in fig. A.2.

Completed receiver front-end unit

The deployable receiver front-end unit was completed in December 2022 and is shown in fig. 2.29. The finalised construction weighs 29 kilograms and, as stated previously, is allocated a maximum of 135 W for total front-end power from the solar panels. Control and

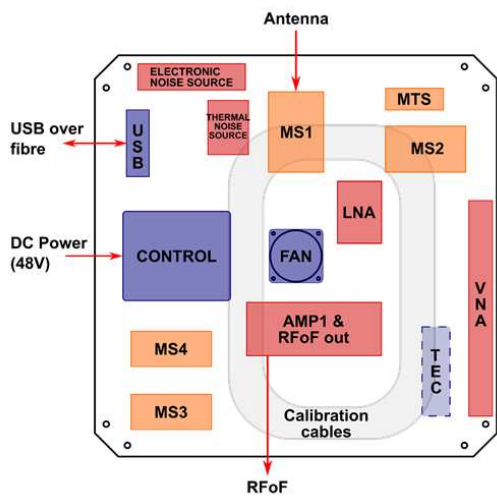


Fig. 2.29 The completed receiver front-end unit (right) along with a layout diagram showing the approximate positions of various components (left). Shown in the image are the compact VNA on the bottom right and the TC-08 module in the centre with green thermocouple probes. The stadium housing the calibration cables is seen around the TC-08 and obscures the amplifiers and TEC. The various cylinders are the multi-input switches connected to calibration sources. The microcontroller unit can be seen on the middle-left and is powered on as shown by the LED's. The USB over fibre link and diode noise source are shown in the top left corner.



Fig. 2.30 The receiver front-end in its natural environment, deployed at the REACH experiment site in the Karoo Radio Astronomy Reserve, South Africa. Image credit: Dr. Saurabh Pegwal

RF circuitry require about 31.5 W with the remaining 103.5 W left for cooling through the TEC. The majority of the engineering work went into construction of this receiver front-end and is expected to be deployed as a portable, energy efficient system with accurate in situ calibration through internal environmental control while maintaining the highest quality measurement capabilities and RFI mitigation. Also included are various ferrite beads to limit control and power signals from intercepting the RF signal path and were generally placed through trial-and-error. Subcomponents along the signal chain are connected with RG-402 semi-rigid cables to prevent cable flexing during transportation. A second 1:1 replica of the receiver is currently being built in Cambridge to assist in remote triage expected during deployment and design changes are being considered for future front-ends to accommodate additional antennas. A picture of the receiver front-end deployed on the REACH site in South Africa is shown in fig. 2.30.

2.1.2 Receiver back-end

The receiver back-end houses the components critical for remote communication away from the deployment site, power distribution to the instrument as a whole and measurement subsystems that are less sensitive to environmental effects. 100 metres away from the dipole antenna, the receiver back-end sits below ten MODEL NUMBERS solar panels rated to give SPECIFICATIONS HERE as diagrammed in fig. 2.1. This distance was chosen to avoid radio-frequency reflections off the solar panel and back-end faces as well as serving



Fig. 2.31 A conceptual CAD rendering used as a reference for the REACH back-end RF-EMC enclosure is shown on the left exhibiting various custom assemblies for use in the South African Karoo such as ventilation paths and interference mitigation. The right image shows the completed receiver back-end rack housed inside the RF-EMC enclosure. Rack components such as the amplifier and spectrometer assembly (large silver module), ventilation and power distribution units can be seen.

as a potential central node to be equidistant from future antennas. Under the solar panel construction is a radio-frequency electromagnetic-compatibility (RF-EMC) enclosure custom made by Interference Testing and Consultancy Services Ltd. to mitigate the effects of external RFI on our measurements as well as any potential EMI leakage from our own instrument that may be picked up by nearby experiments. Designs for the RF-EMC enclosure were informed by similar constructions used with the HERA experiment that incorporate considerations of the on-site environment as well as compliance with the EMC requirements of the Karoo Radio Astronomy Reserve. A conceptual diagram of the RF-EMC enclosure is shown in fig. 2.31.

Within the RF-EMC enclosure are the various back-end modules mounted on a 36-inch rack^k also shown in fig. 2.31 which includes modules for additional signal amplification, conditioning and digitisation, the spectrometer for measurement of power spectral data, the back-end server and GPS system for remote communication and automation of the device,

^kA StarTech 22U 36in Depth Enclosed Server Cabinet was used in Cambridge but not shipped for deployment.

as well as power distribution and cooling units as detailed in this section. The back-end RF-EMC enclosure is accompanied by a smaller similar chamber to house various additional units such as a 7400 Wh SS202 Lithium Iron Phosphate battery made by Solar MD for overnight power storage from the solar panels or during periods of non-ideal weather. This smaller chamber is shown in fig. A.3 for reference but is not strictly a part of the receiver back-end.

RF signal chain III: Amplifier #2 and out-of-band injection

The first device in the receiver back-end is our third stage of amplification with Amplifier #2 (AMP2). Upon entering AMP2, the RFoF signal from the front-end is converted back into an RF signal by the optical receiver, again constructed with an FC/APC connection to a Polycom printed circuit board mounted to the AMP2 module. The next task of AMP2 is to continue filtering the signal using another Mini-Circuits XLF-42M+ 2-stage MMIC low-pass filter to block high-frequency out-of-band signals. To sharply filter signals outside the REACH observational band (above 170 MHz), a custom 11-order Cauer Chebyshev low-pass filter was designed using a series of five 1812SMS air core inductors made by Coilcraft as shown in the circuit diagram fig. A.4. Following this, the signal is amplified using two more Mini-Circuits GALI-S66+ and PHA-13LN+ amplifiers, as used in AMP1, to achieve best dynamic range prior to the analogue-to-digital converter (ADC) within the iTPM spectrometer module. Low-loss 3 dB Mini-Circuits RCAT-03+ equalisation circuits are also used throughout AMP2 to flatten the passband to 2 dB. The final sub-component of AMP2 is a power splitter to output two equal signals from the module with one path going to the ADC/spectrometer unit and the duplicated signal available for additional devices such as another ADC or a power meter for remote monitoring as done with the HERA experiment.

Supplementary to AMP2 was an optional module for out-of-band continuous wave or filtered noise signal injection to condition the ADC. This unit was built to inject a constant power (adjustable through the inclusion of attenuators) at 10 MHz and is band limited to DC–20 MHz, strictly outside the REACH observational band as not to contaminate the measurement. An example of the injected out-of-band noise from this module is shown in fig. 2.32, though this feature was not used in the final deployed system as it provided no tangible improvements to the data as discussed in the THINGS THAT DIDNT WORK SECTION. The completed AMP2 and out-of-band injection unit are shown in fig. 2.33 which represent the final components of the RF signal chain.

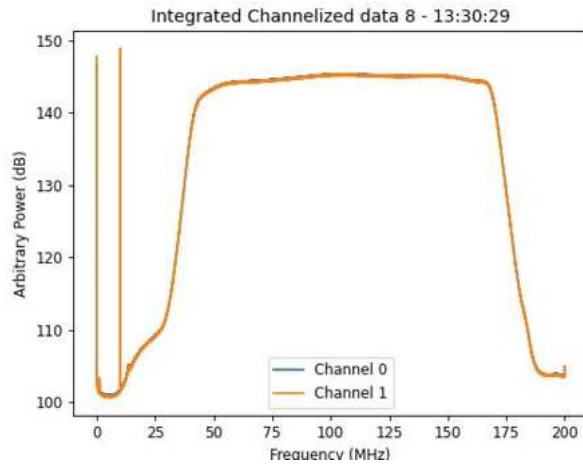


Fig. 2.32 A power spectral measurement of the ambient temperature 50Ω load with the out-of-band noise injection module activated. A constant power is injected at 10 MHz and can be used to assess the accuracy of the spectrometer reading as well as condition the ADC for low-power signals. Attenuators were used to prevent signals resonant to the 10 MHz injection from intercepting the in-band measurements. The spike at 0 MHz is an artefact of the spectrometer and receiver architecture and is not considered a hazard to the measurement.



Fig. 2.33 The completed Amplifier #2 (left) and out-of-band noise injection module (right) for inclusion in the receiver back-end. The ‘Fibre In’ port on AMP2 connects to the RFoF link from the front-end and the power splitter outputs identical signals to the ports labelled ‘Outputs’. The ‘Noise Output’ ports from the noise injection module would connect to the ‘Noise In’ port of AMP2 though this is not currently applied to measurements in the field.

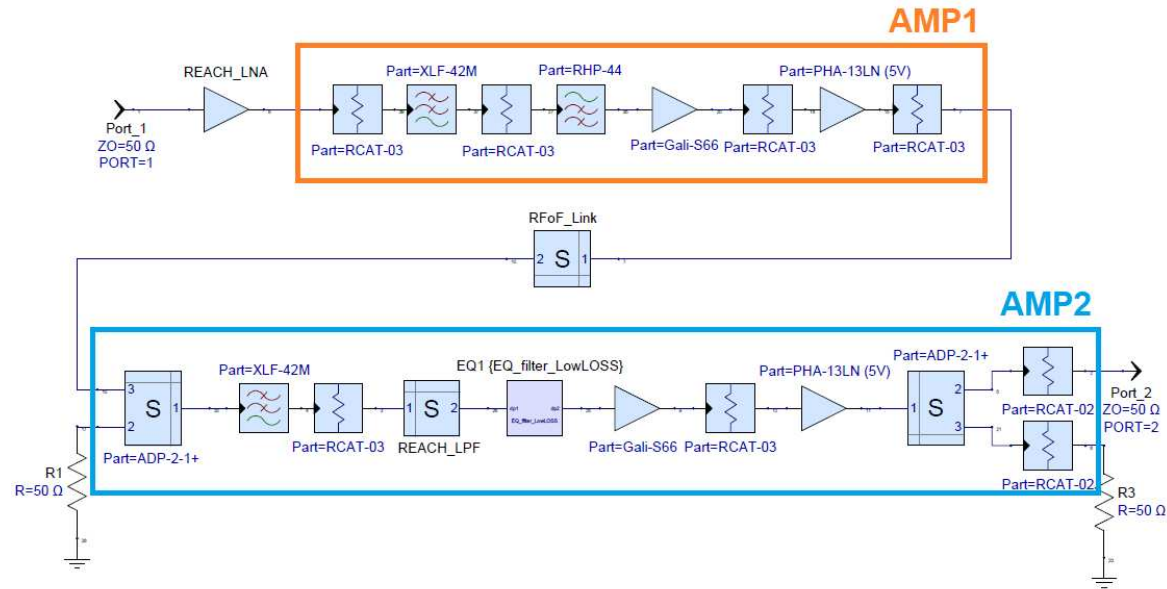


Fig. 2.34 REACH RF system end-to-end block simulations made with the Keysight PathWave RF Synthesis software showing the LNA, AMP1, AMP2 as well as the RFoF link.

RF signal chain IV: Simulations

Within the design process of the RF signal chain components; the LNA, AMP1 and AMP2, were various stages of optimisation and fine-tuning. Constituent elements within the LNA were first simulated then built and measured with the PNA-X as shown in fig. 2.27. This data was then imported back into the simulation to further inform the development of the signal chain as a whole. Simulations were undertaken using the Keysight PathWave RF Synthesis software (formerly known as Genesys) with the in-program optimisation tool used to optimise filter design. Both linear analysis and the Keysight Spectrasys RF System Simulation software were also employed for RF budget simulations with other components simulated using Modelithics' substrate scalable models. Also included in the simulations were measurements the AMP1 optical transmitter, AMP2 optical receiver and 100 metres of single-mode fibre, characterised by the VNA at different power levels and added to the simulation as a single block as shown in fig. 2.34 which replicates the complete RF signal chain. The results of the full RF signal chain simulations are shown in fig. 2.35 where we highlight the flat noise figure of the network over the observational band.

Spectrometer

Following the amplification stages is the Sanitas EG *italian* Tile Processor Module (iTPM) shown in fig. 2.36 which serves as an analogue-to-digital converter (ADC) and a high-

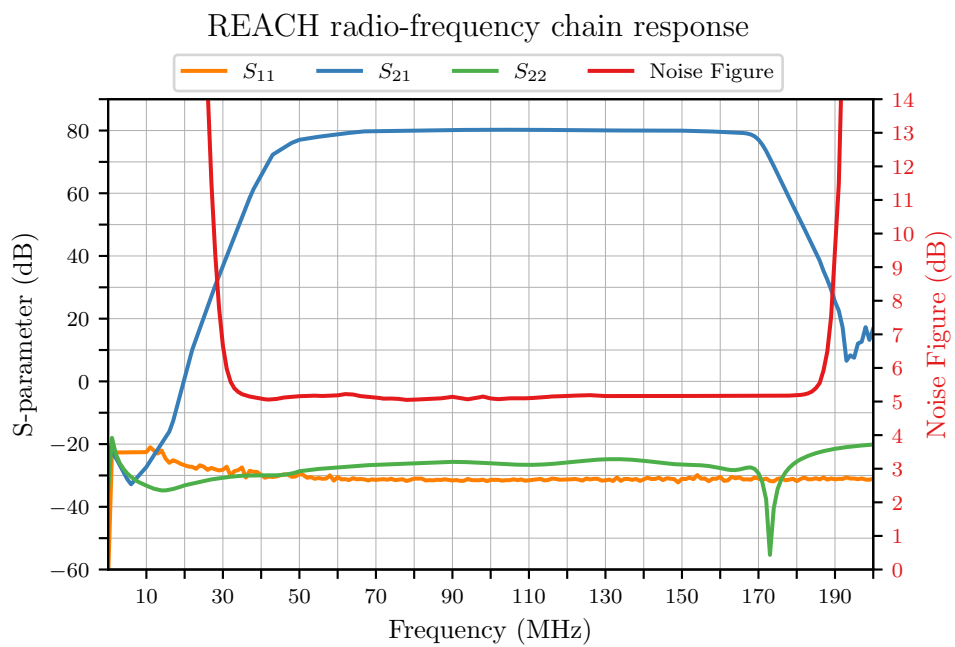


Fig. 2.35 Simulated radio-frequency response of the REACH end-to-end signal-chain as diagrammed in fig. 2.34 which includes the LNA, AMP1, AMP2 and RFoF modules. VNA measurements of the LNA have been included in this simulation as well. The shaded region represents the REACH observation band where we see a flat noise figure throughout. Adapted from figure included in REACH NATURE PAPER.



Fig. 2.36 The Sanitas EG Italian Tile Processor Module for conversion of analogue signals to digital as well as spectral measurements.

resolution ultra-wideband digital spectrometer. This device was chosen for its development under the Square Kilometre Array experiment as part of the Low Frequency Aperture Array and has been used for verification of an SKA1 station as well as for back-end signal processing in other experiments [47]. The iTPM's design targeting similar EoR signals granted easy reconfiguration for the REACH experiment through the reuse of auxiliary functions such as control, monitoring and data acquisition. Conversion of the incoming analogue signal to digital is undertaken using sixteen dual-channel Analog Devices 14-bit AD9680 ADCs allowing for multiple data streams from additional proposed antennas as detailed in the FUTURE WORK SECTION. At the time of deployment, two ADC channels were initialised as seen in the fig. 2.32 legend for the two antennas expected to be built with the remaining ADC channels disabled to save power. Analogue signals are digitised at 400 MSPS using 16,384 channels at 12.2 kHz per channel. After conversion, spectral measurements are taken by two AMD XILINX UltraScale XCU40 field-programmable gate arrays (FPGAs) each customised to process a single digitised RF signal using a full floating-point fast Fourier transform (FFT), power integrator and polyphase filter bank incorporating 229,376 tap coefficients downloadable to the FPGA to allow the implementation of different weighting functions without recompiling the FPGA firmware. Spectra are accumulated over a number of FFT frames corresponding to an integration time of approximately one second which are then transmitted to a processing server via Ethernet connection where further accumulation can take place on the order of minutes. A typical spectrum obtained from a 20-minute integration on the 50Ω cold load is shown in fig. 2.37. The 90 dB channel isolation of the spectrometer is expected to be useful for RFI excision. While on-site RFI measurements are

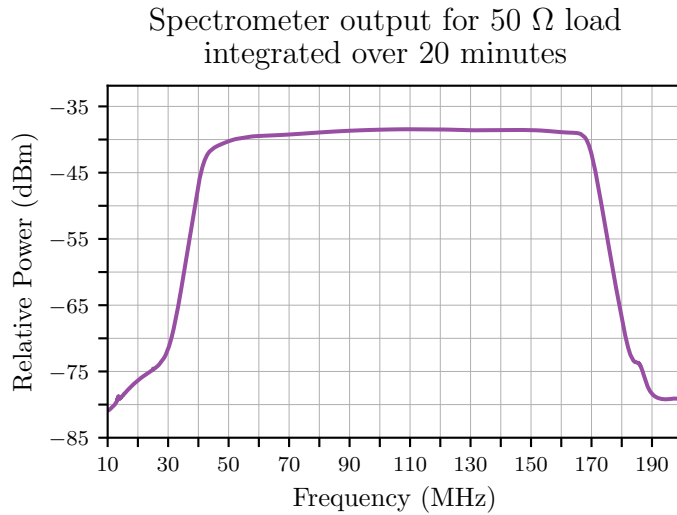


Fig. 2.37 A spectra taken by the iTPM of the ambient temperature 50Ω load integrated for 20 minutes using the finalised receiver system. A stable power measurement is seen within the REACH observational band (shaded region).

still needed to confirm this, data from co-located experiments such as HERA suggest that the current channel isolation is adequate.

Readout enclosure

The readout system comprised of AMP2, the digitiser and spectrometer is housed in a custom-built 6U¹ metal enclosure as shown in fig. 2.38. Included in the readout enclosure are installations for two USB power meters to independently monitor absolute power levels in the field as previously detailed as well as slots for the out-of-band noise injection module and two independent Amplifier #2 modules to accommodate two antennas in the field. Semi-rigid RG-405 connect the AMP2 outputs to iTPM channel inputs allocated individual panels seen in fig. 2.38. Within the enclosure is an off-the-shelf Peltier heat exchanger, fan and insulation to help regulate the temperature of the readout system, though the back-end components are subject to less scrutiny for operating temperature and output directly to the communication server via RJ45 cabling. Also seen on the front panelling are timing inputs to connect the iTPM to the GPS unit as detailed in the next subsection.

GPS unit for TPM synchronisation

Tile processor modules, such as the one used in our readout system, are comprised of a series of processing units referred to as ‘tiles’ which work in tandem to perform tasks efficiently.

¹housing height of six standard rack units approximately equal to 266.7 mm



Fig. 2.38 The readout enclosure housing the receiver components needed for digitisation and spectral measurements of radio-frequency signals.

For precision applications, synchronisation among tiles is crucial for overall performance and a reference oscillator is needed to provide a common clock signal coordinating the timing of operations across different tiles. As we do not know the environmental effects of the deployment site on the iTPM's internal oscillator *a priori*, we use an external Thunderbolt E GPS disciplined clock made by Trimble to ensure iTPM tiles operate in harmony. The Thunderbolt E links to a proprietary GPS antenna through a 75Ω Belden 1189A cable which allows the module to communicate with the global positioning system to generate a 10 MHz oscillation which is used as a reference to produce a 400 MHz clock to set the ADC sampling rate of 400 MSPS. The module then relays a pulse per second (PPS) signal to synchronise the ADCs to ensure coherence. The GPS disciplined clock was chosen over alternative atom-based frequency standardisation modules to ensure the reference clock accuracy, and in turn the sampling clock accuracy, is isolated from environmental effects, damage during transport, or interference generated by our own receiver components. This would in theory increase accuracy by limiting the propagation of delayed clock signals across tiles (known as skewing), and small variations in clock signal timings (known as jitter). Furthermore, a single reference should be used when using multiple TPMs, as may be the case in the future, to avoid slightly different sampling rates based on individual oscillators. Users of the receiver back-end should note that the 10 MHz GPS signal is independent from the 10 MHz out-of-band noise injection and are urged to be aware of the similarly-named labelling throughout the instrument. The Trimble Thunderbolt E as well as its GPS antenna are shown in fig. 2.39.



Fig. 2.39 The Trimble clock discipline system consisting of the Thunderbolt E reference signal generator (left) and GPS antenna (right).

Server & additional back-end units

To permit communication between the instrument and users at Cambridge, a Lenovo M920q Tiny ThinkCentre with a ninth generation Intel i7 core is included in the receiver back-end as a server. Xubuntu was chosen as the server operating system as the Xfce desktop environment uses fewer system resources in the field while retaining the flexibility and ease of use of Ubuntu^m. The ThinkCentre's visual output connects to an ATEN CL6700 MW Single Rail LCD Console with built-in monitor keyboard and trackpadⁿ for in-person interaction with the machine during installation, triage and site trips when network connection may not be available.

USB links between the server and receiver components is achieved with a StarTech MODEL NUMBER 10-port USB hub with its primary function of receiving the USB over fibre signal from the front-end through the Icron 2244 USB Ranger's optical-to-USB transducer. As detailed in section 2.1.1, this allows for the collection of reflection coefficient and temperature data as well as transmission of instructions to the microcontroller and front-end thermal management system. Additional ports on the StarTech USB hub connect the server to the back-end TEC controller for the Peltier device within the readout enclosure as well as a Penn Elcom FT01-Q module consisting of three rack-mounted fans for airflow and cooling within the receiver back-end. Finally, the USB hub connects the server to a Netgear ProSafe M4100-D12G Ethernet managed switch for control of further components via RJ45 connection. Connected to the Ethernet switch is the readout system output, permitting the collection of spectral data from the iTPM as well as connection to a Tripp Lite PDUMH15HVNET Ethernet controlled power distribution unit allowing users to toggle power for individual

^msorry Arch users...

ⁿAlso referred to as a 'KVM' console for 'Keyboard, Video & Mouse'.



Fig. 2.40 The completed receiver back-end installed in the 36-inch rack in Cambridge (minus the RF-EMC enclosure). The custom readout system weighs in at 15.89 kilograms and is central to the experiment's data acquisition. The Ethernet switch and power distribution units can be seen and are controlled by the Lenovo server. This unit would be common to any additional antennas deployed to the field and is generally less sensitive to environmental effects on site.

devices throughout the receiver back-end. The Ethernet switch will also be connected to the satellite uplink intended to be installed after the receiver back-end but not finalised at the time of writing. A second PDU was included in the deployed back-end but is not used. Tables specifying the connections of the USB hub, Ethernet switch and back-end PDU are given in table A.4, table A.5 and table A.6 respectively for reference.

Completed receiver back-end unit

The receiver back-end was also finished in December 2022 and is shown in fig. 2.40. The completed build was too large to be shipped practically and was disassembled into its constituent submodules before being sent to South Africa in February 2023 and reconstructed using a different standardised rack. This finalised construction is intended to serve as a central node for the REACH experiment including any further antennas to be deployed on site. As much of the receiver back-end consists of off-the-shelf components, we expect serviceability and part replacement to be more straightforward than the front-end. A diagram indicating the back-end submodules is shown in fig. 2.41.

2.1.3 Automation

The nearest settlement to the REACH deployment site in the Karoo Radio Reserve is Carnarvon, about 90 kilometres away and about seven hour's drive from the central international

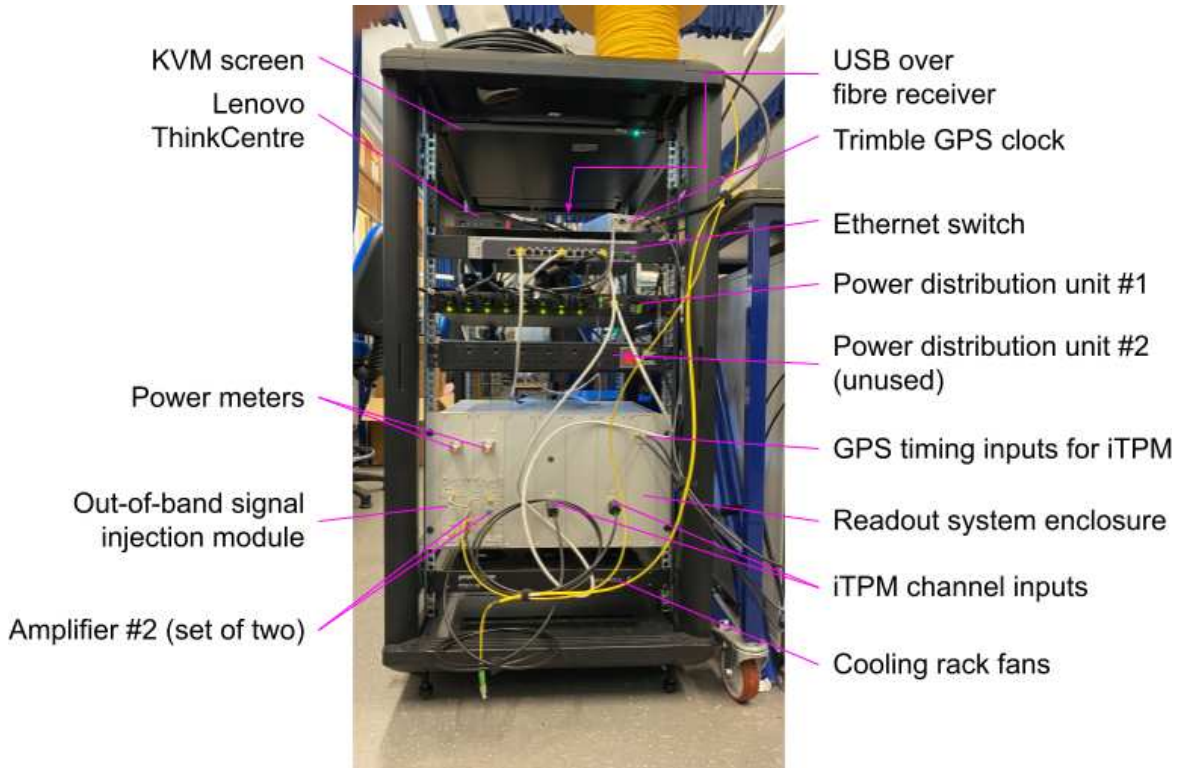


Fig. 2.41 A diagram specifying the placement of the various back-end components for the completed unit in December 2023.

airport in Cape Town. Such isolation made the development of a fully autonomous instrument a necessity and procedures were developed to facilitate remote access and communication with the device. In our procedure, the receiver front-end(s) and back-end are controlled and monitored by our management software running on the Lenovo processing server which oversees operation of the instrument such as the configuration of hardware components, data management and directing subroutines. Within our management software, a variety of different communication protocols are used. The Python FPGA Board Interface Layer (Py-FABIL) is used to interact with the iTPM while the Standard Commands for Programmable Instruments (SCPI) protocol is used to contact the VNA. Proprietary USB protocols in a Python wrapper are used by the TC-08 temperature sensor with the TEC needing an additional proprietary Windows-based Application Programming Interface which entails a virtual machine running in our Linux desktop environment. Signal path configuration through the microcontroller unit is assigned to Teensy ports accessed through a command line serial interface. A crib sheet useful for the development of automated procedures such as an observation schedule is shown in fig. 2.42 which details the specific devices contactable through individual microcontroller ports.

Both the calibration and observation procedures are managed by a YAML configured scheduler allowing a remote operator to specify a sequential list of operations including switch toggling, reflection coefficient or spectral measurement, the VNA calibration and hardware initialisation among other low-level commands for debugging purposes. General prescriptions are provided for the two main operations, the first of which is calibration. During calibration, the instrument is instructed to first calibrate the VNA through measurement of the S-O-L standards as detailed in section 2.1.1. Following this, a measurement of the 50Ω test load is compared to a saved file from the PNA-X on a frequency-by-frequency basis. If the VNA measurements are within a user-defined tolerance (usually 5%), the instrument proceeds with receiver calibration measurements; S_{11} , spectra and temperatures of the calibration sources along with an S_{11} measurement of the LNA. This data is fed into the calibration algorithm to generate calibration coefficients which are verified through comparison with a benchmark set of coefficients to within a user-defined tolerance (e.g. previous calibration coefficients to within 5%).

Following this is the second primary mode of operation; observation. During observation, power spectral measurements of the sky, reference load and reference noise source as part of the Dicke cycle are performed by the YAML-configured schedule started by a local sidereal time (LST) trigger. Additional measurements of the test load are taken to support ad hoc debugging procedures after which RFI in the data is flagged by a separate algorithm. Calibration coefficients derived in the calibration routine are then applied to the data before

Teensy port	Net name	J4 connector	Net name	Teensy port
22	+12V	12V	24	+24V
ALWAYS ON	+3.3V	3V3	1.1	MS1-1
GND	GND	GND	1.2	MS1-2
5	+6V_A	6VA	1.3	MS1-3
5	+6V_B	6VB	1.4	MS1-4
GND	GND	GND	1.5	MS1-5
20	INT_FAN	FAN	1.6	MS1-6
6	NS_PWR	NS	1.7	MS1-7
SCL0	SCL0	SCL	1.8	MS1-8
SDA0	SDA0	SDA	2.1	MS2-1
RX1	TEC_TX	TX	2.2	MS2-2
TX1	TEC_RX	RX	2.3	MS2-3
2	TEC_EN	TEC	2.4	MS2-4
3/SCL2	GPIO3	GP3	2.5	MS2-5
4/SDA2	GPIO4	GP4	2.6	MS2-6
9	MS4-1	4.1	3.1	MS3-1
10	MS4-2	4.2	3.2	MS3-2
11	MS4-3	4.3	3.3	MS3-3
12	MS4-4	4.4	3.4	MS3-4
GND	GND	GND	X.1	MTS
5	6V_EN	n/a	5V_EN	ALWAYS ON

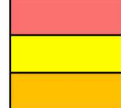

 Power supply
 Requires +12V enabled
 Requires +24V enabled

Fig. 2.42 A reference sheet listing the front-end component assignments to the Teensy input/output ports for use in receiver automation. Individual switch positions, power supplies and components can be seen facilitating the creation of new automated routines and on-the-fly system interaction via command line interface. MS‘N’–‘P’ refers to mechanical RF switch number N, port P. ‘MTS’ is the mechanical transfer switch. ‘TEC’ is the thermo-electric cooler module.

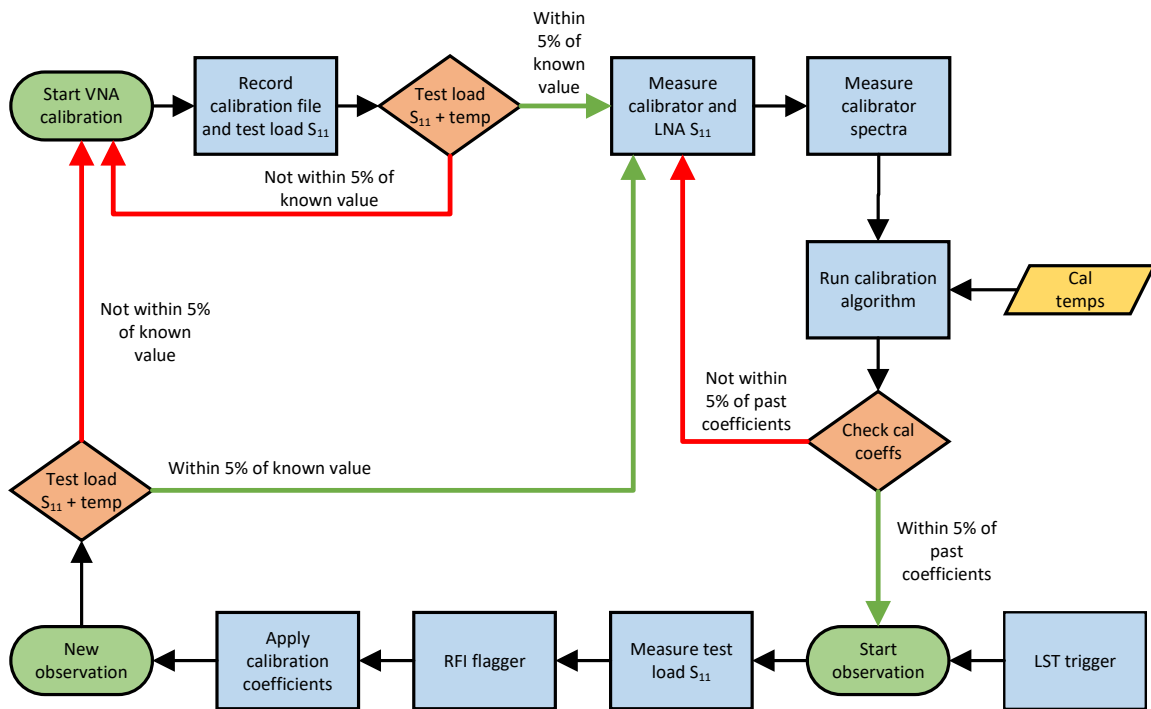


Fig. 2.43 Typical REACH calibration and observation loop including calibration of the VNA and receiver as well as data acquisition, checks and processing such as RFI flagging. Various stages are verified via algorithm before proceeding to the next process.

being set for data processing. A flowchart depicting the general steps of instrument operation is shown in fig. 2.43.

The receiver back-end transmits integrated spectra as Streaming Protocol for Exchanging Astronomical Data User Datagram Protocol (SPEAD UDP) packets over a 1 GbE network to be received by the associated spectrometer module. A software monitoring daemon collects temperature and power information every minute which is stored in a metric database which are included as metadata with calibration and observation data to inform the calibration procedure. The generated data is then stored as an HDF5 file which includes spectra and reflection coefficients with associated timestamps along with temperature sensor readings. The HDF5 files are self-describing, containing all the information required for future processing without having to refer to observation schedules or similar documentation. The HDF5 files then are transferred off-site to a centralised storage system through a satellite network link installed on-site. An plot of power spectral data taken remotely from Stellenbosch University in South Africa is shown in fig. 2.44.

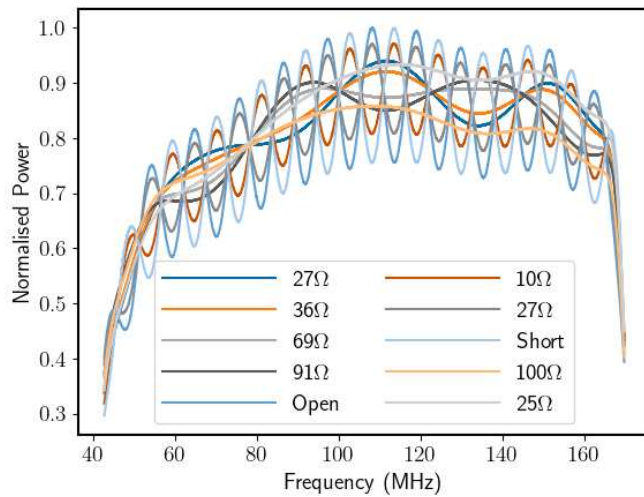


Fig. 2.44 Passband measurements of several calibration sources taken remotely through an automated procedure. The spectral data shows a clean frequency response with small RFI spikes at lower frequencies which will need to be processed by the separate RFI flagger.

2.1.4 Deployment

Throughout 2022, the deployment site in South Africa was prepared while receiver development took place. Ditches were dug for support posts to be placed for the raised ground plane mesh suspended by guide wires. Due to natural land slope on site, the ground plane was erected between 1 metre and 1.2 metres above ground level to maintain a level construction. Support structures were built and the antenna was then installed as shown in fig. 2.45. Upon being shipped from Cambridge, the receiver front and back-ends underwent strict electromagnetic compatibility (EMC) testing at the Karoo radio reserve under the same level of scrutiny as co-located experiments such as HERA. After a final round of testing by the REACH team, the receiver was transported to the deployment site in August 2023 where the back-end components were installed as shown in fig. 2.46.

It was understood that at some time between shipment from Cambridge and deployment in the field that both the front-end TEC Peltier device as well as satellite infrastructure had been damaged and no longer functioned. The front-end has been sent back to Stellenbosch University to investigate the fault. Despite this, in-field sky spectra was taken, a screenshot of which can be seen in fig. 2.47. As a disclosure, it should be noted that this in-field data was left on a USB flash drive on site and here, a snapshot from the KVM screen taken with a phone camera is used. The image has been enhanced using Microsoft Lens and the GNU Image Manipulation Program (GIMP). While the spectra shown in fig. 2.47 is raw, uncalibrated data that hasn't gone through any processing, some important details can be



Fig. 2.45 The REACH dipole antenna on the raised wire mesh ground plane. Support posts of heights varying 20 cm were raised to provide a level ground plane in contrast to the sloped land underneath.



Fig. 2.46 The receiver back-end and support enclosure underneath the solar panel installation at the deployment site.

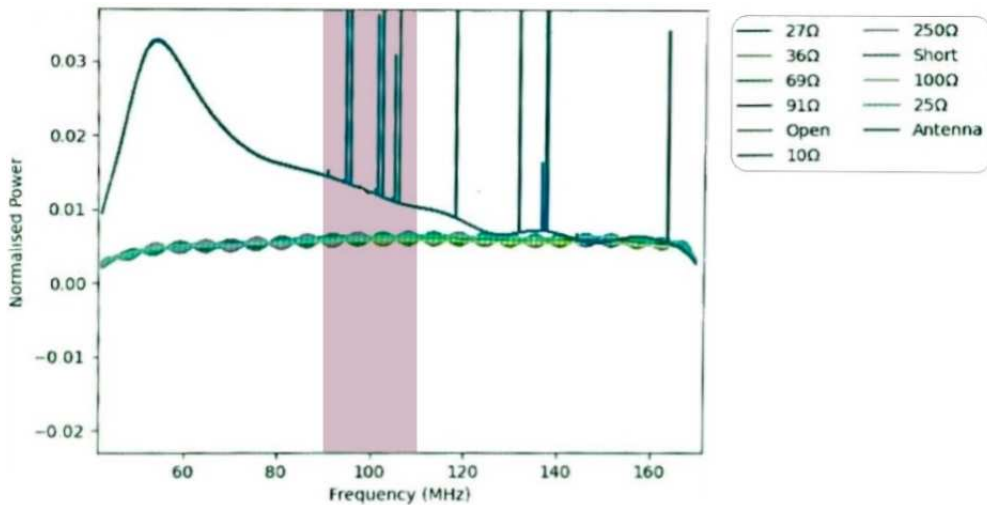


Fig. 2.47 A screenshot from the REACH's first light showing on-site sky data collected by the dipole and taken directly from the back-end KVM console using a mobile phone. The thermoelectric cooling unit damaged during transport was not running during this data acquisition. The spectra seen are uncalibrated and underwent no data processing which causes the spectra to deviate from the characteristic power-law form expected of the foregrounds at low and high frequencies. The shaded region is the FM radio broadcast band for South Africa (87.5 – 108 MHz).

derived from the plot. Firstly, spectra from the antenna is generally higher than the calibrator spectra which serves as a sanity check. Secondly, more than half of the RFI spikes seen in the antenna spectra lie within the FM radio broadcast band for South Africa (87.5 – 108 MHz) as highlighted in purple, confirming that our apparatus is indeed receiving radio-frequency signals. Further verification can be undertaken by cross checking the precise broadcast frequencies of local radio stations. Finally, we can also see that the antenna spectra peaks at low frequencies and decays off, approximating the power law shape of galactic synchrotron emission expected from sky measurements at these frequencies **COMPARE WITH POWER LAW SKY MEASUREMENT IN EDGES RESULT**. We therefore conclude that these spectra are encouraging as an initial proof-of-concept measurement.

Furthermore, it has also been seen that, due to the changing weather conditions on site, the 20×20 metre ground plane^o sags due to insufficient support. Provisional supports were made with scrap wood as seen in fig. 2.45 while a more permanent method of support is currently deployed. With the approximate completion of the ground plane, installation of the dipole antenna, solar panels and receiver back-end, the REACH site can be seen through satellite imaging at the latitude-longitude coordinates $30^{\circ}50'19.4''\text{S}$ $21^{\circ}22'29.8''\text{E}$ as shown in fig. 2.48.

^owith 6 metre serrations



Fig. 2.48 A satellite image from Google Earth showing the REACH deployment site. The 20 metre wide ground plane can be seen with the antenna installed at its centre. To the upper right of the ground plane is the back-end node covered by the solar panel installation. The lower left shows two vehicles and a tent with a dirt road exiting the site on the left along the ground plane.

Chapter 3

Receiver calibration

With a working instrument capable of taking measurements in the field, the next step towards detection of the 21-cm signature is calibration of the experimental apparatus. There are many forms of calibration from physical antenna or ground plane modifications to numerical post-processing methods such as correctional atmospheric modelling. The need for more accurate cosmic signal measurements against the cacophony of unwanted noise demands finer degrees of calibration through the development of novel methods. At the current technological aim of millikelvin-level calibration, minute differences in an instrument’s electrical properties can skew spectral measurements enough to hamper a cosmological detection. In the previous chapter, we detailed the system architecture designed to minimise these distortions. Here we present a procedure to calibrate out the remaining systematic effects. The task has encompassed decades of research starting in the 1950’s where Bauer and Rothe [6] and Rothe and Dahlke [59] introduced a wave formulation of noise to microwave systems^a before a mathematical prescription to eliminate these noise waves through the derivation of “noise wave parameters” was conceived by Meys [40] in 1978. This method, which inspires many contemporary radiometric calibration procedures, relies on the relative differences between sequential measurements of known passive devices to divide out small-timescale variability through a method known as “Dicke switching”, named after famed astronomer Robert Dicke. This relative calibration was utilised into the late 2000’s when Bowman and Rogers [13] placed a lower limit on the duration of the reionisation epoch at $\Delta z < 0.06$.

It was quickly understood that the extraction of further information from 21-cm experimentation required a more powerful calibration method and work commenced to reformulate the noise wave parameters under an “absolute” calibration procedure which offered a more comprehensive derivation by referencing all measurements to an absolute temperature scale as well as expanding compatibility with instruments of increasing bandwidth [58]. It was

^aBauer and Rothe [6] presented in English by Penfield [52].

this absolute calibration that was used in the 2018 EDGES measurement where the authors quote a 20 mK calibration accuracy [15, 43]. In response to the controversy surrounding the EDGES experiment, we have strived to improve the methodology and address discrepancies in the procedure through the introduction of a Bayesian calibration framework which we formulate over the following sections.

3.1 Calibration formalism

The noise necessitating calibration arises during measurements. For a global experiment such as REACH, we measure a sky temperature $T_{\text{sky}}(\Omega, v, t)$ as a function of the direction Ω , frequency v and time t which can be broken down into two primary components: the global 21-cm signal T_{21} and astrophysical foregrounds T_f

$$T_{\text{sky}}(\Omega, v, t) = T_{21}(v) + T_f(\Omega, v, t). \quad (3.1)$$

Sky signals absorbed by the antenna convolve with the normalised antenna directivity B , introducing systematic noise represented by our random noise term N_{data} .

$$D(v, t) = \int T_{\text{sky}}(\Omega, v, t)B(\Omega, v)d\Omega + N_{\text{data}}. \quad (3.2)$$

Thus, our 21-cm signature can be formulated as

$$T_{21} \approx D(v, t) - \int T_f(\Omega, v, t)B(\Omega, v)d\Omega - N_{\text{data}}. \quad (3.3)$$

A diagram illustrating the evolution of the sky signal during this process is shown in fig. 3.1. The integral in eq. (3.3) is assessed through foreground and beam modelling techniques such as those discussed in Anstey et al. [3] while modelling of N_{data} from the (statistical) properties of $D(v, t)$ is accomplished through calibration.

The standard calibration strategy follows the method introduced by Dicke to characterise systematic features in radio-frequency instruments [23] and is widely used in experiments such as EDGES [43] and LOFAR [8] to evaluate the spectral index of the sky's diffuse radio background [58]. The technique involves measurements of two internal reference standards; a load and a noise source, in addition to a series of external calibration sources attached to the receiver input in lieu of the antenna. Historically these include an ambient-temperature ‘cold’ load, a ‘hot’ load heated to ~ 400 K, an open-ended cable and a shorted cable as detailed previously in fig. 2.8.

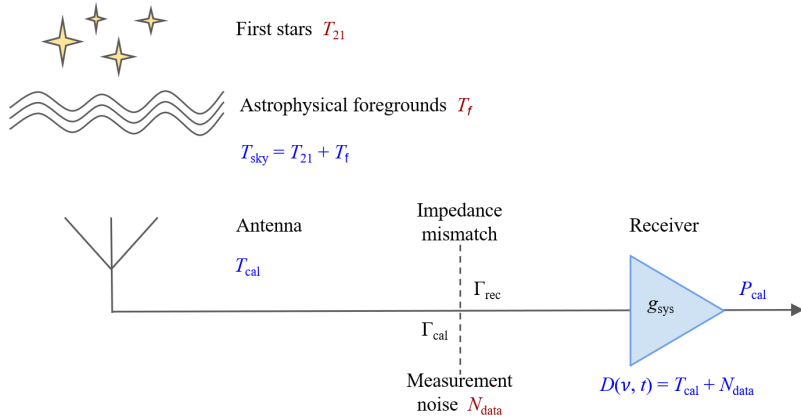


Fig. 3.1 Diagram showing the evolution of the 21-cm signal hampered by astrophysical foregrounds, convolution with the antenna beam and the emergence of measurement noise before calibration to retrieve the sky temperature.

During a calibration measurement, power spectral densities (PSDs) are taken of each Dicke switch position; the receiver input (P_{cal}), the internal reference load (P_L) and the internal reference noise source (P_{NS}) [43]. These measurements are used to calculate a preliminary ‘uncalibrated’ antenna temperature T_{cal}^*

$$T_{\text{cal}}^* = T_{\text{NS}} \left(\frac{P_{\text{cal}} - P_L}{P_{\text{NS}} - P_L} \right) + T_L, \quad (3.4)$$

where T_L and T_{NS} are assumptions for the noise temperature of the internal reference load and excess noise temperature of the internal noise source above ambient, respectively. This comparison of sequential power measurements serves as the ‘relative’ calibration which removes time-dependent variations in system gain emerging from individual components or technical capabilities of the instrument [43]. These PSD measurements can be expanded in terms of specific response contributions with the input power spectra being

$$P_{\text{cal}} = g_{\text{sys}} \left[T_{\text{cal}} (1 - |\Gamma_{\text{cal}}|^2) \left| \frac{\sqrt{1 - |\Gamma_{\text{rec}}|^2}}{1 - \Gamma_{\text{cal}} \Gamma_{\text{rec}}} \right|^2 + T_{\text{unc}} |\Gamma_{\text{cal}}|^2 \left| \frac{\sqrt{1 - |\Gamma_{\text{rec}}|^2}}{1 - \Gamma_{\text{cal}} \Gamma_{\text{rec}}} \right|^2 \right. \\ \left. + T_{\text{cos}} \operatorname{Re} \left(\Gamma_{\text{cal}} \frac{\sqrt{1 - |\Gamma_{\text{rec}}|^2}}{1 - \Gamma_{\text{cal}} \Gamma_{\text{rec}}} \right) + T_{\text{sin}} \operatorname{Im} \left(\Gamma_{\text{cal}} \frac{\sqrt{1 - |\Gamma_{\text{rec}}|^2}}{1 - \Gamma_{\text{cal}} \Gamma_{\text{rec}}} \right) + T_0 \right], \quad (3.5)$$

where Γ_{cal} and Γ_{rec} are the measured reflection coefficients of the device connected to the receiver input and receiver itself respectively. g_{sys} is the system gain referenced to the receiver input and T_{cal} is our calibrated input temperature. T_{unc} , T_{cos} , and T_{sin} are the ‘noise wave

parameters' introduced by Meys [40] to calibrate the instrument ^b. T_{unc} represents the portion of noise reflected by the antenna that is uncorrelated with the output noise of the LNA while T_{\cos} and T_{\sin} represent the portions correlated with LNA noise [43, 58]. The phase in which these reflected noise waves re-enter the receiver is described by the $\text{Re}()$ and $\text{Im}()$ arguments of eq. (3.5)^c. In the EDGES experiment, the noise wave parameter quantities are modelled using seven-term polynomials in frequency.

The PSDs for the internal reference load and noise source can similarly be expressed as in eq. (3.5). However, since the reflection coefficients of the internal references are assumed to be small, we approximate them as zeros in order to simplify the equations

$$P_L = g_{\text{sys}}^* [T_L (1 - |\Gamma_{\text{rec}}|^2) + T_0^*], \quad (3.6)$$

$$P_{\text{NS}} = g_{\text{sys}}^* [(T_L + T_{\text{NS}}) (1 - |\Gamma_{\text{rec}}|^2) + T_0^*]. \quad (3.7)$$

As shown in fig. 2.8, the internal references may be on a separate reference plane than the receiver input, resulting in a system gain g_{sys}^* and a noise offset T_0^* different from those defined in eq. (3.5). This effect is taken into account by two additional scale and offset parameters, C_1 and C_2 , introduced by EDGES [43].

Since C_1 and C_2 also correct for first-order assumptions in the noise temperatures of the internal reference load and noise source, we have chosen to absorb these terms into T_L and T_{NS} in our analysis. This adjustment allows all calibration parameters, T_{unc} , T_{\cos} , T_{\sin} , and the 'effective' T_{NS} and T_L , to be solved for in units of kelvin, facilitating a joint solution of parameters. Expanding eq. (3.4) using eqs. (3.5) to (3.7) yields a linear identity providing a relationship between the uncalibrated input temperature and a final calibrated temperature of any device connected to the receiver input

$$\begin{aligned} T_{\text{NS}} \left(\frac{P_{\text{cal}} - P_L}{P_{\text{NS}} - P_L} \right) + T_L &= T_{\text{cal}} \left[\frac{1 - |\Gamma_{\text{cal}}|^2}{|1 - \Gamma_{\text{cal}}\Gamma_{\text{rec}}|^2} \right] + T_{\text{unc}} \left[\frac{|\Gamma_{\text{cal}}|^2}{|1 - \Gamma_{\text{cal}}\Gamma_{\text{rec}}|^2} \right] \\ &\quad + T_{\cos} \left[\frac{\text{Re} \left(\frac{\Gamma_{\text{cal}}}{1 - \Gamma_{\text{cal}}\Gamma_{\text{rec}}} \right)}{\sqrt{1 - |\Gamma_{\text{rec}}|^2}} \right] + T_{\sin} \left[\frac{\text{Im} \left(\frac{\Gamma_{\text{cal}}}{1 - \Gamma_{\text{cal}}\Gamma_{\text{rec}}} \right)}{\sqrt{1 - |\Gamma_{\text{rec}}|^2}} \right], \end{aligned} \quad (3.8)$$

where all parameters are frequency-dependent though not explicitly shown for simplicity of notation. During a calibration procedure, T_{cal} , Γ_{cal} and Γ_{rec} are measured along with the PSDs while g_{sys} and T_0 are calibrated out via the 'relative' calibration procedure inherent to

^bequivalent to T_a , T_b , and T_c in his notation

^cThese arguments are equivalent to the α term in the EDGES notation [43] and analogous to ϕ in the Meys formulation [40]

eq. (3.4). As stated in section 2.1.1, the 50Ω cold and hot loads exhibit the main temperature references needed for T_L and T_{NS} while delayed reflection in the calibration cables allow for the derivation of T_{unc} , T_{cos} and T_{sin} by simulating an antenna observing an ambient temperature sky [58].

3.2 Bayesian parameter derivation

From an instrumentation perspective, a possible source of the systematics thought to blemish the EDGES measurement is the calibration of their instrument in a controlled laboratory setting separate from the environment in which astrophysical observations take place. At the milli-kelvin level, these environmental effects may be non trivial. Parameters related to the physical instrument are expected to change such as the antenna response due to heat expansion or impedance fluctuations of delicate front-end components. As corroborated by the various experiments in the REFER TO RESULTS SECTION, this may especially be the case with regards to how the calibration parameters change between observation runs. Furthermore, the fixed seven-term polynomial used by EDGES to model all of their noise wave parameters may underfit or overfit individual parameters and thus ‘fit out’ data useful for determining systematics or potentially even the 21-cm signal itself if a joint fit is performed.

In response to these concerns, we have developed a calibration pipeline that improves on the strategies presented in Monsalve et al. [43] and introduce a novel Bayesian methodology using conjugate priors, allowing for a dynamic application of our algorithm in the field with astrophysical data collection regardless of system complexity. Also included are model selection procedures for the optimisation of individual noise wave parameters to combat overfitting and underfitting, the results of which converge with that of a least-squares approach when wide priors are adopted. Our pipeline easily incorporates many more calibration sources than the standard four as shown in section 2.1.1 for increased constraints on noise wave parameters while identifying possible correlations between parameters. A schematic overview of our improved Bayesian calibration method is shown in fig. 3.2.

We first, simplify the notation of our approach by defining the following terms

$$X_{unc} = -\frac{|\Gamma_{cal}|^2}{1 - |\Gamma_{cal}|^2}, \quad (3.9)$$

$$X_L = \frac{|1 - \Gamma_{cal}\Gamma_{rec}|^2}{1 - |\Gamma_{cal}|^2}, \quad (3.10)$$

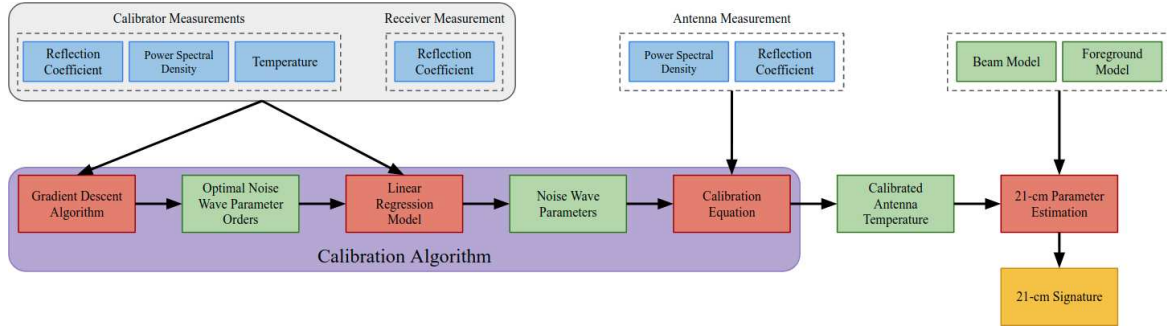


Fig. 3.2 Outline of our Bayesian calibration algorithm. Blue blocks represent data to be taken, red blocks represent calculations and green blocks represent calculation outputs.

$$X_{\cos} = -\operatorname{Re} \left(\frac{\Gamma_{\text{cal}}}{1 - \Gamma_{\text{cal}}\Gamma_{\text{rec}}} \times \frac{X_L}{\sqrt{1 - |\Gamma_{\text{rec}}|^2}} \right), \quad (3.11)$$

$$X_{\sin} = -\operatorname{Im} \left(\frac{\Gamma_{\text{cal}}}{1 - \Gamma_{\text{cal}}\Gamma_{\text{rec}}} \times \frac{X_L}{\sqrt{1 - |\Gamma_{\text{rec}}|^2}} \right), \quad (3.12)$$

$$X_{\text{NS}} = \left(\frac{P_{\text{cal}} - P_L}{P_{\text{NS}} - P_L} \right) X_L, \quad (3.13)$$

which represent initial calibration measurements on D in the frequency domain for the characterisation of N_{data} from eq. (3.2) via our noise wave parameters. Here we assume that calibration-related deviations of D in the time domain are sufficiently curtailed through practical strategies such as temperature control of the receiver environment. Incorporating these equations into eq. (3.8), with some rearrangement, then gives

$$X_{\text{unc}} T_{\text{unc}} + X_{\cos} T_{\cos} + X_{\sin} T_{\sin} + X_{\text{NS}} T_{\text{NS}} + X_L T_L = T_{\text{cal}}, \quad (3.14)$$

at each frequency. We can see here that there are no squared or higher-order terms, allowing us to take advantage of the linear form by grouping the data and noise wave parameters into separate matrices

$$\begin{aligned} \mathbf{X} &\equiv \begin{pmatrix} X_{\text{unc}} & X_{\cos} & X_{\sin} & X_{\text{NS}} & X_L \end{pmatrix}, \\ \boldsymbol{\Theta} &\equiv \begin{pmatrix} T_{\text{unc}} & T_{\cos} & T_{\sin} & T_{\text{NS}} & T_L \end{pmatrix}^{\top}. \end{aligned} \quad (3.15)$$

Under this formulation, all of our data; the reflection coefficient measurements and power spectral densities, are grouped in an \mathbf{X} vector which forms a matrix where one of the axes is frequency. The calibration parameters as frequency-dependent polynomials of varying degree are collected into a $\boldsymbol{\Theta}$ vector which serves as our model describing N_{data} . Applying

these definitions condenses the calibration equation into

$$\mathbf{T}_{\text{cal}} = \mathbf{X}\Theta + \sigma, \quad (3.16)$$

where \mathbf{T}_{cal} is a vector over frequency and σ is a noise vector representing our error. Since EDGES assumes that each power spectral density measurement is frequency independent, we have assumed that σ is a multivariate normal distribution. This assumption is implicit in the EDGES analysis in which they use a least-squares minimisation approach for solving model parameters.

For calibration of the receiver, we are concerned with the construction of predictive models of the noise wave parameters, Θ , in the context of some dataset, \mathbf{T} . We can use Θ to calculate the probability of observing the data given a specific set of noise wave parameters:

$$p(\mathbf{T} | \Theta, \sigma^2) = \frac{1}{2\pi\sigma^2}^{N/2} \exp \left\{ -\frac{1}{2\sigma^2} (\mathbf{T} - \mathbf{X}\Theta)^\top (\mathbf{T} - \mathbf{X}\Theta) \right\}, \quad (3.17)$$

where, N is the number of measurements. This distribution on the data is the *likelihood*. For the purposes of calibration, \mathbf{T} may be \mathbf{T}_{cal} measurements or alternatively, \mathbf{T}_{sky} for prediction of a sky signal. Our model must also specify a *prior* distribution, quantifying our initial assumptions on the values and spread of our noise wave parameters which we specify as a multivariate normal inverse gamma distribution:

$$p(\Theta, \sigma^2) \propto \left(\frac{1}{\sigma^2} \right)^{a+1+(d/2)} \times \exp \left[-\frac{1}{\sigma^2} \left\{ b + \frac{1}{2} (\Theta - \mu_\Theta)^\top \mathbf{V}_\Theta^{-1} (\Theta - \mu_\Theta) \right\} \right], \quad (3.18)$$

which is proportional up to an integration constant. Here, a and b , which are greater than zero, along with \mathbf{V}_Θ and μ_Θ represent our prior knowledge on the noise wave parameters. d is the length of our vector Θ .

Equation (3.17) is determined by a set of values for our model Θ . We can marginalise out the dependence on Θ and our noise term by integrating over the prior distribution by both Θ and σ^2 at once. Following the steps in Banerjee [5]

$$\begin{aligned} p(\mathbf{T}_{\text{cal}}) &= \int p(\mathbf{T}_{\text{cal}} | \Theta, \sigma^2) p(\Theta, \sigma^2) d\Theta d\sigma^2 \\ &= \frac{b^a \Gamma(a^*) \sqrt{|\mathbf{V}^*|}}{b^{*a^*} \Gamma(a) \sqrt{|\mathbf{V}_\Theta|}} (2\pi)^{-N/2}, \end{aligned} \quad (3.19)$$

where

$$\begin{aligned} a^* &= a + \frac{N}{2}, \\ b^* &= b + \frac{1}{2} [\boldsymbol{\mu}_{\Theta}^{\top} \mathbf{V}_{\Theta}^{-1} \boldsymbol{\mu}_{\Theta} + \mathbf{T}_{\text{cal}}^{\top} \mathbf{T}_{\text{cal}} - \boldsymbol{\mu}^{*\top} \mathbf{V}^{*-1} \boldsymbol{\mu}^*], \\ \boldsymbol{\mu}^* &= (\mathbf{V}_{\Theta}^{-1} + \mathbf{X}^{\top} \mathbf{X})^{-1} (\mathbf{V}_{\Theta}^{-1} \boldsymbol{\mu}_{\Theta} + \mathbf{X}^{\top} \mathbf{T}_{\text{cal}}), \\ \mathbf{V}^* &= (\mathbf{V}_{\Theta}^{-1} + \mathbf{X}^{\top} \mathbf{X})^{-1}, \end{aligned} \quad (3.20)$$

and $\Gamma(x)$ represents the Gamma function, not to be confused with the notation for our reflection coefficients. Equation (3.19) is the *evidence*, which gives the probability of observing the data \mathbf{T}_{cal} given our model.^d

With the prior distribution specified, we use Bayes' equation to invert the conditioning of the likelihood and find the *posterior* using the likelihood, prior and evidence:

$$p(\boldsymbol{\Theta}, \sigma^2 | \mathbf{T}_{\text{cal}}) = \frac{p(\mathbf{T}_{\text{cal}} | \boldsymbol{\Theta}, \sigma^2) p(\boldsymbol{\Theta}, \sigma^2)}{p(\mathbf{T}_{\text{cal}})}. \quad (3.21)$$

Similarly from Banerjee [5], this can be written as

$$p(\boldsymbol{\Theta}, \sigma^2 | \mathbf{T}_{\text{cal}}) \propto \left(\frac{1}{\sigma^2} \right)^{a^* + \frac{d}{2} + 1} \times \exp \left\{ -\frac{1}{\sigma^2} \left[b^* + \frac{1}{2} (\boldsymbol{\Theta} - \boldsymbol{\mu}^*)^{\top} \mathbf{V}^{*-1} (\boldsymbol{\Theta} - \boldsymbol{\mu}^*) \right] \right\}. \quad (3.22)$$

The posterior distribution represents the uncertainty of our parameters after analysis, reflecting the increase in information [46]. We highlight the difference between the ‘likelihood-only’ least-squares approach versus the Bayesian approach with the former being a special case of the latter with very wide priors demonstrable when $\mathbf{V}_{\Theta} \rightarrow \infty \Rightarrow \mathbf{V}_{\Theta}^{-1} \rightarrow 0$, and $\boldsymbol{\mu}^*$ becomes $\boldsymbol{\Theta}$. The transition from ‘non-starred’ variables to ‘starred’ variables represents our ‘Bayesian update’ of the prior to the posterior noise wave parameters in light of the calibration data \mathbf{T}_{cal} .

As we can see, the posterior distribution is in the same probability distribution family as eq. (3.18), making our prior a *conjugate prior* on the likelihood distribution. The use of conjugate priors gives a closed-form solution for the posterior distribution through updates of the prior hyperparameters via the likelihood function [5, 49]. The resulting numerical computation is many orders of magnitude faster than MCMC methods relying on full numerical sampling and permits an in-place calculation in the same environment as the data acquisition. This becomes particularly useful for the speed of the algorithm as frequency

^dIt is in fact better to use the equivalent more numerically stable expression $b^* = b + \mathbf{q}^{\top} \mathbf{q} + \mathbf{q}^{\top} \mathbf{X} \mathbf{V}_{\Theta} \mathbf{X}^{\top} \mathbf{q}$, where $\mathbf{q} = \mathbf{T}_{\text{cal}} - \mathbf{X} \boldsymbol{\mu}^*$ to avoid cancellation of large terms.

dependence is introduced in which the computations would not be manageable without conjugate gradients.

To allow for a smooth frequency dependency, we promote each of our noise wave parameters in eq. (3.15) to a vector of polynomial coefficients

$$T_i = \left(T_i^{[0]}, \quad T_i^{[1]}, \quad T_i^{[2]}, \quad \dots, \quad T_i^{[n]} \right), \quad (3.23)$$

where i is our noise wave parameter label; $i \in \{\text{unc}, \cos, \sin, \text{NS}, \text{L}\}$, modelled using $n + 1$ polynomial coefficients. Likewise

$$\mathbf{X}_i = \left(\mathbf{x}_i, \quad \mathbf{x}_i \left(\frac{v}{v_0} \right), \quad \mathbf{x}_i \left(\frac{v}{v_0} \right)^2, \quad \dots, \quad \mathbf{x}_i \left(\frac{v}{v_0} \right)^n \right), \quad (3.24)$$

where v is a vector of input frequencies which are raised to powers up to n . For a vector of n 's attributed to our calibration parameters, under this notation multiplication in eq. (3.16) is element-wise and eq. (3.19) is effectively $p(\mathbf{T}_{\text{cal}}|\mathbf{n})$. Assuming a uniform prior on \mathbf{n} , inverting Bayes' theorem gives $p(\mathbf{n}|\mathbf{T}_{\text{cal}})$ for use in model comparison in which the relative probabilities of models can be evaluated in light of the data and priors. Occam's razor advises whether the extra complexity of a model is needed to describe the data [67], permitting optimisation of the polynomial orders for individual noise wave parameters as detailed in section 3.1. By taking a random sampling of the resulting posterior, we characterise the noise wave parameters as multivariate distributions depicted in contour plots which exhibit a peak value accompanied by 1σ and 2σ variance as well as correlation between parameters inferred from a covariance matrix.

Following characterisation of the receiver, we next apply the \mathbf{T}_{cal} from our calibration to a set of raw antenna data $\hat{\mathbf{X}}$ for prediction of our sky signal, \mathbf{T}_{sky} , from eq. (3.2). The predictions for the data follow from the *posterior predictive distribution*

$$p(\mathbf{T}_{\text{sky}} | \mathbf{T}_{\text{cal}}) = \int p(\mathbf{T}_{\text{sky}} | \Theta, \sigma^2) p(\Theta, \sigma^2 | \mathbf{T}_{\text{cal}}) d\Theta d\sigma^2. \quad (3.25)$$

The first probability in the integral is the likelihood for our antenna measurement \mathbf{T}_{sky} and the second is our posterior from eq. (3.22). Following the steps in Banerjee [5], this can be

shown to be a multivariate Student's t-distribution written as:

$$p(\mathbf{T}_{\text{sky}} | \mathbf{T}_{\text{cal}}) = \frac{\Gamma(a^* + \frac{d}{2})}{\Gamma(a^*) \pi^{\frac{d}{2}} |2b^* (I + \hat{\mathbf{X}}\mathbf{V}^*\hat{\mathbf{X}}^\top)^{-1}|^{\frac{1}{2}}} \\ \times \left[1 + \frac{(\mathbf{T}_{\text{sky}} - \hat{\mathbf{X}}\boldsymbol{\mu}^*)^\top (I + \hat{\mathbf{X}}\mathbf{V}^*\hat{\mathbf{X}}^\top)^{-1} (\mathbf{T}_{\text{sky}} - \hat{\mathbf{X}}\boldsymbol{\mu}^*)}{2b^*} \right]^{-(a^* + \frac{d}{2})}, \quad (3.26)$$

where I is the $N \times N$ identity matrix and a^* , b^* , $\boldsymbol{\mu}^*$ and \mathbf{V}^* are defined in eq. (3.20). This new distribution on \mathbf{T}_{sky} corresponds to a set of points with error bars and represents the calibrated sky temperature as the output of the receiver.

Chapter 4

Results

Hold on. This whole operation was your idea.

Anakin Skywalker

Now that we are caught up with the technical logistics of the instrument as well as the mathematical prescription to calibrate it, we assess the capabilities of our method under the scrutiny of varied sets of data. Throughout the process of our research, practical development of the receiver reformed our approach to calibration which consequently reshaped the implementation of our instrument design. In the continuous interchange of physical and mathematical adjustments, a great deal of experiments were undertaken to increase the potency of our algorithm, often to little or no effect. The results presented here demonstrate the incremental progress in calibration accuracy up to the time of deployment in the Fall of 2023. We start by briefly detailing the application of data taken before construction of the REACH receiver as a proof-of-concept that reasonable calibrated temperatures can be retrieved. Following this, we give results from the application of simulated data to assess the noise floor of our algorithm under idealised conditions. We then exhibit the capabilities of our algorithm using laboratory data taken from a partially-constructed REACH receiver as well as a HERA receiver to demonstrate the further application of the procedure to other experiments. Results from data collected with a completed REACH receiver are shown along with an overview of attempts to increase the effectiveness of our technique through physical and computational adjustments. We then compare our results to the conventional formulation as a sanity check before discussing efforts with more advanced methods after which we appraise the state of the field considering these developments.

4.1 Preliminary laboratory measurements

Whilst construction of the receiver was underway, preliminary experiments were performed to gauge the performance of our calibration procedure. An initial dataset was produced using some of the publicly available EDGES data and laboratory measurements taken at Cambridge using various disconnected instruments. Two calibration sources were used for our measurements; a 50Ω load at ambient temperature and a heated source constructed from a 50Ω load coupled to a ThermOptics DN511 proportional heater set to 373 K and attached to a 4-inch rigid coaxial cable similar to the apparatus detailed in section 2.1.1. Temperatures for these calibration sources were assumed to be 298 K and 373 K respectively and were not measured during the experiment.

As the receiver was not yet built, a Dicke switch was approximated by manually swapping sources at the front of the signal chain. An additional 50Ω load was used as the reference load while a Noisecom NC346A noise diode with 5 dB of attenuation was used as the reference noise source. The Noisecom NC346A was chosen for its stable noise output value of ~ 350 K over the frequency band of interest as shown in TABLE and resembling the specifications of the internal reference noise source used by the EDGES team. Reflection data for the devices was taken using the Keysight N5247A PNA-X VNA. An RF signal chain was created for PSD measurements which consisted of 10 metres of coaxial cabling preceding a custom built LNA with specifications shown in table A.7. Following the LNA, the signal was filtered before reaching a CASPER ROACH-2 ADC/spectrometer made from an AMD XILINX Virtex-6 FPGA.

Combining our measurements of the ambient and heated loads along with the noise wave parameters published by EDGES (T_{unc} , T_{\cos} , T_{\sin} , C_1 and C_2), a system of calibration equations was established in which the noise temperatures for the internal reference load and noise source were calculated under their model and plotted in fig. 4.1 as the red and dark blue data respectively. Returning to our formulation as specified in section 3.1 MAKE SURE REFER TO OUR FORMALISM NOT EDGES, measured reflection coefficients, PSDs and the assumed temperatures were inputted into our model to solve for the noise wave parameters. 1000 posterior samples of T_{NS} and T_L ^a from our Bayesian model are plotted in fig. 4.1 in orange and cyan respectively.

The apparent agreement between the system solution and our Bayesian model supports our assertion that the absorption of the EDGES C_1 and C_2 parameters into an effective T_{NS} and T_L is a valid procedure. Furthermore, recovery of the internal reference noise temperatures assumed by EDGES, 350 K and 300 K for the internal noise source and load respectively,

^anow proper noise wave parameters in this formulation

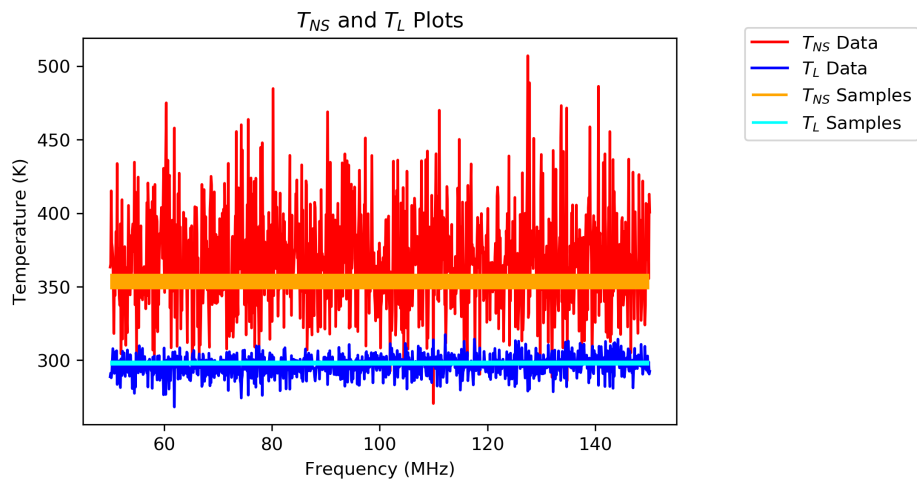


Fig. 4.1 Calculations of T_{NS} and T_{L} from initial datasets taken before construction of the REACH receiver. Two-minute integrations and reflection coefficient data were taken of the ambient and heated 50Ω loads. The red and dark blue show the resulting T_{NS} and T_{L} from solving a linear set of calibration equations under the EDGES formulation for calibratin a receiver. The orange and cyan show 1000 posterior samples for T_{NS} and T_{L} from our Bayesian algorithm. The agreement between the system-of-equations and Bayesian solutions indicates the validity of our changes to the formulation. Recovery of the assumed noise temperatures of the internal reference noise source and load (350 K and 300 K respectively) shows that noise wave parameter values may be determined under our Bayesian algorithm. Finally, the reduction of noise apparent in the Bayesian solution is encouraging suggests that the method improves calibration accuracy.

Calibrator	Temperature
Cold load (50Ω)	298 K
Hot load (50Ω)	373 K
Gore cable +5 Ω	298 K
Gore cable +500 Ω	298 K
Gore cable +31 Ω	298 K
Gore cable +81 Ω	298 K
25 Ω resistor	298 K
100 Ω resistor	298 K

Table 4.1 Table of calibrators used in the creation of our empirical data models for analysis. Calibrators were inputted in pairs in the order shown when demonstrating the effects of additional calibrator information (see REFER TO SECTION ON INCREASING CALIBRATOR NUMBER).

shows that our model can correctly determine the T_{NS} and T_L parameters using ambient and heated source data. Additionally, the reduction of noise in the Bayesian solution suggests that our method improves calibration accuracy when subjected to identical data.

4.2 Results with simulated data

To verify the performance of our pipeline and highlight features of the algorithm, we evaluate the results of self-consistency checks using empirical models of data based on measurements taken in the laboratory. To make this data as realistic as possible, we used actual measurements of the reflection coefficients of many types of calibrators (see table 4.1) to generate power spectral densities using eqs. (3.5) to (3.7) given a set of realistic model noise wave parameters along with some assumptions about the noise, which are described in REFER TO THE SECTION WHERE WE DESCRIBE ADDING NOISE TO THE SIMULATED CALIBRATORS. The impedance of the calibrators which were measured with a vector network analyser (VNA) and used in our pipeline are shown on a Smith chart in fig. 4.2

We start by demonstrating the importance of correlation between noise wave parameters when determining their values to provide a better calibration solution (section 4.2.1). We then show the increased constraints on these noise wave parameters attributed to the inclusion of more calibrators than the standard number of four (REFER TO SECTION). Following this, we illustrate the effectiveness of model selection for the optimisation of individual noise wave parameters to prevent the loss of information resulting from overfitting or underfitting

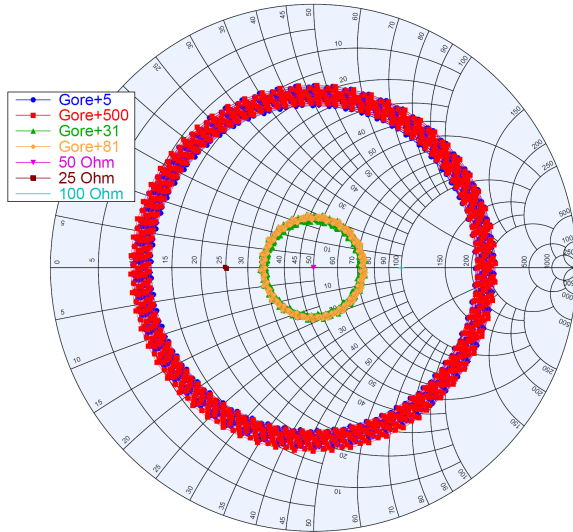


Fig. 4.2 Smith chart showing the measured complex impedance of devices used to create empirical models of calibration sources for testing of our Bayesian algorithm.

of the data (REFER TO SECTION). Finally, these features are incorporated into a calibration solution applied to a $50\ \Omega$ load (REFER TO SECTION).

4.2.1 Correlation between noise wave parameters

The first major feature of our Bayesian pipeline is the consideration of possible correlation between noise wave parameters when deriving their values. This is best demonstrated when noise is introduced in an idealised way as to retain a form matching the Gaussian form of our mathematical model. To do this, empirical models of power spectral densities are calculated from eqs. (3.5) to (3.7) using measurements of Γ_{rec} , Γ_{cal} and T_{cal} for the cold and hot loads, as well as a set of realistic fiducial noise wave parameters. Gaussian noise of one unit variation is then added to the T_{cal} measurements after the calculation to conserve its Gaussian form. This data is submitted to our algorithm and the resulting posterior distributions for coefficients of the polynomial noise wave parameters are compared to the fiducial values.

Such posterior distributions can be seen in fig. 4.3 showing the results of models using only the cold load (grey posterior), only the hot load (red posterior) and using both loads in tandem (blue posterior). For these calculations we chose a set of model noise wave

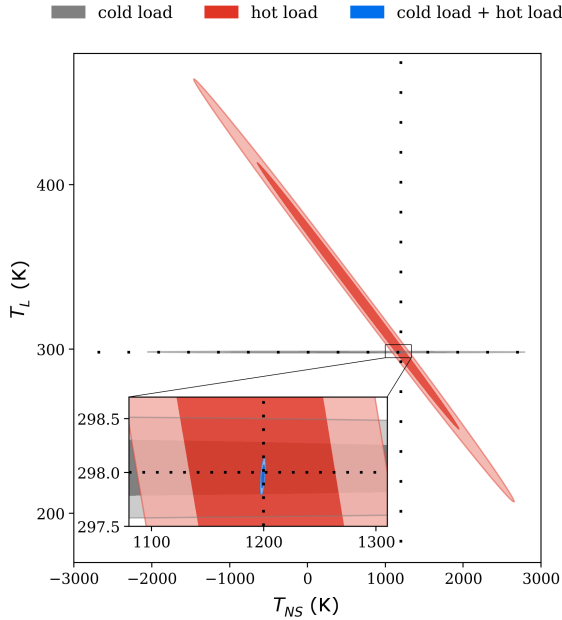


Fig. 4.3 Plot showing the joint posteriors of T_L and T_{NS} for models using the cold load, the hot load, and both loads concurrently shown as the grey, red and blue posteriors respectively. The black cross hairs mark the noise wave parameter values used to generate data submitted to the pipeline. A zoom-in of the posterior intersection is provided to illustrate the constraint of noise wave parameter values attributed to the correlation between parameters.

parameters as constants across the frequency band;

$$T_{unc} = 250 \text{ K}$$

$$T_{cos} = 190 \text{ K}$$

$$T_{sin} = 90 \text{ K}$$

$$T_{NS} = 1200 \text{ K}$$

$$T_L = 298 \text{ K}$$

In fig. 4.3, a strong correlation between the T_L and T_{NS} is evident as the hot-load posterior is highly skewed as expected from eqs. (3.10) and (3.13). The resulting intersection of posteriors from the individual loads facilitate the derivation of noise wave parameters as the dual-load posterior is found within the region of posterior overlap crossing with the values of the model shown in the inset of fig. 4.3. Retrieval of the noise wave parameter values using correlations between them found in the data demonstrate the relevance of this information which is not taken into account in previous calibration techniques.

4.2.2 Constraints with additional calibrators

Another feature of our pipeline is the ability to include as many calibrators as required to constrain the calibration parameters. For analysis, six more calibrators are introduced in pairs following the order presented in table 4.1. We include data generated from measurements of multiple resistors terminating a high quality 25 m cable made by GORE[®]^b. Data for these calibrators is once again generated using fixed terms and Gaussian noise of one unit variation added to T_{cal} as discussed above. Figure 4.4 shows the results of models using four, six, and eight calibrators.

As shown, the inclusion of more calibrators increases the constraint on the resulting noise wave parameters. However, we note that after the inclusion of four calibrators, the relative additional constraint decreases with each additional calibrator and thus the use of a large number of calibrators would be unnecessary. The values of noise wave parameters used to generate the data as indicated by the cross hairs in fig. 4.4 all fall within 1σ of our pipeline’s resulting posterior averages for models using all eight calibrators.

4.2.3 Optimisation of individual noise wave parameters

The final highlight of our Bayesian pipeline is a use of machine learning techniques to optimise individual noise wave parameters. This is advantageous as a blanket prescription of order-seven polynomials applied to all noise wave parameters, such as done in the EDGES experiment, may underfit or overfit individual parameters and misidentify systematics or information about the signal being measured.

The optimisation procedure compares the evidences (eq. (3.19)) of different models to determine the vector of noise wave parameter polynomial coefficients \mathbf{n} that best describes the data as briefly mentioned at the end of section 3.2. Since the model favoured by the data will have the highest evidence, we use a steepest descent procedure to compare models in ‘ \mathbf{n} -space’ and determine the direction of the gradient in ‘evidence-space’. After multiple iterations, this brings us to the model with the maximal evidence. Since \mathbf{n} consists of five numbers corresponding to the number of polynomial coefficients for each of the five noise wave parameters, models are generated by individually increasing each index of \mathbf{n} by 1. We expect the evidence to follow an ‘Occam’s cliff,’ in which the evidence sharply increases preceding the optimal \mathbf{n} with a slow fall-off following the maximum.

^bAt this stage of development, we had not decided on which model of cable would optimise both calibration results and cost efficiency. While we eventually chose the LMC195 cabling detailed in section 2.1.1, many early datasets included the high quality, but expensive GORE[®] cabling.

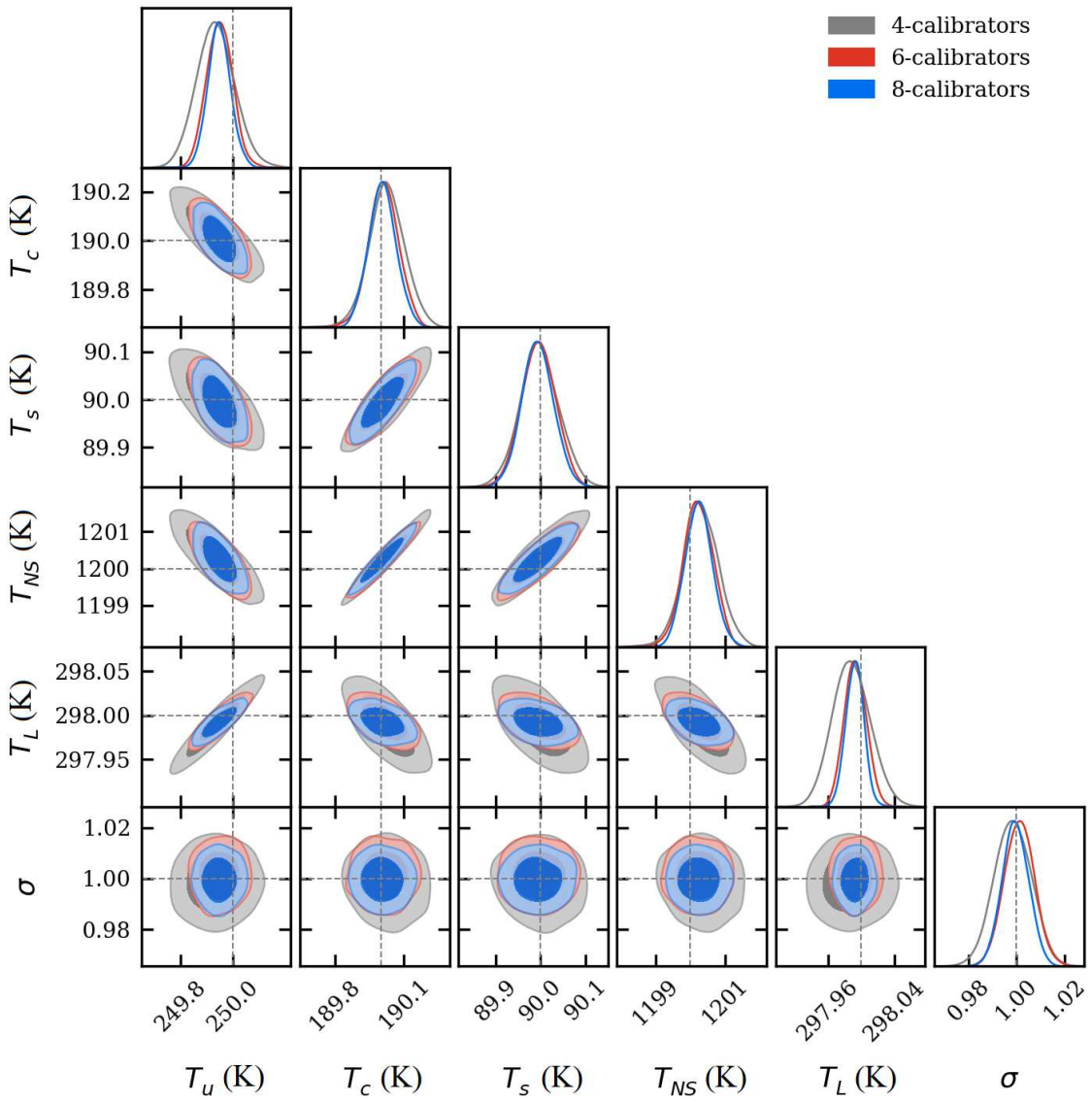


Fig. 4.4 Posterior results of our pipeline using data from four, six and eight calibrators shown in grey, red and blue, respectively. Cross hairs mark the values of noise wave parameters used to generate the data. These values fall within 1σ of the posterior mean values. We can see that the constraint on noise wave parameter values increases with the number of calibrators used in our pipeline which is encouraging.

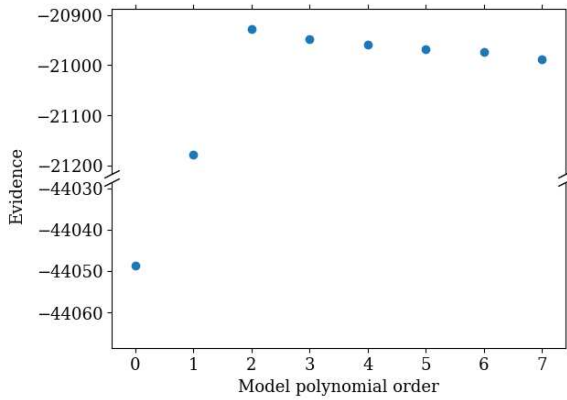


Fig. 4.5 Evidence of multiple models are plotted which display the Occam’s cliff. Data is generated using noise wave parameters as order-2 polynomials. We see that for the model with the highest evidence, that is, the model favoured by the data, the number of polynomial coefficients matches that of the model noise wave parameters.

To demonstrate this, data is generated using measurements from all eight calibrators of table 4.1 and noise wave parameters as second-order polynomials

$$\begin{aligned}
 T_{\text{unc}} &= x^2 - 3x + 250 \text{ K} \\
 T_{\text{cos}} &= 2x^2 + 190 \text{ K} \\
 T_{\text{sin}} &= 3x^2 + 8x + 90 \text{ K} \\
 T_{\text{NS}} &= 4x^2 + 5x + 1200 \text{ K} \\
 T_{\text{L}} &= 5x^2 + 10x + 298 \text{ K}
 \end{aligned}$$

where x is our normalised frequency. Gaussian noise of one unit variation is applied to the calibrator input temperatures as before. The evidences of various models are plotted in fig. 4.5 in which an Occam’s cliff can be seen peaking at polynomial order two. As expected from the plot, the steepest descent algorithm finds that noise wave parameters modelled as second-order polynomials best describe the data.

4.2.4 Application with realistic noise

To demonstrate the robustness of our pipeline, we conducted self-consistency checks using empirically modelled data with a more complicated noise model. This data was generated using reflection coefficients of eight calibrators and the receiver measured in the laboratory. These reflection coefficients were then smoothed using a cubic smoothing spline [71] in order to maintain their approximate shape over frequency. The same second-order noise

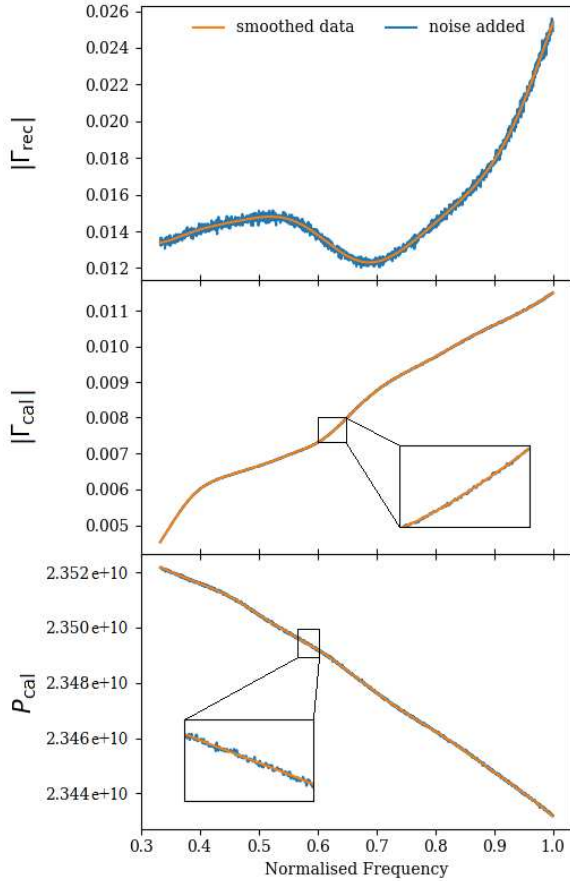


Fig. 4.6 Power spectral densities and reflection coefficients for the receiver and the cold load generated under our realistic noise model.

wave parameters detailed in section 4.2.3 are used with the reflection coefficients to generate our model power spectral densities. Following this, we added of order 1% Gaussian noise independently to the smoothed Γ_{rec} and Γ_{cal} as well as P_{cal} to more accurately represent the instrument noise from measurement equipment such as vector network analysers. No noise was added to the calibrator input temperatures. This results in a model that does not match the Gaussian form of our mathematical model as in the previous sections and thus does not demonstrate the features of our pipeline as explicitly, but is more representative of data set expected from measurements in the field. Data for the receiver and the cold load generated using this noise model are shown in fig. 4.6.

Using data generated for all eight calibrators with our realistic noise model, the calibration algorithm selects optimal polynomial orders matching those of the model noise wave parameters whose values fall within within 1σ of the posterior peak values as shown in fig. 4.7. For these higher order tests, we use fgivenx plots which condense noise wave

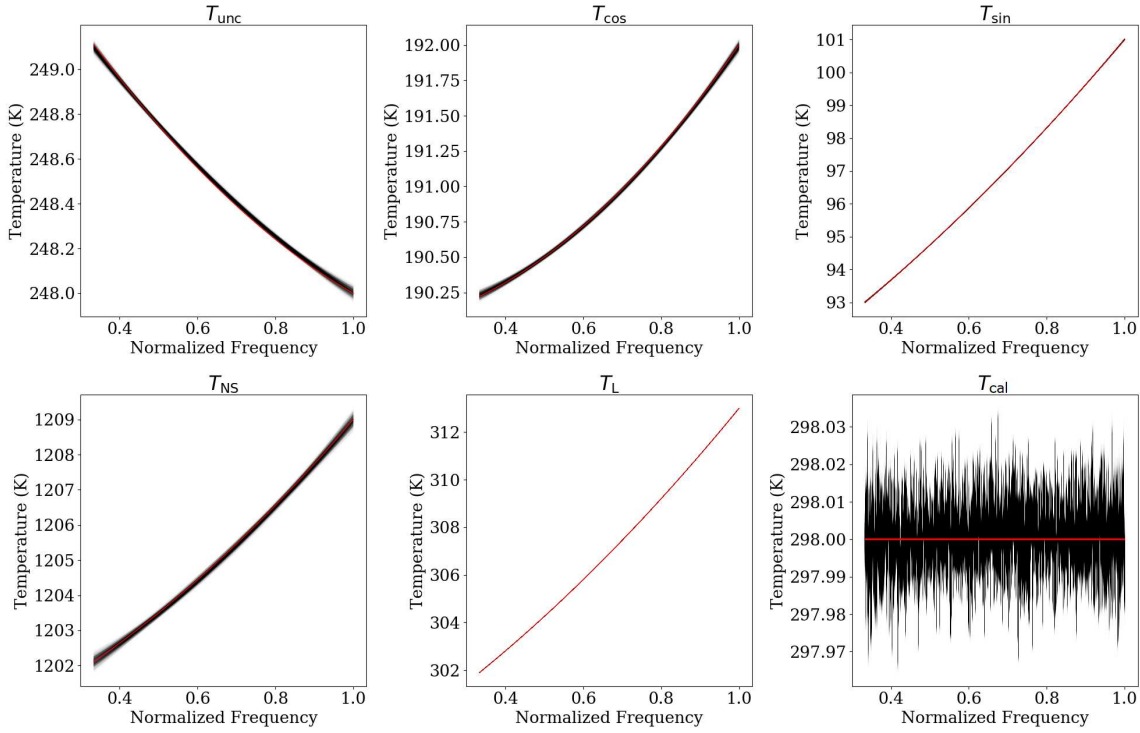


Fig. 4.7 Results from 1000 samples using data generated with our more realistic noise model (shown in black). The second-order noise wave parameters shown in red are used to generate the data inputted to our pipeline. The polynomial order and values of the noise wave parameters that best suit the data according to our algorithm match that of the empirical model. This solution is applied to an ambient-temperature load, shown in the bottom right panel as our predictive \hat{y} from eq. (3.26), and calibrates it to within 1σ of ambient temperature.

parameter posteriors into samples that can be compared to the model parameter values instead of comparing each individual coefficient [29].

When this calibration model is used to calibrate an ambient-temperature 50Ω load, the RMS error between the calibrated temperature and the measured temperature is 8 mK, well within the 1σ noise level (bottom right panel of fig. 4.7). This level of accuracy is comparable to the 26 mK noise floor estimated for the EDGES pipeline in 2016 [43].

4.2.5 Waiting for REACH: Results with a HERA receiver

The comparable results of our preliminary technique and the independent EDGES framework serves as a verification of our formulation which would need to be evaluated using real data. While awaiting construction of the REACH hardware a HERA Front End Module (FEM) was employed as a sufficient proxy for data collection. The FEM's Cambridge-led

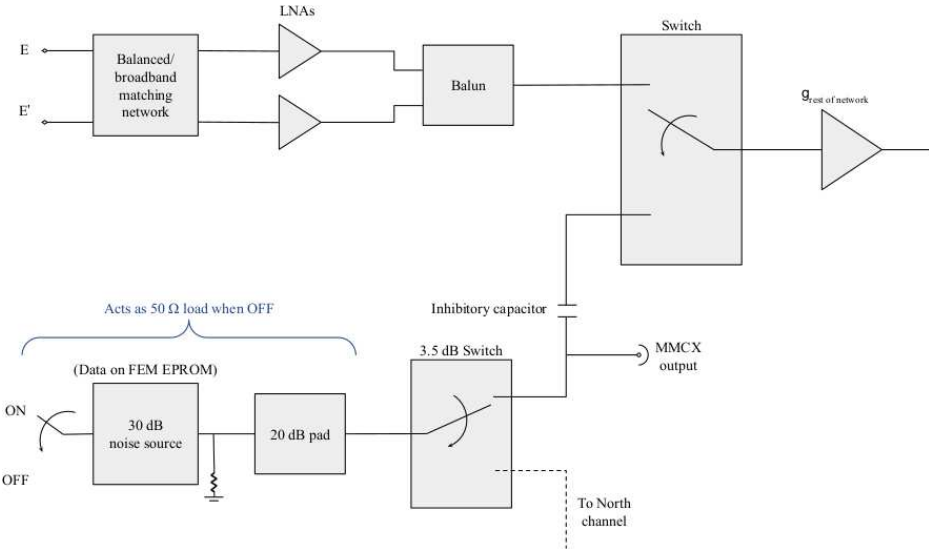


Fig. 4.8 A block diagram of the HERA Front End module East channel input. The module input, marked E and E', is immediately followed by two low noise amplifiers before a balun converts the signal to a feed line into the internal switch. The switch toggles between the FEM input and a contraption acting as a passive 50Ω load or a 6.5 dB noise source when powered. The MMCX output allows for rerouting of the internal reference outputs. The circuitry following the internal switch approximates that of the REACH front-end receiver, permitting normal operation of our calibration procedure.

design and construction, along with HERA's targeting of similar radio-frequency hydrogen signals ensured that similar technologies were incorporated into its architecture including a switch for comparison of the module input with two internal references. Some of the FEM design considerations accommodating the experimental requirements of HERA needed to be addressed, most notably; a pair of low noise amplifiers between the module input and the internal reference switch. The inclusion of these amplifiers, highlighted in fig. 4.8, invalidate the assumption of $g_{\text{sys}} \approx g_{\text{sys}}^*$ for this receiver design. To account for this with minimal changes to our pipeline, we sought to quantify the gain of the FEM's anterior amplifiers as a corrective factor to be applied to spectral measurements before submission to our pipeline as ordinary data^c.

Appraisal of the FEM amplifiers required physical modifications to the device such as the removal of an inhibitory capacitor to impedance match the internal references with the rest of the circuit. Following this, the internal switch measures the references directly without amplification. An MMCX output linked to the internal references is then used to redirect their output to the module input where the data would pass through the low noise amplifiers

^cThis assumes that the gain of the HERA hardware is strictly linear, which is reasonable based on the design specifications.

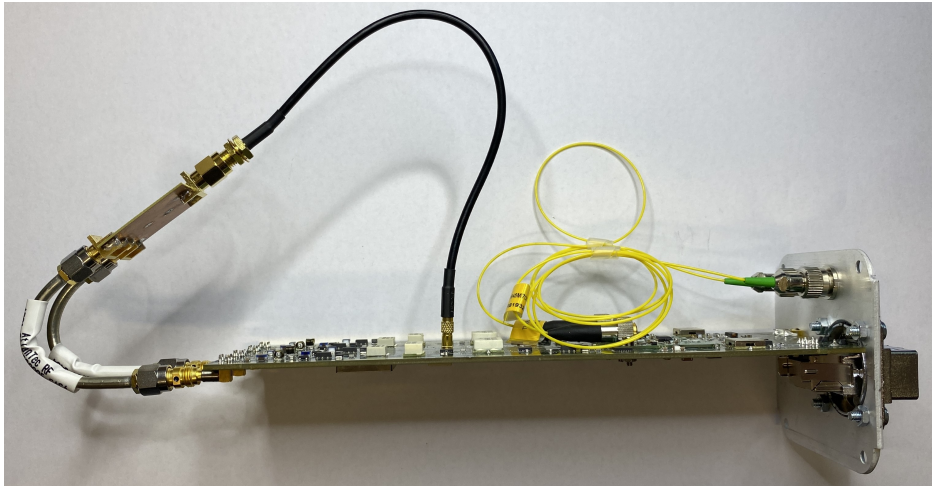


Fig. 4.9 A HERA Front End Module without its housing, configured to evaluate anterior LNA gain. At the board's centre is the internal reference MMCX output connected to a hybrid splitter which bisects the signal into a pair separated by a 180° phase difference. The signal is then directed to the module input for measurement of the amplifier effects on the internal references.

before being measured. An image of the setup used to reroute the internal references to the FEM input is shown in fig. 4.9. As shown in fig. 4.10, the amplified reference load signal resembles an upward shift and broadening of the direct signal, which we approximate as a frequency-dependent multiplicative factor executed by the LNAs. The same behaviour can be seen in the internal noise source data (not shown) and is consistent over multiple data runs. We therefore compile spectral data for this receiver in a three-step process; 1) measurement of the calibrators at the module input followed by 2) direct measurement of the Dicke references via internal switch. 3) The corrective factors derived from the MMCX output procedure are then applied to the internal reference load and noise source data to effectively equalise the gain over all spectral data before being passed to our pipeline as an ordinary dataset. This operation allowed us to avoid the complications of manually switching the calibration sources and rerouted reference signals at the FEM input when ‘cycling’ through the Dicke switch.

As the internal reference connection to the module input shown in fig. 4.9 prevented use of the FEM in its regular housing, data collection was undertaken with the device placed in a RF-secure chamber similar to the Rittal AE 1007.600 enclosure detailed in section 2.1.1. The FEM output was connected to the same iTPM used for REACH acting as a spectrometer and reflection data was taken with a Keysight N5247A PNA-X. A single temperature reading was recorded at the beginning of each device’s respective spectral measurement via thermocouple.

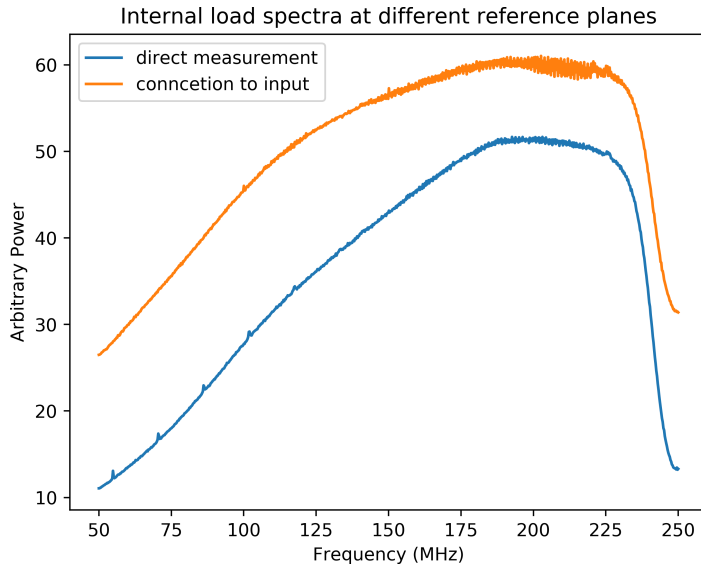


Fig. 4.10 Comparison of data from the reference load when measured directly thorough the internal switch (blue) and when directed to the module input via MMCX output (orange). The apparent action of the amplifiers on the redirected data can be approximated as a frequency-dependent multiplicative factor which is applied to the internal reference data before submission to our pipeline.

Under this configuration, four calibrators were used; an ambient temperature 50Ω load, a 50Ω load heated to 373 K, a 12.5 metre TCOM-200 cable with an opened end, and the same cable with a shorted end. The derived solution was then calibrated against an ambient temperature HERA noise filter. The results, plotted in fig. 4.11, show 1000 model samples from our posterior achieving a 236 mK RMS error and a noise term $\sigma = 3.942$ K under our formulation THERE SHOULD BE AN EQUATION FOR SIGMA SOMEWHERE. While the sub-kelvin error is encouraging, the solution however does not centre on the temperature of the noise filter measured to be 300.4 K. It is understood that more accurate measurements of the 50Ω load calibration sources would improve this as adjustments to this data translate the solution up and down accordingly. This finding informed the design of the REACH front-end to record temperature over the entire period of a calibrator's spectral measurement. Also seen in the solution is sinusoidal structure across the entire bandwidth suggesting a systematic not being accounted for. As the load-based calibrators determine the temperature scale of the solution, the cable-based sources characterise its shape, e.g. cable information is somehow not being captured by our algorithm. Repeated results such as these were the motivation to include a more accurate temperature model for the cable calibration sources as detailed in REFERENCE SECTION ON CABLE CORRECTION. We also note that the calibration accuracy using a HERA FEM is limited by the Noisecom NC4959 used as the

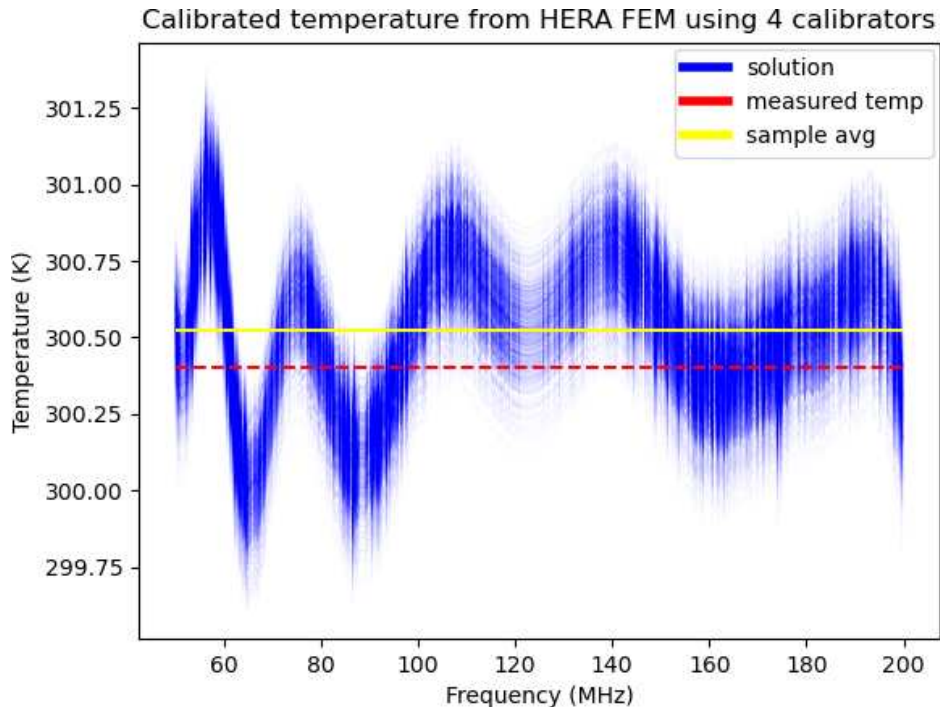


Fig. 4.11 1000 posterior samples from our calibration algorithm using data collected with a HERA FEM are shown in blue. The solution is derived from four canonical sources calibrated against an ambient-temperature noise filter. The integration time for spectral measurements was not recorded for this experiment but was likely 2 minutes as this was our standard for such experiments. While the solutions exhibit a 236 mK RMS error, they do not centre on the measured temperature of the noise filter at 300.4 K shown in red. Ignoring the measured noise filter temperature, the RMSE of the 1000 samples from their average shown in yellow is 212 mK. Sinusoidal structure can be seen across the bandwidth suggesting a cable-based systematic not being captured by our technique.

reference noise source, which varies in output by ~ 1 dB compared to the NC346A used in the REACH front-end which varies by 0.2 dB over the observation band (see table 2.1). We therefore believe that our RMSE of ~ 200 mK approaches the limit for this particular device using our algorithm. A full schematic of the HERA FEM as well as images of the circuit board are given in fig. A.5 and fig. A.6 for reference.

4.2.6 REACH Results?

Data collection using the REACH receiver system commenced once the majority of construction was completed. In the laboratory, automated data sets were taken using the front and back-ends linked by 100 metres of fibre cabling wound over a spool to represent the entire length of the signal chain deployed in South Africa (fig. 4.12).



Fig. 4.12 Due to space constraints within the lab, 100 metres of fibre optic cabling were wound over a spool to verify communication between the receiver front and back-end units over the planned deployment separation as detailed in section 2.1.

Mock antenna results 1

An initial dataset was taken using all 12 calibration sources detailed in section 2.1.1 integrated for two minutes each (e.g two minute integrations on the source, then two minutes on the reference load, followed by two minutes on the reference noise source, repeated for each calibration source). For this particular experiment, it should be noted that data was taken with the front-end components assembled outside of the thermal enclosure, which is expected to negatively affect calibration accuracy. The resulting calibration solution is applied to an ambient-temperature noise filter used as our mock antenna as in the previous section. A plot of 1000 sampled solutions, shown in fig. 4.13, once again does not centre on the measured mock antenna temperature of 302.8 K and achieves an RMSE of 1.075 with respect to it. An RMSE recalculated with respect to the sample average is 689 mK and our posterior error term $\sigma = 4.041$ K.

These results using the REACH receiver system exhibit much less structure than that of the HERA FEM, however the solution still does not resemble Gaussian noise as would be expected from a successful calibration. The average of the posterior samples shown in yellow once again does not correspond to the measured temperature of the mock antenna shown in red. There are also a few spikes in the solution that stand out qualitatively which we take to be RFI. We attribute the defects of our results to the absence of the front-end enclosure and the lack of its accompanying features such as the thermal management subsystem and RFI shielding. We also note the differences between the reported root mean square errors and our

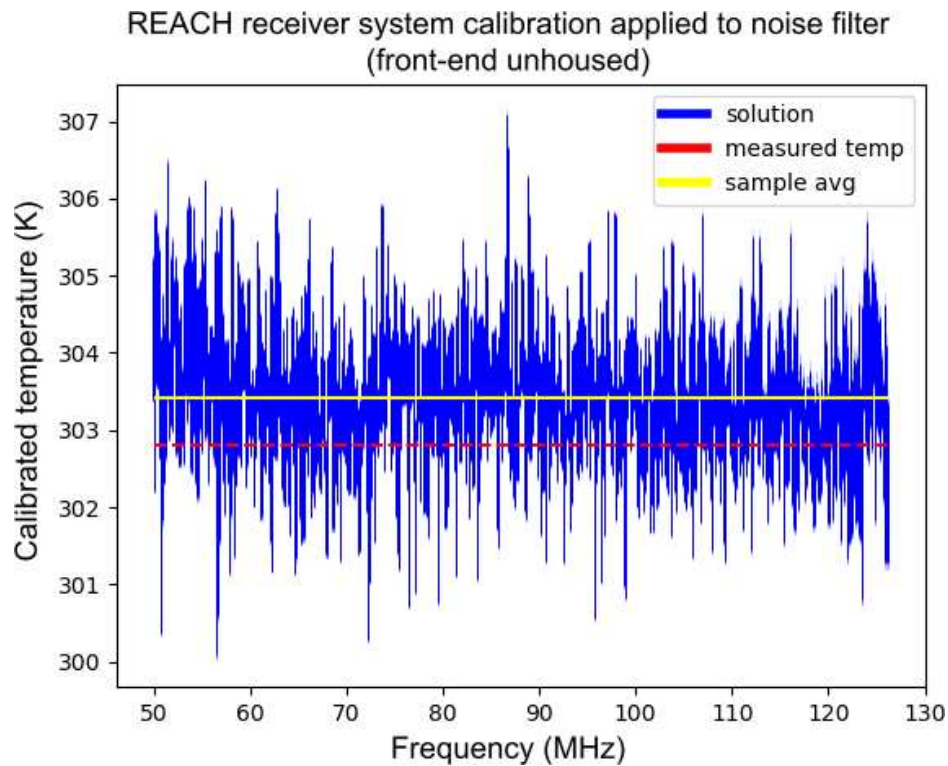


Fig. 4.13 1000 posterior samples from our calibration pipeline using data taken with the REACH receiver system is shown in blue. The front-end did not have its enclosure during data collection for this experiment. All twelve calibration sources were integrated for two minutes and the solution was applied to a room temperature noise filter as our mock antenna. The measured antenna temperature is 302.8 K (red line) which differs from the sample average (yellow), however less structure can be seen than in fig. 4.11. The RMSE is 1.075 K with respect to the measured antenna temperature and 689 mK with respect to the sample average. Our posterior error term $\sigma = 4.041$ K.

error term, σ . We approached this by reformulating our priors starting with setting the prior on our shape parameter

$$a = 1, \quad (4.1)$$

which, for our inverse-gamma prior, corresponds to being very wide while still remaining normalised. We see in MEAN VARIANCE EQUATIONS IN INV-GAM DISTRIBUTION WIKIPEDIA PAGE, that there is no mean or variance for $a = 1$, indicating that the distribution is heavily tailed while reaching a peak at $b/(a + 1)$. Our prior for the scale parameter is therefore

$$b = (a + 1) \times \left(\frac{\sigma_p}{300} \right)^2. \quad (4.2)$$

Here σ_p is the level of noise which we expect to find which we appraise to be ~ 1 K based on our instrument construction. Additionally, b is normalised by our assumed ambient temperature of 300 K which is then squared, giving b dimensions of temperature squared. Our priors for the statistical spread of each of our five noise wave parameter values are set to 10. Given the $a + 1$ term in eq. (4.2), this corresponds to five σ widths and is dimensionless. We can confirm that the results are relatively insensitive to changes in the priors for our noise wave parameter values as the priors are very wide and we use a large amount of training data. Using our formulation for our updated prior volume \mathbf{V}^* in eq. (3.20), our posterior error term

$$\sigma^2 = \Sigma^* = \left(\frac{b^*}{a^*} \right) \mathbf{V}^*, \quad (4.3)$$

which has dimensions of normalised temperature. We believe this reformulation to be robust and verified that the expected results are recovered using simulated data.

Mock antenna results 2

As we continued to construct the receiver, many components required replacement including the TEC power supply, VNA, iTPM and the USB-to-fibre converter. While we do not expect these replacements to affect our calibration results, we report them here for the sake of documentation or consideration in future analyses. To better assess the capabilities of our pipeline, a mock antenna was built to resemble the S_{11} of the deployed antenna dipole based on simulations provided by CITE JOHN CUMNER. This mock antenna was made by soldering a 90Ω load to the end of a 2 metre coaxial cable, providing an S_{11} varying between -11 dB and -14 dB as shown in fig. 2.24. With this configuration, 16-minute integrations were performed on eight calibration sources; the ambient and heated 50Ω loads, shorted and open cables, 25Ω and 100Ω resistors, and the 12 metre calibration cable terminated at 27Ω and 91Ω . The calibration solution applied to our mock antenna is shown in fig. 4.14 and yields a

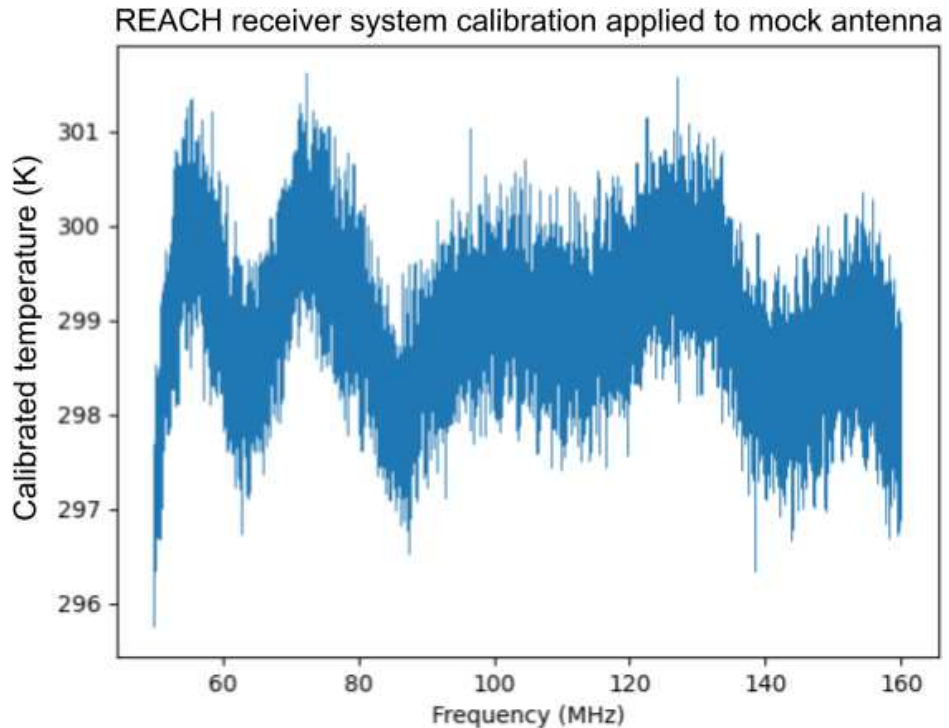


Fig. 4.14 1000 posterior samples from our calibration pipeline using data taken with the completed REACH receiver system including the front-end enclosure. Eight calibration sources were integrated for 16 minutes and the resulting solution was applied to a new mock antenna resembling the reflection characteristics of the deployed antenna dipole. A posterior error $\sigma = 1.464$ K is achieved.

$\sigma = 1.464$ K. The calibration results are seen to have a clear sinusoidal systematic which we attribute to some physical phenomena not being accounted for or incorporated into our pipeline.

4.3 Responses

The sinusoidal structure seen in both fig. 4.11 and fig. 4.14 indicate systematics needing to be addressed. The two typical avenues of approach are to; a) find and attend to the physical source of the systematic (loose wire, etc) and b) incorporate better numerical models into our algorithm to incorporate the information not captured presently. For the engineer, the former is often attempted first, and for the statistician, the latter. One may argue that a perfect calibration algorithm should account for any systematic, which perhaps is true. In practice however, incorporating a myriad of models for every potential loose wire at every connection or the impedance changes of every component with every degree of temperature increase

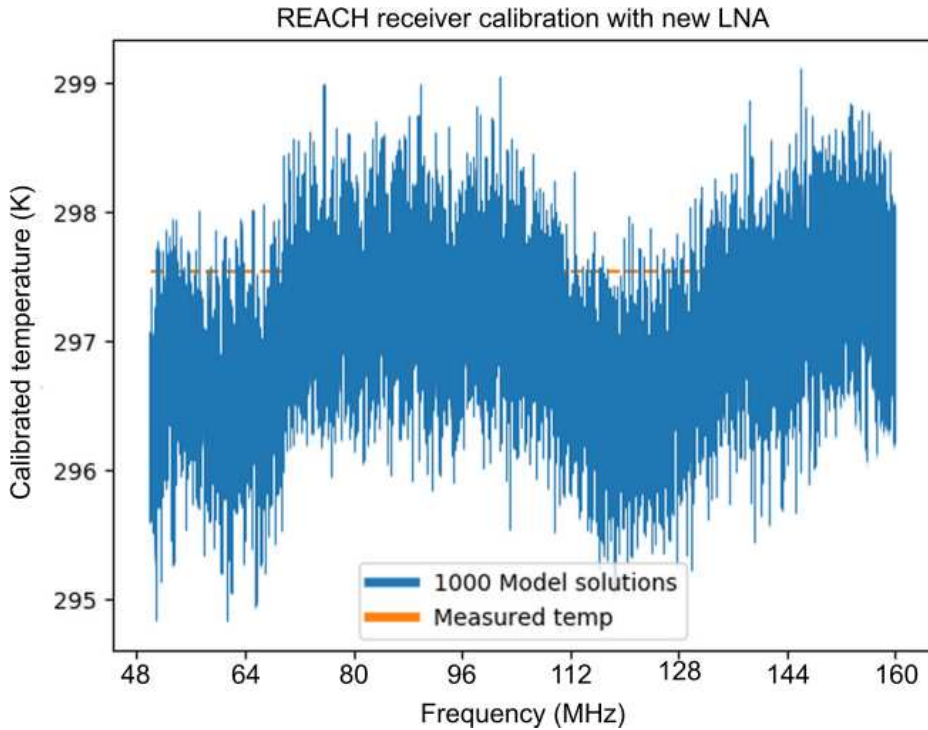


Fig. 4.15 Results from our calibration pipeline using data taken as in fig. 4.14 but with a new LNA built to identical specifications. As can be seen, some of the sinusoidal structure has been ameliorated suggesting that a component within the original LNA was partially at fault. 1000 posterior samples are shown in blue. Eight calibration sources were integrated for 16 minutes and the resulting solution was applied to the mock antenna. The posterior error is $\sigma = 1.070 \text{ K}$.

proves difficult. The approach of identifying physical faults with the instrument tends to yield more immediate results as well, as shown in fig. 4.15 where the front-end low noise amplifier was replaced with a new construction of identical specifications.

The results of fig. 4.15 show a marked decrease in sinusoidal structure, but still exhibits systematics indicating the need for further adjustment. A great deal of attempts to physically rectify the systematic were made that provided little or no improvements to the results. We first recollected datasets with increased and decreased out-of-band 10 MHz tone injection through the application or removal of attenuators at the amplifier output. This was thought to better calibrate short-term variation in the spectrometer over the course of the three-position Dicke cycle during measurements through the division of power spectral measurements in eq. (3.4), though no change in results were seen. We next took datasets at different front-end TEC setpoints, having it maintain a variety of different temperatures. While the calibration results did not improve for these runs, we can confirm that instructing the machine to maintain

a set point closer to the outside ambient temperature has beneficial effects on the power consumption of the machine, as one would expect.

Following this, we noted the possibility of a small, hertz or kilohertz-level misalignment of measurement frequency bins between the VNA and spectrometer due to the devices being separate machines taking independent frequency measurements. In response to this, we employed a Stanford Research Systems FS725 Rubidium Frequency Standard as an external reference connected to the VNA and spectrometer for a true frequency-by-frequency bin matchup. While data sets using this setup did not yield noticeable improvement, suggesting that at the current calibration scale, kilohertz or lower level bin misalignment would not affect our measurements, we recommend the alignment of the VNA and spectrometer through a similar configuration for future builds. In principle, this would be beneficial as calibration accuracy improves past the ten millikelvin level.

We then proceeded to replace every individual component within the receiver including every switch, the VNA, iTPM spectrometer and USB-to-fibre converters. We experimented with both longer and shorter calibration cables as well as different brands of cabling. The calibration sources were rebuilt and a battery of attenuators and ferrite beads were installed throughout the instrument to reduce any internal electromagnetic interference. Filtering of the RF signals was also tried with no effect. Adjustments were made to the VNA sweep time to compensate for any delays in the signal travelling up and down the length of the calibration cables. We even attempted data runs in which spectral data was taken as normal while reflection data was taken by the Keysight N5247A PNA-X to determine whether or not the specifications of the CMT TR1300/1 were the limiting factor, which was not found to be the case. Setups with the PNA-X and spectrometer aligned by the FS725 Rubidium standard were also investigated with still no rectification of the systematics seen in the results.

We consider the above to be the extent of reasonable adjustments to the physical machine and continue on to the statistician’s approach to systematics—adjustments to our numerical algorithm. We started with reformulating of our priors similar to the procedure of eq. (4.1) through eq. (4.3) under various assumptions such as keeping the priors wide or constraining them based off of noise wave parameter values published by EDGES as well as from our own experience. We however considered equations presented in this chapter to be a good compromise between the best calibration accuracy and the wide priors expected of a comparable frequentist approach. We also experimented with the incorporation of additional corrective factors to compensate unaccounted gain contributions as well as offset factors to correct for minute differences in the measurement reference planes. We improved the gradient descent algorithm that optimises the noise wave parameter polynomial order by refactoring

the code to avoid getting trapped at local minima. Furthermore, we tried smoothing of the data as well as up-sampling and down-sampling of the data.

4.4 Additional models for incorporation

In our experimentation with modifications of our algorithm, we decided on three additional models to be incorporated into our calibration procedure. While these models do not result in immediate practical benefits to our experimental results with regard to the sinusoidal systematics presented above, they serve to reinforce the theoretical foundation on which our algorithm is built. These models are explained below.

4.4.1 Fixture compensation to improve S-parameter measurements

At our desired levels of precision, RF system design must minimise the number of reference planes within the instrument. Each additional reference plane will have its own path-specific signal delays and reflections which slightly alter the data with respect to a measurement device such as the VNA. Preceding the full calibration of the receiver, the VNA is initially calibrated via the SOL standards with respect to the MS2 input reference plane as shown in fig. 2.13. Following this, all further reflection measurements of the calibration sources and LNA are taken with respect to a reference plane at the inputs of the MTS switch, represented by the red dashed lines in fig. 2.13^d.

Omitting any redesign of the front-end, we may attempt to mitigate the effects of the path length through the MTS switch through the techniques of fixture compensation. A particularly accurate method of fixture compensation is the use of scattering transfer parameters (T-parameters), also referred to as ABCD parameters^e [54]. Modelling the MTS+source combination as a cascaded network at the MS2 input reference plane, we may use T-parameters to mathematically de-embed fixtures such as the MTS and remove their effects on the data. For a 2-port network such as the path through the MTS switch, the relation between S-parameters and T-parameters under the scattering transfer convention is defined as

$$T = \begin{bmatrix} T_{11} & T_{12} \\ T_{21} & T_{22} \end{bmatrix} = \begin{bmatrix} \frac{S_{12}S_{21}-S_{11}S_{22}}{S_{21}} & \frac{S_{11}}{S_{21}} \\ \frac{-S_{22}}{S_{21}} & \frac{1}{S_{21}} \end{bmatrix}, \quad (4.4)$$

^dWe take the mechanical switches MS1, MS3 and MS4 to be lossless while assuming the path through the 2-port MTS is non-negligible.

^eAn alternative convention known as chain scattering parameters are also referred to as ‘T-parameters’ and care should be taken to ensure that one’s calculations are consistent to avoid errors

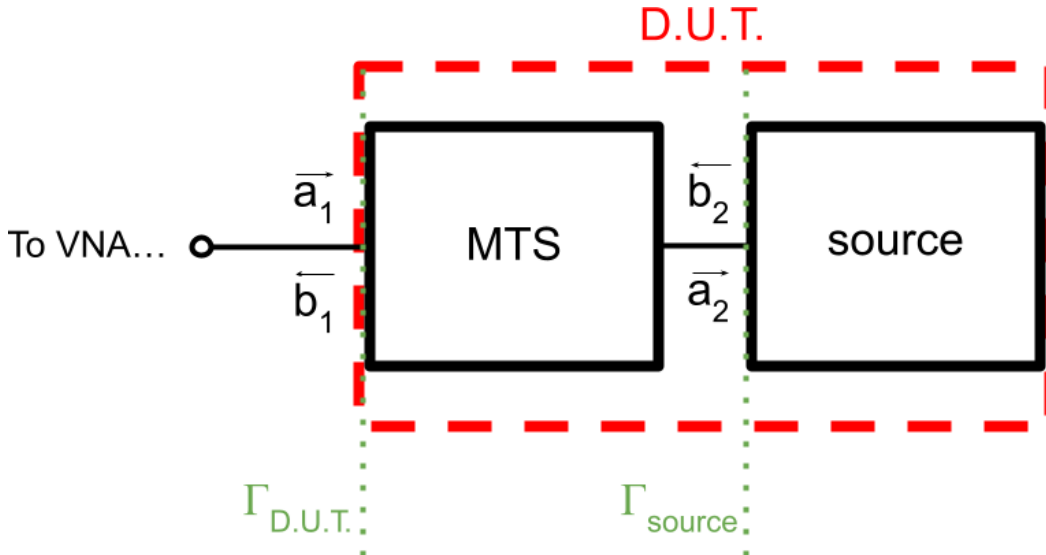


Fig. 4.16 From the perspective of the VNA, a reflection measurement is taken of a single device under test (D.U.T.) consisting of the MTS switch connected to a source. The reflection coefficient measured by the VNA, $\Gamma_{\text{D.U.T.}}$, is altered by the path through the MTS switch. The desired reading is Γ_{source} which needs to be extracted from the D.U.T. measurement.

where the S-parameters in the above matrix are reflection measurements of the offending paths through the MTS switch (e.g. the MTS-J1→MTS-J2 path for calibration sources and MTS-J3→MTS-J4 for the LNA). In the current analysis, measurements of the MTS switch were performed in the laboratory using the Keysight N5247A PNA-X. While this procedure contradicts our philosophy of an all-in-field calibration system, we believe it strengthens the foundation of our overall technique and future work will be undertaken on a system design that either avoids multiple reference planes or facilitates in situ 2-port measurements of the MTS switch.

During a reflection measurement, all the VNA sees is a device under test (DUT) which in reality consists of a calibration source connected to the MTS as shown in fig. 4.16. The traversing and reflected waves are related by

$$\begin{bmatrix} a_1 \\ b_1 \end{bmatrix} = \begin{bmatrix} T_{11} & T_{12} \\ T_{21} & T_{22} \end{bmatrix} \begin{bmatrix} a_2 \\ b_2 \end{bmatrix}, \quad (4.5)$$

where $\Gamma_{\text{source}} = \frac{b_2}{a_2}$ and $\Gamma_{\text{D.U.T.}} = \frac{b_1}{a_1}$. Wanting the reflection coefficient of the source, we expand as a system of equations that can be solved yielding

$$\Gamma_{\text{source}} = \frac{\Gamma_{\text{D.U.T.}} - S_{22}^{\text{MTS}}}{S_{12}^{\text{MTS}} S_{21}^{\text{MTS}} + S_{11}^{\text{MTS}} (\Gamma_{\text{D.U.T.}} - S_{22}^{\text{MTS}})}, \quad (4.6)$$

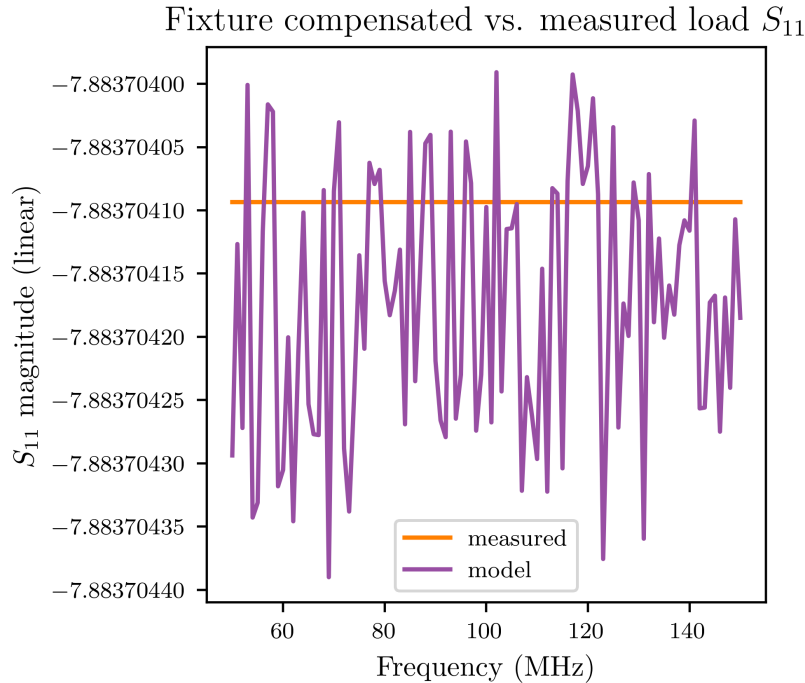


Fig. 4.17 A plot comparing a simulated load and a model derived through fixture compensation. A load+cable configuration was simulated in the PathWave RF Synthesis software which was measured using the tools within the program. Measurements were then taken of the simulated cable on its own which were used to derive T-parameters and de-embed the cable from the fixture. The resulting model for the simulated load is shown in purple and plotted against the in-program measurement of the load shown in orange. We see that the model and measurement agree to within six decimal places. S-parameter magnitudes are shown on a linear scale and S-parameter measurements within the software were noiseless. REPLOT THIS AS THE DIFFERENCE BETWEEN THE DATA AND MODEL RATHER THAN THIS CRAZY THING...

where the S-parameters are measurements of the MTS-J1→MTS-J2 paths for corrections regarding sources and MTS-J3→MTS-J4 for corrections of the LNA reflection coefficient. These corrections are applied to all S-parameter measurements.

Using simulations of a similar cascaded network made with Keysight's PathWave RF Synthesis software, we can confirm that this method of fixture compensation retrieves the source reflection coefficient to within six decimal places as shown in fig. 4.17.

Following the above corrections to the reflection measurements made by the VNA, calibration source S_{11} 's are effectively taken from the MTS-J2 connection while the LNA S_{11} is taken at the MTS-J4 connection. We note however that spectral measurements of the calibration sources must pass through the MTS-J2→J4 path before reaching the LNA as shown by the purple dashed line in fig. 2.13. In other words, the calibration sources see a

D.U.T. consisting of the MTS-J2→J4+LNA that is not seen by the VNA. We must once again use T-parameters to embed the path through the MTS switch onto the LNA reflection measurements to have a matched reference plane for our data. Following a similar calculation as above we find the corrected LNA reflection coefficient to be

$$\Gamma_{\text{LNA}(\text{corrected})} = S_{22} + \frac{S_{12}S_{21}\Gamma_{\text{LNA}(\text{original})}}{1 - S_{11}\Gamma_{\text{LNA}(\text{original})}}, \quad (4.7)$$

where the S-parameters correspond to measurements of the two-port network defined by the MTS-J2→J4 inputs.

4.4.2 Temperature gradients across calibration cables

As shown in THE CALIBRATION SECTION, the accurate readings of the physical temperatures from our calibration sources are crucial for optimal performance. These are typically measured by the TC-08 thermocouples throughout an observation and are assumed to be spectrally flat. This is, however, not entirely accurate as many of our calibration sources are constructed from a resistor terminating a cable which will exhibit a temperature gradient across the cable's length similar to the heated 50Ω load with the resistor heated to 370 K and the connecting end of the device at ambient temperature as shown in HEATED LOAD DIAGRAM. In the case of our calibration cables, a short (2 metre) and long (10 metre) MAKE SURE THESE LENGTHS MATCH THE ONES QUOTED IN THE INSTRUMENTAL CHAPTER are connected the various resistor values by the 12 V MS3 and MS4 switches as represented in fig. 2.13. These powered switches are seen to produce a ~ 3 degree difference between the cable and the resistors resulting in a minor temperature gradient which needs to be accounted for in a manner similar to the heated load as discussed in CALIBRATION MATHS CHAPTER.

We start by calculating the the realised gain of each source path which describes the actual gain that a device is able to achieve taking into account factors such as loss and mismatch

$$G = \frac{|S_{21}|^2 (1 - |\Gamma_R|^2)}{|1 - S_{11}\Gamma_R|^2 (1 - |\Gamma_{\text{src}}|^2)}, \quad (4.8)$$

where S_{11} and S_{22} are the forward S-parameters of the calibration cable in question. The reflection coefficient is also measured of the cable+switch+load construction and of the terminating resistor represented as Γ_{src} and Γ_R respectively with the former being the S-parameter data from our original equations in CALIBRATION MATS SECTION. Using the

realised gain, we can model the effective temperature of each source as

$$T_{\text{src}} = GT_{\text{R}} + (1 - G)T_{\text{cab}}, \quad (4.9)$$

where T_{R} and T_{cab} are the temperatures of the resistive load and cable measured by thermocouple during normal operation.

4.4.3 Temperature gradients across the antenna

For the majority of laboratory measurements, training data from calibration sources is used to derive a calibration solution for the current receiver state which is applied to mock antenna data yielding a calibrated antenna temperature. This mock antenna at the MTS-J2 reference plane, is made from a load-terminated 1 metre cable which also exhibits temperature discontinuities between the load, cable and connection to the MTS input. Following the same principles as section 4.4.2, we compute the available gain using eq. (4.8) and reflection measurements of the antenna construction as well as its constituent cable and load. For our mock antenna, we want T_{sky} which will be the temperature at the terminating load. Rearranging eq. (4.9) for T_{R}

$$T_{\text{ATL}} = \frac{1}{G} (T_{\text{ant}} + (G - 1)T_{\text{cab}}), \quad (4.10)$$

where T_{ATL} is the temperature at the antenna's terminating load, T_{ant} is the temperature of the mock antenna as measured at the receiver input and T_{cab} is the temperature of the cable within the mock antenna construction. T_{cab} can be approximated with the following

$$T_{\text{cab}} = \frac{1}{L_{\text{tot}}} (T_{\text{int}}L_{\text{int}} + T_{\text{ext}}L_{\text{ext}}), \quad (4.11)$$

where T_{int} and T_{ext} represent the internal and external cable temperatures while L_{int} and L_{ext} represent the internal and external cable length. L_{tot} is the total cable length. For our mock antenna, L_{ext} is 100 cm and L_{int} is 28 cm.

During deployment, these corrections may need to be refined to accommodate the response of additional components such as a balun. If the radiation efficiency of the antenna = 1 (i.e. $T_{\text{ant}} = T_{\text{sky}}$), the balun and the antenna feed cable will form two RF networks between the antenna and our reference plane, both of which will be cooler than the hot sky at REACH frequencies. The response of these devices have the potential to impose frequency structure on the calibrated antenna temperature unless similar corrections are applied.

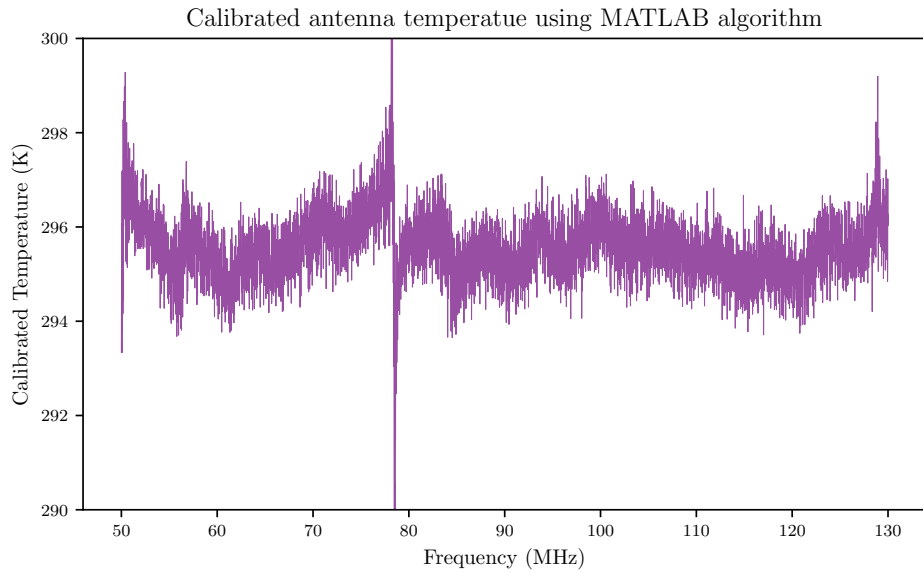


Fig. 4.18 Calibrated temperature of the laboratory-based mock antenna using data from ten calibrators integrated for twenty minutes. No S-parameter, cable temperature gradient or antenna temperature corrections were applied to this solution. The RFI at 78 MHz was excised before calculation of the RMSE relative to the solution average yielding a calibration accuracy of 760 mK. It is evident that without the corrections reviewed in section 4.4.1 section 4.4.2 and section 4.4.3, noticeable structure remains in the result.

4.5 Comparison with least squares algorithm

After evaluating the results from section 4.2.5 through section 4.3 we wanted to determine whether our Bayesian algorithm was the limiting factor in achieving a calibration accuracy on the scale of tens of millikelvin. As a sanity check, an independent pipeline was written in MATLAB following the least-squares solution to a system of linear equations as prescribed in Monsalve et al. [43]. A dataset was taken of 20 minute integrations on ten calibrators; the heated and ambient temperature 50Ω loads, the 25Ω and 100Ω loads, the open and shorted 25 metre cable, and the 12 metre cable terminated with 27Ω , 91Ω , 36Ω and 69Ω resistors. The calculated order-5 noise wave parameters were applied to data of the lab-based mock antenna as described in the previous sections with no corrections applied such as those discussed in section 4.4.1, section 4.4.2, and section 4.4.3. The resulting calibrated antenna temperature is shown in fig. 4.18 where we can see structure throughout the observation band. Significant RFI is seen at 78 Mhz which was excised before calculating an RMSE from the average calibrated antenna temperature yielding an accuracy of 760 mK. Upon applying the S-parameter, cable temperature gradient, and antenna temperature corrections, the accuracy increases, giving an RMSE of 518 mK as shown in fig. 4.19

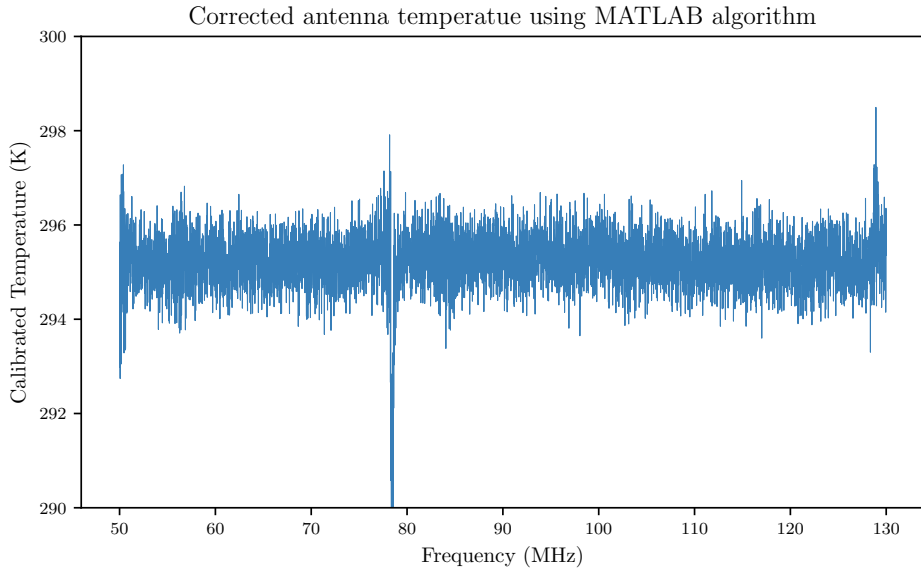


Fig. 4.19 Calibrated temperature using the same experimental setup as in fig. 4.18 but with the S-parameter, cable temperature gradient and antenna temperature correction applied. The structure from the previous solution is mitigated and the calibration accuracy increases to an RMSE of 518 mK (78 MHz excised).

The increase in accuracy exhibited by the MATLAB algorithm is intriguing, though we note that while comparable, the root mean square error relative to the solution average is not strictly the same as the error term σ reported for our Bayesian pipeline. Much of the structure present in fig. 4.18 is reduced by the S-parameter and cable temperature gradient corrections giving calibration accuracies more similar to those of section 4.2.5. It is however unclear if useful information is lost from the data when these corrections are applied. Continued experiments using either on-site data or simulations of astrophysical data will need to be performed for verification.

4.5.1 Averaging results to bring the noise down

We wanted to determine under what conditions we could get a calibration accuracy under 100 mK. While the below method may not adhere entirely to the philosophy of a fast, in-the-field calibration technique, we found the results interesting enough to present here. For this experiment, we took a collection of fifteen independent training datasets of the ten calibrators used in the previous section each integrated for 20 minutes with the TEC set to maintain at 30 °C internal receiver temperature throughout. All of the data was first masked to the 50–130 MHz band followed by the application of the S-parameter and cable temperature gradients discussed in section 4.4.1 and section 4.4.2. Once the \mathbf{X} vector is built following

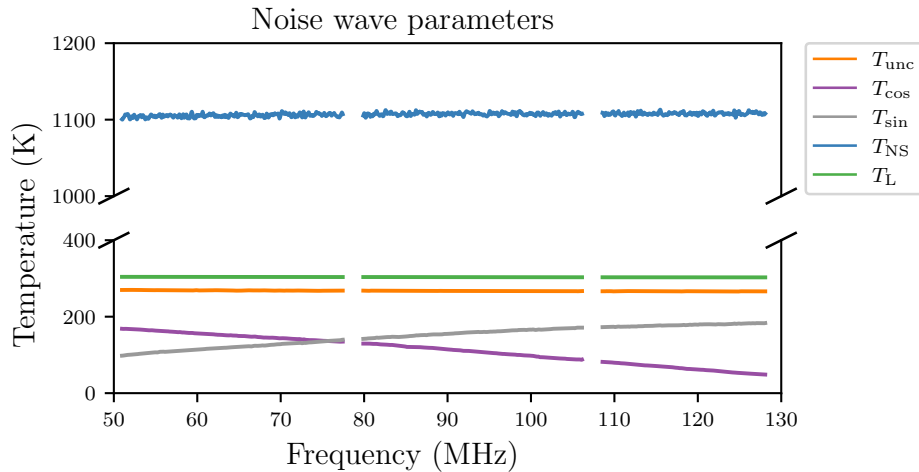


Fig. 4.20 A set of noise wave parameters derived from the least squares algorithm in which ten calibrators were integrated on for 20 minutes each and the resulting \mathbf{X} components were smoothed. Four bands maligned with interference were excised as can be seen at the beginning of the observation band, at 79 MHz, at 108 MHz, and at the far end of the observation band. We can see that T_L has a temperature around 300 K, corroborating the ambient temperature reference load within our Dicke switch. T_{NS} is seen to have a value around 1100 K as predicted from our manufacturer-supplied data from fig. 2.11. We believe that this sanity check partially validates the results of our least squares algorithm.

eq. (3.15), a smoothing spline factor of 0.99999999^f was applied to each element of \mathbf{X} to effectively reduce noise on the reflection measurements.

The resulting fifteen smoothed \mathbf{X} 's were then submitted to the MATLAB least squares pipeline using a Moore-Penrose pseudoinverse to determine the noise wave parameters. Artefacts in the calculated noise wave parameters were the excised through replacement with NaN's corresponding to 6.2 MHz of the 80 MHz-wide observation band. The fifteen noise wave parameter sets, one of which shown in fig. 4.20, were then averaged and the resulting single set of noise wave parameters were then applied to the fifteen sets of mock antenna data which were further corrected using the procedure discussed in section 4.4.3. Finally the fifteen antenna solutions were averaged to produce a solution with a root mean square error of 80 mK from the solution average as shown in fig. 4.21.

The amount of work needed to reduce the calibration error on our mock antenna is intriguing. We suggest that the steps outlined above correspond to an overall reduction of noise with the \mathbf{X} vector smoothing corresponding to the S-parameters (see eqs. (3.9) to (3.13)) and the averaging of the noise wave parameters corresponding to the spectral data indicating that a more accurate VNA and spectrometer may need to be employed. Averaging of the

^fwith a factor of 1 being no smoothing

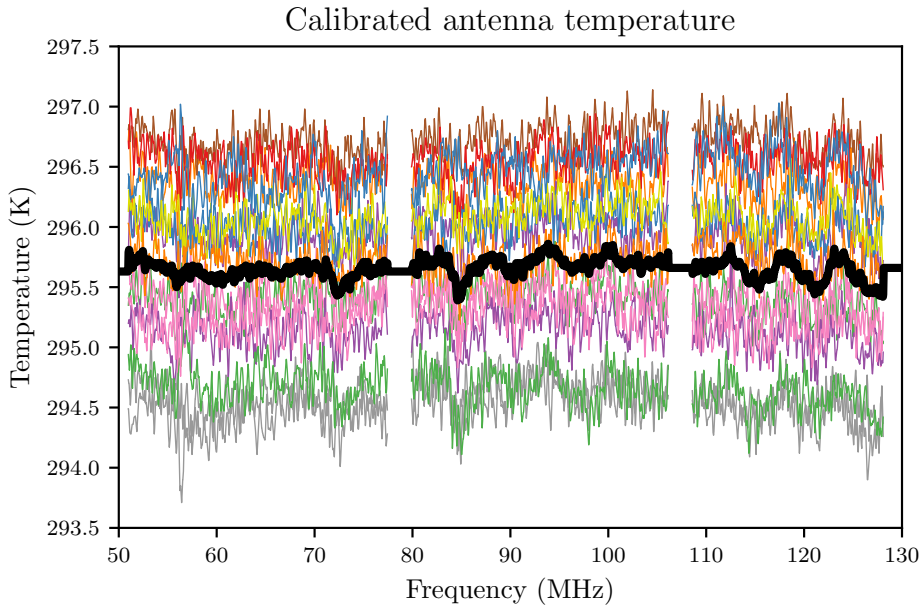


Fig. 4.21 The fifteen corrected calibrated antenna temperatures from our least squares algorithm are plotted in colours following the smoothing and averaging procedures outlined in this section as well as the excision of RFI over four bands. An average of the antenna temperatures is shown in black which yields a RMSE of 80 mK, of the order one would expect for this kind of calibration technique. The relative spread of the coloured solutions demonstrate the time-variability of the receiver system over the 165-hour data acquisition which necessarily needs to be managed to increase calibration accuracy. The application of the smoothing and averaging procedures needed to obtain this result indicate amount of work that must be done both on an instrumental and numerical level.

fifteen solutions indicates that increased integrations of the spectral data also increases the resulting accuracy (as one would expect)^g. The fifteen datasets taken however, correspond to a total 165 hours of spectral integration which is clearly not feasible for an experiment such as ours in which sky data is taken over night for six to eight hours. We also note that within the idealised laboratory environment, the ambient temperature varied by up to 3.5 degrees. While the TEC was able to maintain a relatively stable internal temperature within the receiver front-end, it is unclear how the device will perform over prolonged usage in the Karoo where outside temperatures are assumed to vary by much more.

4.6 A frequency-by-frequency Bayesian solver

One clear difference between our MATLAB and Python calibration pipelines is the least squares solution for noise wave parameters at each frequency compared to the derivation of broadband noise wave parameters as polynomials in frequency, respectively. Independent investigations with a polynomial-based Bayesian pipeline developed by the EDGES team (though, not based on a conjugate prior approach) seem to corroborate our findings that a polynomial model for the noise wave parameters may not be the most appropriate at the desired level of sensitivity [45]. To test this, we developed an additional Bayesian calibration approach that solves for the set of five noise wave parameters at each frequency which we derive here.

As in our CALIBRATION CHAPTER BAYESIAN SECTION derivation, we specify a likelihood as the probability of the data given our model $p(y|\boldsymbol{\theta})$ where we assume that the variation or noise in our data is Gaussian

$$P(y|\boldsymbol{\theta}) = \frac{1}{\sqrt{2\pi C}} \exp \left\{ -\frac{1}{2} (y - \mathbf{X}\boldsymbol{\theta})^\top \mathbf{C}^{-1} (y - \mathbf{X}\boldsymbol{\theta}) \right\}, \quad (4.12)$$

where y is our temperature data, \mathbf{C} is a 5×5 data covariance matrix, \mathbf{X} is a vector of our data terms (eqs. (3.9) to (3.13)) and $\boldsymbol{\theta}$ is a vector of our noise wave parameters T_{unc} , T_{cos} , T_{sin} , T_{NS} and T_{L} , with all terms in eq. (4.12) representative of the values at a single frequency^h. Similar to our derivation in chapter 3, we consider the log likelihood to simplify the analytic calculations and promote numerical stability. Expanding the expression in the exponential and reminding ourselves of the property regarding the transpose of a matrix product, $(\mathbf{AB})^\top =$

^gThis may be verified by visible inspection of calibration solutions with increased integration time

^hNotice that \mathbf{X} and $\boldsymbol{\Theta}$ from BAYESIAN CALIBRATION SECTION were matrices with one of the axes being across frequency.

$$\mathbf{B}^\top \mathbf{A}^\top;$$

$$\log \mathcal{L} = -\frac{1}{2} \log |2\pi \mathbf{C}| - \frac{1}{2} (\mathbf{y} - \mathbf{X}\boldsymbol{\theta})^\top \mathbf{C}^{-1} (\mathbf{y} - \mathbf{X}\boldsymbol{\theta}) \quad (4.13)$$

$$= -\frac{1}{2} \log |2\pi \mathbf{C}| - \frac{1}{2} \mathbf{y}^\top \mathbf{C}^{-1} \mathbf{y} + \frac{1}{2} \mathbf{y}^\top \mathbf{C}^{-1} \mathbf{X} \boldsymbol{\theta} + \frac{1}{2} \boldsymbol{\theta}^\top \mathbf{X}^\top \mathbf{C}^{-1} \mathbf{y} - \frac{1}{2} \boldsymbol{\theta}^\top \mathbf{X}^\top \mathbf{C}^{-1} \mathbf{X} \boldsymbol{\theta}. \quad (4.14)$$

We then define the terms

$$\boldsymbol{\Sigma}^{-1} := \mathbf{X}^\top \mathbf{C}^{-1} \mathbf{X}, \quad (4.15)$$

$$\boldsymbol{\mu} := \boldsymbol{\Sigma} \mathbf{X}^\top \mathbf{C}^{-1} \mathbf{y}, \quad (4.16)$$

where $\boldsymbol{\Sigma}$ is our 5×5 parameter covariance matrix and $\boldsymbol{\mu}$ is a length-5 vector of noise wave parameter distribution means. We then add and subtract the term $\frac{1}{2} \boldsymbol{\mu}^\top \boldsymbol{\Sigma}^{-1} \boldsymbol{\mu}$ to eq. (4.14), substitute eq. (4.15) and eq. (4.16) followed by a rearrangement of terms,

$$\begin{aligned} \log \mathcal{L} &= -\frac{1}{2} \log |2\pi \mathbf{C}| - \frac{1}{2} \mathbf{y}^\top \mathbf{C}^{-1} \mathbf{y} + \frac{1}{2} \boldsymbol{\mu}^\top \boldsymbol{\Sigma}^{-1} \boldsymbol{\mu} \\ &\quad - \frac{1}{2} \boldsymbol{\theta}^\top \boldsymbol{\Sigma}^{-1} \boldsymbol{\theta} + \frac{1}{2} \boldsymbol{\theta}^\top \boldsymbol{\Sigma}^{-1} \boldsymbol{\mu} + \frac{1}{2} \boldsymbol{\mu}^\top \boldsymbol{\Sigma}^{-1} \boldsymbol{\theta} - \frac{1}{2} \boldsymbol{\mu}^\top \boldsymbol{\Sigma}^{-1} \boldsymbol{\mu}, \end{aligned} \quad (4.17)$$

where we condense the second line of eq. (4.17) (compare to the expansion of eqs. (4.13) and (4.14)),

$$\log \mathcal{L} = -\frac{1}{2} \log |2\pi \mathbf{C}| - \frac{1}{2} \mathbf{y}^\top \mathbf{C}^{-1} \mathbf{y} + \boldsymbol{\mu}^\top \boldsymbol{\Sigma}^{-1} \boldsymbol{\mu} - \frac{1}{2} (\boldsymbol{\theta} - \boldsymbol{\mu})^\top \boldsymbol{\Sigma}^{-1} (\boldsymbol{\theta} - \boldsymbol{\mu}). \quad (4.18)$$

Re-exponentiating to retrieve our likelihood we have,

$$\begin{aligned} \mathcal{L} &= |2\pi \mathbf{C}|^{-\frac{1}{2}} \times \exp \left\{ -\frac{1}{2} \mathbf{y}^\top \mathbf{C}^{-1} \mathbf{y} \right\} \times \exp \left\{ \frac{1}{2} \boldsymbol{\mu}^\top \boldsymbol{\Sigma}^{-1} \boldsymbol{\mu} \right\} \\ &\quad \times \exp \left\{ -\frac{1}{2} (\boldsymbol{\theta} - \boldsymbol{\mu})^\top \boldsymbol{\Sigma}^{-1} (\boldsymbol{\theta} - \boldsymbol{\mu}) \right\}. \end{aligned} \quad (4.19)$$

We desire to find the set of noise wave parameters with the maximal evidence at each frequency. The analytic equation for the evidence, \mathcal{Z} , is

$$\mathcal{Z} = \int \mathcal{L} \frac{1}{\mathbf{V}} d\boldsymbol{\theta}, \quad (4.20)$$

where our prior volume \mathbf{V} makes $\frac{1}{\mathbf{V}}$ our prior distribution and we are integrating over the space of possible noise wave parameters $\boldsymbol{\theta}$. Plugging in our expression for \mathcal{L} and factoring

from the integral terms independent of $\boldsymbol{\theta}$,

$$\mathcal{Z} = \frac{1}{\mathbf{V}} |2\pi\mathbf{C}|^{-\frac{1}{2}} \times \exp \left\{ -\frac{1}{2} \mathbf{y}^\top \mathbf{C}^{-1} \mathbf{y} \right\} \times \exp \left\{ \frac{1}{2} \boldsymbol{\mu}^\top \boldsymbol{\Sigma}^{-1} \boldsymbol{\mu} \right\} \times \int e^{-\frac{1}{2} (\boldsymbol{\theta} - \boldsymbol{\mu})^\top \boldsymbol{\Sigma}^{-1} (\boldsymbol{\theta} - \boldsymbol{\mu})} d\boldsymbol{\theta}, \quad (4.21)$$

where we recognise the terms in the intergral as a Gaussian multiplied by its normalising constant,

$$\mathcal{Z} = \frac{1}{\mathbf{V}} |2\pi\mathbf{C}|^{-\frac{1}{2}} \times \exp \left\{ -\frac{1}{2} \mathbf{y}^\top \mathbf{C}^{-1} \mathbf{y} \right\} \times \exp \left\{ \frac{1}{2} \boldsymbol{\mu}^\top \boldsymbol{\Sigma}^{-1} \boldsymbol{\mu} \right\} \times |2\pi\boldsymbol{\Sigma}|^{\frac{1}{2}}. \quad (4.22)$$

It is this equation that we will attempt to maximise with a gradient descent giving us noise wave parameter distribution means ($\boldsymbol{\mu}$), spreads and covariances ($\boldsymbol{\Sigma}$) that are best supported by the data. From Bayes' theorem our posterior distribution, P , for our noise wave parameters is,

$$\log P = \log \mathcal{L} + \log \frac{1}{\mathbf{V}} - \log \mathcal{Z}. \quad (4.23)$$

Plugging in the logged expressions for eq. (4.19) and eq. (4.22), we find many of the terms cancel. Exponentiating our logged posterior reveals yet another Gausian form,

$$P(\boldsymbol{\theta} | \mathbf{y}) = \frac{1}{\sqrt{2\pi\boldsymbol{\Sigma}}} e^{-\frac{1}{2} (\boldsymbol{\theta} - \boldsymbol{\mu})^\top \boldsymbol{\Sigma}^{-1} (\boldsymbol{\theta} - \boldsymbol{\mu})}, \quad (4.24)$$

where we build a multivariate noise wave parameter posterior distribution from the optimised $\boldsymbol{\mu}$ and $\boldsymbol{\Sigma}$ from the maximised evidence.

Upon inspection of the likelihood (eq. (4.19)), evidence (eq. (4.21)) and posterior (eq. (4.24)), we point the common Gaussian form. Our prior distribution for the noise wave parameters however is an unregulated uniform prior eqaul to one over the prior volume, \mathbf{V} , and effectively an infinite-length rectangle in every direction in parameter space. By selecting a Gaussian form for our priors, we may be able to mitigate points corrupted by interference through constraint to values surrounding distribution means. Further exploration and testing of priors is intended to be a topic of future work.

Chapter 5

Conclusions

In this thesis, we explored methods for improving the measurement accuracy of radio-frequency receivers for inclusion in the emerging frontier of astrophysics experiments targeting 21-cm hydrogen signatures from the Cosmic Dawn and Epoch of Reionisation. Investigation of these unexamined windows of cosmic history offer new insights into open questions such as the development of structure in the universe [27], the nature of dark matter [36], as well as constraints on inflationary theories and spatial curvature [11, 37]. With such a broad potential for cosmological insight, analysis of these hydrogen signatures is categorised as an area of scientific importance in the 2020 National Academy of Sciences decadal survey [48] and has spawned numerous experiments attempting detection including EDGES [44], HERA [21] and the SKA [22].

Models for the 21-cm signal, thought to be minute spectral fluctuations redshifted to radio frequencies, are shown to be orders of magnitude smaller than galactic foregrounds [61], with terrestrial interference [20] and even the thermal noise of electronic detection equipment posing a significant challenge to scientific analysis. Such considerations highlight the need for novel instrument design and advanced numerical algorithms to maximise the prospects of experiments. In chapter 2, we presented the architecture and construction of a high-quality radio-frequency receiver for deployment in the South African Radio Astronomy Observatory as part of the REACH experiment [20]. The receiver unit utilises a Dicke switching procedure to mitigate time-variation of the system gain while incorporating up to twelve calibration sources to provide a substantial amount of training data and facilitate the derivation of calibration parameters. A compact design including an onboard VNA, LNA and temperature control system promotes an *in situ* calibration with automation scripts, crash and backup routines ensuring that the device works with minimal human intervention.

Informing the receiver design was the parallel development of a numerical calibration method named EXCALIBRATE. Based on the noise wave formulation of calibration parame-

ters [40], EXCALIBRATE expands on the calibration algorithm developed for the EDGES experiment [43] by introducing a Bayesian approach to the derivation of these ‘noise wave parameters’. Central to our technique is the utilisation of conjugate priors, giving a closed-form solution for our noise wave parameters and yielding a fast algorithm further promoting characterisation of the instrument in the same environment as the data acquisition- -a first of its kind for this type of experiment. Additionally, our procedure incorporates possible correlation between calibration parameters during their derivation and features individual optimisation of parameters which prevents overfitting of the data that may hamper detection of the hydrogen signature.

Our calibration method has been tested with data taken from the REACH receiver at various points of construction as well as with a HERA front end module. In our tests, significant kelvin-level structure were seen in the results despite physical modification to the receiver and, numerical adjustments and revisions of our Bayesian model suggesting that the derivation of calibration parameters as broadband polynomials in frequency may be inadequate for the desired levels of accuracy for modern experiments. Furthermore, results from an independent investigation by the EDGES group seem to corroborate our findings indicating the need for an alternative approach if advancements in calibration technology are to continue [45].

Following these findings, additional tests were conducted using a separate procedure employing a least squares algorithm to determine the noise wave parameters on a frequency-by-frequency basis which exhibited less chromaticity in the results. We then presented a framework for a Bayesian frequency-by-frequency solver which may be developed to yield a calibration accuracy at the tens-of-millikelvin level.

5.1 Future work

As made clear by the results presented in this thesis, there are multiple avenues of further research for increasing instrument sensitivity and accuracy including the development of a more robust numerical calibration algorithm, improvements to the receiver design as well as the continued deployment of the REACH experiment. Our Bayesian pipeline developed in chapter 3 currently gives calibration solutions with a variation σ around 1 kelvin, much too large to confidently identify the cosmic 21-cm signature believed to have a magnitude up to 250 mK according to theoretical models and up to 500 mK if the EDGES results can be confirmed [18, 15]. Although we have suggested continued work on a frequency-by-frequency solver, the 500 mK accuracy achieved by the precursor MATLAB algorithm still contains too much noise to make a detection.

A more advanced procedure was developed where power and reflection measurements are submitted to a simulation based inference algorithm to learn corresponding calibrator temperatures following a neural ratio estimator framework. Once trained, input of the antenna measurements would ideally give a calibrated temperature probability distribution. It was seen however that the software did not generalise to higher temperatures like the antenna leading to unsatisfactory results. Improvements to the technique are anticipated which will attempt to learn g and T_{rec} instead as these values are expected to be more stable across measurements^a. We do recommend that caution be taken with such approaches based on neural networks as the solution may open an interpretability issue when reporting results [74].

Another potential subject of continued investigation is the inclusion of a more advanced noise model in our pipeline. Currently, we assume that the noise on calibration measurements is Gaussian and uncorrelated which may not be true. It may be reasonable to expect that noise in neighbouring frequency bins is correlated which diminishes at frequency bins that become increasingly distant. We certainly see empirically that non-ideal behaviour increases with decreasing wavelength which is typical in RF applications. Inclusion of a Gaussian process that models this may be beneficial for identifying noise in parameter derivation. As briefly mentioned in section 4.6, stepping away from unregulated priors may also be advantageous.

Spikes from electromagnetic and radio-frequency interference also pose issues in the detection of minute cosmic signals. In the results presented throughout this work, point-like RFI were exhibited at precise frequencies which could be excised through typical numerical masking procedures. While a Bayesian RFI flagger has been developed by Leeney et al. [34], we also raise concern with the possibility of broadband RFI corrupting the data. This form of interference, which would affect an extended band of frequencies in more subtle ways than spikes present in the data, may be more difficult to identify and remove. Similar issues are under consideration in related experiments such as HERA [33].

As demonstrated in section 4.5.1, continued integration during spectral measurements may also increase calibration accuracy. The extreme example presented in section 4.5.1 results from a combined 165 hours of integration which is not very feasible based on the long-term variability of the instrument as well as an obvious disjoint between time spent on calibration measurements versus sky observations. Considerations for how to reduce the time needed on calibration measurements will need to be explored. For instance, the needed levels of averaging and smoothing suggest the employment of a better spectrometer and VNA unit respectively. Much of the time spent on calibration is integration on calibration sources. Implicit in much of this thesis are questions about how many calibrators are needed

^aContact Dr. Harry Bevins (htjb2@cam.ac.uk) for more information.

to provide an adequate set of training data. Historically, measurements of an open or shorted cable were used to determine calibration parameters analogous to our T_{unc} , T_{\cos} and T_{\sin} [58] with the ambient and heated load providing the main temperature references for the remaining parameters [43]. As shown by our simulated results in section 4.2, constraints on the noise wave parameter posteriors increased with additional calibrators, however each additional calibrator provided diminishing returns with regard to the amount of information gained (see fig. 4.4). Conversely, a large set of available calibration sources may be beneficial during deployment as described in section 4.5 where data from two of the calibrators was found to be inconsistent with the remaining data and were thus excluded from the analysis. If it is determined that less calibration sources are needed to achieve the desired level of quality in the data, ports on the MS1 switch may be vacated for the S-O-L standards used in VNA calibration which would avoid the need for the S-parameter modelling prescribed in section 4.4.1.

Some general areas for consideration include a better grasp of the calibrator temperatures during measurement. As shown in section 4.4.2, a model accounting for a temperature gradient across the length of the cable-based calibrators was seen to reduce structure in the results. Improvements to the models may need to be made as calibration accuracy increases to incorporate the temperature of connecting structures such as the MS1, MS3 and MS4 powered switches which have their own temperature profile and heat generation due to frequent toggling. While the TC-08 data logger is limited to eight simultaneous measurements, the Teensy 3.5 microcontroller board can accommodate up to 64 I²C temperature probes. This would allow for temperature measurement of each calibrator termination, the mechanical switches as well as on multiple points along the calibrator cable length which may lead to better informed models further improving measurement quality. The correction for the laboratory-based antenna in section 4.4.3 will need to be extended for application to the in-field hexagonal dipole antenna, especially if a device such as a balun is present in the signal chain between the antenna and receiver input. Additionally, models for antenna loss such as those discussed in Rogers and Bowman [58] may need to be applied following a form similar to:

$$T_{\text{corrected}} = \left(T_{\text{raw}} - T_{\text{ambient}} \left(10^{-\frac{l}{10}} - 1 \right) \right) / 10^{-\frac{l}{10}} \quad (5.1)$$

Where l is the antenna loss in dB including ground loss, resistive loss, transmission line loss and balun loss. Furthermore, some concern has been raised regarding the vitality of the thermal management systems in the desert environment of the Karoo. While the systems were adequate in the Cambridge laboratory, they have not been extensively tested in the field. For extended data acquisition, an increased power budget may be required as the TEC unit contends with the day/night temperature variations as large as 30 °C [72].

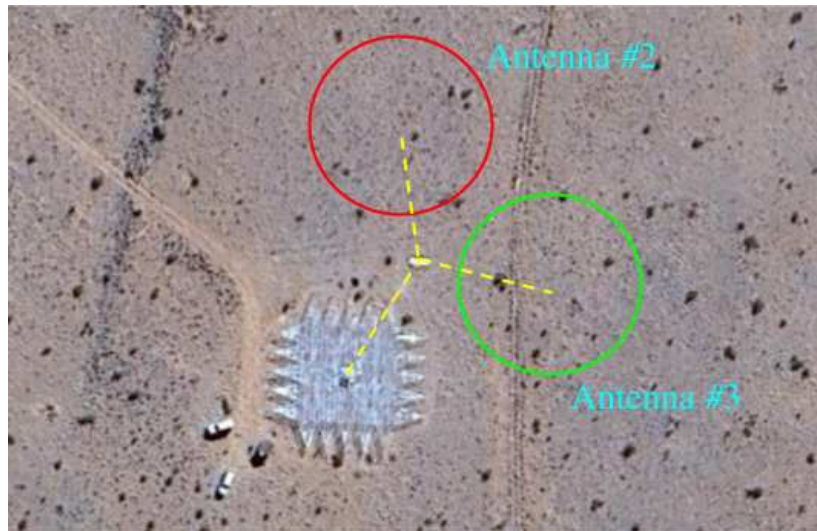


Fig. 5.1 A mock-up of the envisioned REACH experiment with potential sites of future antennas highlighted. Coloured circles represent a reasonable area needed for installation of an antenna along with its ground plane and separate receiver front-end unit. Antenna installations would all be located 100 metres (yellow dashed lines) from the singular receiver back-end unit and solar panel array seen at the image's centre. A conical log spiral antenna has been proposed as a second REACH installation. Various options for a third REACH installation are being explored including a scaled antenna for identification of systematics in observation data.

One final area of future work is the continued deployment of the REACH experiment. Currently, the receiver front- and back-ends as well as the hexagonal dipole installed at the deployment site. As detailed in chapter 2, the back-end has infrastructure to accommodate multiple antennas connected to independent receiver front-ends. A second receiver front-end is under construction in Cambridge following the specifications presented in this work with little modification. As detailed in de Lera Acedo et al. [20], simulations for a conical log spiral antenna have been completed for deployment following the current antenna-receiver system. Envisioned is an array of three antennas placed in a triangle configuration each connected to the single back-end and solar panel node as shown in fig. 5.1 It is thought that through the use of multiple antennas, redundant systematics and interference may be easily identified and removed. The experiment may also take advantage of the unique features attributed to different antenna designs such as the lower chromatic distortions of the conical log spiral versus the mechanical simplicity of the hexagonal dipole [2, 19, 20]. The inclusion of many antennas poses some concerns however such as the possible spawning of antenna crosstalk as present in the HERA experiment [32] in the form of correlation or interference between the three proposed antennas. Nevertheless, with appropriate precautions in place

and a robust calibration routine, the experiment may provide a unique window onto the early universe through the detection of the 21-cm hydrogen signature.

References

- [1] Abdurashidova, Z., Aguirre, J. E., Alexander, P., Ali, Z. S., Balfour, Y., Barkana, R., Beardsley, A. P., Bernardi, G., Billings, T. S., Bowman, J. D., Bradley, R. F., Bull, P., Burba, J., Carey, S., Carilli, C. L., Cheng, C., DeBoer, D. R., Dexter, M., de Lera Acedo, E., Dillon, J. S., Ely, J., Ewall-Wice, A., Fagnoni, N., Fialkov, A., Fritz, R., Furlanetto, S. R., Gale-Sides, K., Glendenning, B., Gorthi, D., Greig, B., Grobbelaar, J., Halday, Z., Hazelton, B. J., Heimersheim, S., Hewitt, J. N., Hickish, J., Jacobs, D. C., Julius, A., Kern, N. S., Kerrigan, J., Kittiwisit, P., Kohn, S. A., Kolopanis, M., Lanman, A., La Plante, P., Lekalake, T., Lewis, D., Liu, A., Ma, Y.-Z., MacMahon, D., Malan, L., Malgas, C., Maree, M., Martinot, Z. E., Matsetela, E., Mesinger, A., Mirocha, J., Molewa, M., Morales, M. F., Mosiane, T., Muñoz, J. B., Murray, S. G., Neben, A. R., Nikolic, B., Nunhokee, C. D., Parsons, A. R., Patra, N., Pieterse, S., Pober, J. C., Qin, Y., Razavi-Ghods, N., Reis, I., Ringuette, J., Robnett, J., Rosie, K., Santos, M. G., Sikder, S., Sims, P., Smith, C., Syce, A., Thyagarajan, N., Williams, P. K. G., and Zheng, H. (2022). HERA Phase I Limits on the Cosmic 21 cm Signal: Constraints on Astrophysics and Cosmology during the Epoch of Reionization. *The Astrophysical Journal*, 924(2):51.
- [2] Anstey, D., Cumner, J., de Lera Acedo, E., and Handley, W. (2022). Informing antenna design for sky-averaged 21-cm experiments using a simulated Bayesian data analysis pipeline. *Monthly Notices of the Royal Astronomical Society*, 509(4):4679–4693.
- [3] Anstey, D., de Lera Acedo, E., and Handley, W. (2021). A general Bayesian framework for foreground modelling and chromaticity correction for global 21 cm experiments. *Monthly Notices of the Royal Astronomical Society*, 506(2):2041–2058.
- [4] Anstey, D., de Lera Acedo, E., and Handley, W. (2023). Use of time dependent data in Bayesian global 21-cm foreground and signal modelling. *Monthly Notices of the Royal Astronomical Society*, 520(1):850–865.
- [5] Banerjee, S. (2009). Bayesian linear model: Gory details. Online.
- [6] Bauer, H. and Rothe, H. (1956). Der äquivalente rauschiverpol als wellenvierpol. *Arch elekt. Übertragung*, pages 241–252.
- [7] Bevins, H. T. J., Handley, W. J., Fialkov, A., de Lera Acedo, E., Greenhill, L. J., and Price, D. C. (2021). MAXSMOOTH: rapid maximally smooth function fitting with applications in Global 21-cm cosmology. *Monthly Notices of the Royal Astronomical Society*, 502(3):4405–4425.
- [8] Bilous, A. V., Kondratiev, V. I., Kramer, M., Keane, E. F., Hessels, J. W. T., Stappers, B. W., Malofeev, V. M., Sobey, C., Breton, R. P., Cooper, S., Falcke, H., Karastergiou,

- A., Michilli, D., Oslowski, S., Sanidas, S., ter Veen, S., van Leeuwen, J., Verbiest, J. P. W., Weltevrede, P., Zarka, P., Grießmeier, J.-M., Serylak, M., Bell, M. E., Broderick, J. W., Eisloffel, J., Markoff, S., and Rowlinson, A. (2016). A lofar census of non-recycled pulsars: average profiles, dispersion measures, flux densities, and spectra. *Astronomy & Astrophysics*, 591:A134.
- [9] Borlaff, A., Trujillo, I., Román, J., Beckman, J. E., Eliche-Moral, M. C., Infante-Sáinz, R., Lumbrales-Calle, A., de Almagro, R. T. S. M., Gómez-Guijarro, C., Cebrián, M., Dorta, A., Cardiel, N., Akhlaghi, M., and Martínez-Lombilla, C. (2019). The missing light of the Hubble Ultra Deep Field. *Astronomy & Astrophysics*, 621:A133.
- [10] Bouwens, R. J., Illingworth, G. D., Oesch, P. A., Stiavelli, M., van Dokkum, P., Trenti, M., Magee, D., Labbé, I., Franx, M., Carollo, C. M., and Gonzalez, V. (2010). Discovery of $z \approx 8$ galaxies in the hubble ultra deep field from ultra-deep wfc3/ir observations. *The Astrophysical Journal Letters*, 709(2):L133–L137.
- [11] Bowman, J. D., Morales, M. F., and Hewitt, J. N. (2007). Constraints on Fundamental Cosmological Parameters with Upcoming Redshifted 21 cm Observations. *The Astrophysical Journal*, 661(1):1–9.
- [12] Bowman, J. D. and Rogers, A. E. E. (2010a). A lower limit of $\Delta z > 0.06$ for the duration of the reionization epoch. *Nature*, 468(7325):796–798.
- [13] Bowman, J. D. and Rogers, A. E. E. (2010b). A lower limit of $\Delta z > 0.06$ for the duration of the reionization epoch. *Nature*, pages 796–798.
- [14] Bowman, J. D., Rogers, A. E. E., and Hewitt, J. N. (2008). Toward Empirical Constraints on the Global Redshifted 21 cm Brightness Temperature During the Epoch of Reionization. *The Astrophysical Journal*, 676(1):1–9.
- [15] Bowman, J. D., Rogers, A. E. E., Monsalve, R. A., Mozdzen, T. J., and Mahesh, N. (2018). An absorption profile centred at 78 megahertz in the sky-averaged spectrum. *Nature*, 555(7694):67–70.
- [16] Burns, J., Bale, S., Bradley, R., Ahmed, Z., Allen, S. W., Bowman, J., Furlanetto, S., MacDowell, R., Mirocha, J., Nhan, B., Pivovaroff, M., Pulupa, M., Rapetti, D., Slosar, A., and Tauscher, K. (2021). Global 21-cm Cosmology from the Far-side of the Moon. arXiv 2103.05085.
- [17] Canright, S. and Dunbar, B. (2003). Telescope history.
- [18] Cohen, A., Fialkov, A., Barkana, R., and Lotem, M. (2017). Charting the parameter space of the global 21-cm signal. *Monthly Notices of the Royal Astronomical Society*, 472(2):1915–1931.
- [19] Cummer, J., de Lera Aedo, E., de Villiers, D. I. L., Anstey, D., Kolitsidas, C. I., Gurdon, B., Fagnoni, N., Alexander, P., Bernardi, G., Bevins, H. T. J., Carey, S., Cavillot, J., Chiello, R., Craeye, C., Croukamp, W., Ely, J. A., Fialkov, A., Gessey-Jones, T., Gueuning, Q., Handley, W., Hills, R., Josaitis, A. T., Kulkarni, G., Magro, A., Maiolino, R., Meerburg, P. D., Mittal, S., Pritchard, J. R., Puchwein, E., Razavi-Ghods, N., Roque, I. L. V., Saxena, A., Scheutwinkel, K. H., Shen, E., Sims, P. H., Smirnov, O., Spinelli, M., and Zarb-Adami,

- K. (2022). Radio Antenna Design for Sky-Averaged 21cm Cosmology Experiments: The REACH Case. *Journal of Astronomical Instrumentation*, 11(1):2250001–2058.
- [20] de Lera Aedo, E., de Villiers, D. I. L., Razavi-Ghods, N., Handley, W., Fialkov, A., Magro, A., Anstey, D., Bevins, H. T. J., Chiello, R., Cumner, J., Josaitis, A. T., Roque, I. L. V., Sims, P. H., Scheutwinkel, K. H., Alexander, P., Bernardi, G., Carey, S., Cavillot, J., Croukamp, W., Ely, J. A., Gessey-Jones, T., Gueuning, Q., Hills, R., Kulkarni, G., Maiolino, R., Meerburg, P. D., Mittal, S., Pritchard, J. R., Puchwein, E., Saxena, A., Shen, E., Smirnov, O., Spinelli, M., and Zarb-Adami, K. (2022). The REACH radiometer for detecting the 21-cm hydrogen signal from redshift $z \approx 7.5\text{--}28$. *Nature Astronomy*, 6:984–998.
- [21] DeBoer, D. R., Parsons, A. R., Aguirre, J. E., Alexander, P., Ali, Z. S., Beardsley, A. P., Bernardi, G., Bowman, J. D., Bradley, R. F., Carilli, C. L., Cheng, C., de Lera Aedo, E., Dillon, J. S., Ewall-Wice, A., Fadana, G., Fagnoni, N., Fritz, R., Furlanetto, S. R., Glendenning, B., Greig, B., Grobbelaar, J., Hazelton, B. J., Hewitt, J. N., Hickish, J., Jacobs, D. C., Julius, A., Kariseb, M., Kohn, S. A., Lekalake, T., Liu, A., Loots, A., MacMahon, D., Malan, L., Malgas, C., Maree, M., Martinot, Z., Mathison, N., Matsetela, E., Mesinger, A., Morales, M. F., Neben, A. R., Patra, N., Pieterse, S., Pober, J. C., Razavi-Ghods, N., Ringuette, J., Robnett, J., Rosie, K., Sell, R., Smith, C., Syce, A., Tegmark, M., Thyagarajan, N., Williams, P. K. G., and Zheng, H. (2017). Hydrogen Epoch of Reionization Array (HERA). *Publications of the Astronomical Society of the Pacific*, 129(974):045001.
- [22] Dewdney, P. E., Hall, P. J., Schilizzi, R. T., and Lazio, T. J. L. W. (2009). The Square Kilometre Array. *IEEE Proceedings*, 97(8):1482–1496.
- [23] Dicke, R. H. (1946). The measurement of thermal radiation at microwave frequencies. *Review of Scientific Instruments*, 17:268.
- [24] Ewall-Wice, A., Chang, T. C., Lazio, J., Doré, O., Seiffert, M., and Monsalve, R. A. (2018). Modeling the Radio Background from the First Black Holes at Cosmic Dawn: Implications for the 21 cm Absorption Amplitude. *The Astrophysical Journal*, 868(1):63.
- [25] Fialkov, A., Barkana, R., Pinhas, A., and Visbal, E. (2014). Complete history of the observable 21 cm signal from the first stars during the pre-reionization era. *Monthly Notices of the Royal Astronomical Society*, 437(1):L36–L40.
- [26] Field, G. B. (1958). Excitation of the Hydrogen 21-CM Line. *Proceedings of the IRE*, 46:240–250.
- [27] Furlanetto, S. R., Lidz, A., Loeb, A., McQuinn, M., Pritchard, J. R., Alvarez, M. A., Backer, D. C., Bowman, J. D., Burns, J. O., Carilli, C. L., Cen, R., Cooray, A., Gnedin, N., Greenhill, L. J., Haiman, Z., Hewitt, J. N., Hirata, C. M., Lazio, J., Mesinger, A., Madau, P., Morales, M. F., Oh, S. P., Peterson, J. B., Pihlström, Y. M., Shapiro, P. R., Tegmark, M., Trac, H., Zahn, O., and Zaldarriaga, M. (2009). Astrophysics from the Highly-Redshifted 21 cm Line. In *astro2010: The Astronomy and Astrophysics Decadal Survey*, volume 2010, page 83.

- [28] Gessey-Jones, T., Fialkov, A., de Lera Acedo, E., Handley, W. J., and Barkana, R. (2023). Signatures of cosmic ray heating in 21-cm observables. *Monthly Notices of the Royal Astronomical Society*, 526(3):4262–4284.
- [29] Handley, W. (2018). fgivenx: A python package for functional posterior plotting. *The Journal of Open Source Software*, 3(28):849.
- [30] Hills, R., Kulkarni, G., Meerburg, P. D., and Puchwein, E. (2018). Concerns about modelling of the EDGES data. *Nature*, 564(7736):E32–E34.
- [31] Jonas, J. L. (2009). MeerKAT - The South African Array With Composite Dishes and Wide-Band Single Pixel Feeds. *IEEE Proceedings*, 97(8):1522–1530.
- [32] Kern, N. S., Parsons, A. R., Dillon, J. S., Lanman, A. E., Liu, A., Bull, P., Ewall-Wice, A., Abdurashidova, Z., Aguirre, J. E., Alexander, P., Ali, Z. S., Balfour, Y., Beardsley, A. P., Bernardi, G., Bowman, J. D., Bradley, R. F., Burba, J., Carilli, C. L., Cheng, C., DeBoer, D. R., Dexter, M., de Lera Acedo, E., Fagnoni, N., Fritz, R., Furlanetto, S. R., Glendenning, B., Gorthi, D., Greig, B., Grobbelaar, J., Halday, Z., Hazelton, B. J., Hewitt, J. N., Hickish, J., Jacobs, D. C., Julius, A., Kerrigan, J., Kittiwisit, P., Kohn, S. A., Kolopanis, M., La Plante, P., Lekalake, T., MacMahon, D., Malan, L., Malgas, C., Maree, M., Martinot, Z. E., Matsetela, E., Mesinger, A., Molewa, M., Morales, M. F., Mosiane, T., Murray, S. G., Neben, A. R., Parsons, A. R., Patra, N., Pieterse, S., Pober, J. C., Razavi-Ghods, N., Ringuette, J., Robnett, J., Rosie, K., Sims, P., Smith, C., Syce, A., Thyagarajan, N., Williams, P. K. G., and Zheng, H. (2020). Mitigating Internal Instrument Coupling for 21 cm Cosmology. II. A Method Demonstration with the Hydrogen Epoch of Reionization Array. *The Astrophysical Journal*, 888(2):70.
- [33] Kohn, S. A. (2015). The hera rfi environment. Technical report, University of Pennsylvania. internal memo.
- [34] Leeney, S. A. K., Handley, W. J., and de Lera Acedo, E. (2023). A Bayesian approach to RFI mitigation. *Physical Review D*, 108:062006.
- [35] Liu, A. and Shaw, J. R. (2020). Data Analysis for Precision 21 cm Cosmology. *Publications of the Astronomical Society of the Pacific*, 132(1012):062001.
- [36] Loeb, A. and Zaldarriaga, M. (2004). Measuring the Small-Scale Power Spectrum of Cosmic Density Fluctuations through 21cm Tomography Prior to the Epoch of Structure Formation. *Physical Review Letters*, 92(21):211301.
- [37] Mao, Y., Tegmark, M., McQuinn, M., Zaldarriaga, M., and Zahn, O. (2008). How accurately can 21cm tomography constrain cosmology? *Physical Review D*, 78(2):023529.
- [38] Mesinger, A. (2016). *Understanding the Epoch of Cosmic Reionization Challenges and Progress*. Springer International Publishing.
- [39] Mesinger, A. (2020). *The Cosmic 21 Cm Revolution: Charting the First Billion Years of Our Universe*. Institute of Physics Publishing.
- [40] Meys, R. (1978). A wave approach to the noise properties of linear microwave devices. *IEEE Transactions on Microwave Theory and Techniques*, 26(1):34–37.

- [41] Mirocha, J. and Furlanetto, S. R. (2019). What does the first highly redshifted 21-cm detection tell us about early galaxies? *Monthly Notices of the Royal Astronomical Society*, 483(2):1980–1992.
- [42] Monsalve, R. A., Altamirano, C., Bidula, V., Bustos, R., Bye, C. H., Chiang, H. C., Diaz, M., Fernandez, B., Guo, X., Hendrickson, I., Hornecker, E., Lucero, F., Mani, H., McGee, F., Mena, F. P., Pessoa, M., Prabhakar, G., Restrepo, O., Sievers, J. L., and Thyagarajan, N. (2023). Mapper of the IGM Spin Temperature (MIST): Instrument Overview. arXiv 2309.02996.
- [43] Monsalve, R. A., Rogers, A. E. E., Bowman, J. D., and Mozdzen, T. J. (2017). Calibration of the EDGES High-band Receiver to Observe the Global 21 cm Signature from the Epoch of Reionization. *The Astrophysical Journal*, 835(1):49.
- [44] Mozdzen, T. J., Bowman, J. D., Monsalve, R. A., and Rogers, A. E. E. (2016). Limits on foreground subtraction from chromatic beam effects in global redshifted 21 cm measurements. *Monthly Notices of the Royal Astronomical Society*, 455(4):3890–3900.
- [45] Murray, S. G., Bowman, J. D., Sims, P. H., Mahesh, N., Rogers, A. E. E., Monsalve, R. A., Samson, T., and Vydula, A. K. (2022). A Bayesian calibration framework for EDGES. *Monthly Notices of the Royal Astronomical Society*, 517(2):2264–2284.
- [46] Nagel, J. B. (2017). *Bayesian techniques for inverse uncertainty quantification*. PhD thesis, ETH Zurich.
- [47] Naldi, G., Mattana, A., Pastore, S., Alderighi, M., Zarb Adami, K., Schillirò, F., Aminaei, A., Baker, J., Belli, C., Comoretto, G., Chiarucci, S., Chiello, R., D’Angelo, S., Dalle Mura, G., De Marco, A., Halsall, R., Magro, A., Monari, J., Roberts, M., Perini, F., Poloni, M., Pupillo, G., Rusticelli, S., Schiaffino, M., and Zaccaro, E. (2017). The Digital Signal Processing Platform for the Low Frequency Aperture Array: Preliminary Results on the Data Acquisition Unit. *Journal of Astronomical Instrumentation*, 6(1):1641014.
- [48] National Academy of Sciences (2021). *Pathways to Discovery in Astronomy and Astrophysics for the 2020s*. The National Academies Press, Washington D.C.
- [49] Orloff, J. and Bloom, J. (2013). Conjugate priors: Beta and normal. Online.
- [50] Parsons, A. R. et al. (2010). The precision array for probing the epoch of reionization: 8 station results. arXiv 0904.2334.
- [51] Patra, N., Subrahmanyan, R., Sethi, S., Shankar, N. U., and Raghunathan, A. (2015). Saras measurement of the radio background at long wavelengths. *The Astrophysical Journal*, 801(2).
- [52] Penfield, P. (1962). Wave representation of amplifier noise. *IRE Transactions on Circuit Theory*, pages 84–86.
- [53] Philip, L., Abdurashidova, Z., Chiang, H. C., Ghazi, N., Gumba, A., Heilgendorff, H. M., Jáuregui-García, J. M., Malepe, K., Nunhokee, C. D., Peterson, J., Sievers, J. L., Simes, V., and Spann, R. (2019). Probing Radio Intensity at High-Z from Marion: 2017 Instrument. *Journal of Astronomical Instrumentation*, 8(2):1950004.

- [54] Pozar, D. M. (2012). *Microwave Engineering*. John Wiley & Sons, New York.
- [55] Price, D. C. et al. (2018). Design and characterization of the large-aperture experiment to detect the dark age (LEDA) radiometer systems. *Monthly Notices of the Royal Astronomical Society*, 478(3).
- [56] Pritchard, J. and Loeb, A. (2010). Cosmology: Hydrogen was not ionized abruptly. *Nature*, 468(7325):772–773.
- [57] Pritchard, J. R. and Loeb, A. (2012). 21 cm cosmology in the 21st century. *Reports on Progress in Physics*, 75.
- [58] Rogers, A. E. E. and Bowman, J. D. (2012). Absolute calibration of a wideband antenna and spectrometer for accurate sky noise temperature measurements. *Radio Science*, 47(4):RS0K06.
- [59] Rothe, H. and Dahlke, W. (1956). Theory of noisy fourpoles. *Proceedings of the IRE*, 44:811–818.
- [60] Ryden, B. (2002). *Introduction to Cosmology*. Pearson.
- [61] Shaver, P. A., Windhorst, R. A., Madau, P., and de Bruyn, A. G. (1999). Can the reionization epoch be detected as a global signature in the cosmic background? *Astronomy and Astrophysics*, 345:380–390.
- [62] Sims, P. H. and Pober, J. C. (2020). Testing for calibration systematics in the EDGES low-band data using Bayesian model selection. *Monthly Notices of the Royal Astronomical Society*, 492(1):22–38.
- [63] Singh, S., Jishnu, N. T., Subrahmanyam, R., Udaya Shankar, N., Girish, B. S., Raghunathan, A., Somashekar, R., Srivani, K. S., and Sathyanaarayana Rao, M. (2022). On the detection of a cosmic dawn signal in the radio background. *Nature Astronomy*, 6:607–617.
- [64] Singh, S., Subrahmanyam, R., Udaya Shankar, N., Sathyanaarayana Rao, M., Fialkov, A., Cohen, A., Barkana, R., Girish, B. S., Raghunathan, A., Somashekar, R., and Srivani, K. S. (2018). SARAS 2 Constraints on Global 21 cm Signals from the Epoch of Reionization. *The Astrophysical Journal*, 858(1):54.
- [65] Smith, R. C. (1995). *Observational Astrophysics*. Cambridge University Press, Cambridge, England.
- [66] Sokolowski, M., Tremblay, S. E., Wayth, R. B., Tingay, S. J., Clarke, N., Roberts, P., Waterson, M., Ekers, R. D., Hall, P., Lewis, M., Mossammaparast, M., Padhi, S., Schlegelhauer, F., Sutinjo, A., and Tickner, J. (2015). BIGHORNS - Broadband Instrument for Global HydrOgen Reionisation Signal. *Publications of the Astronomical Society of Australia*, 32:e004.
- [67] Trotta, R. (2008). Bayes in the sky: Bayesian inference and model selection in cosmology. *Contemporary Physics*, 49(2):71–104.
- [68] van Haarlem, M. P. et al. (2013). LOFAR: The LOw-Frequency ARray. *Astronomy & Astrophysics*, 556:A2.

- [69] Visbal, E., Barkana, R., Fialkov, A., Tseliakhovich, D., and Hirata, C. M. (2012). The signature of the first stars in atomic hydrogen at redshift 20. *Nature*, 487:70–73.
- [70] Voytek, T. C., Natarajan, A., Jáuregui García, J. M., Peterson, J. B., and López-Cruz, O. (2014). Probing the Dark Ages at $z \sim 20$: The SCI-HI 21 cm All-sky Spectrum Experiment. *The Astrophysical Journal*, 782(1):L9.
- [71] Weinert, H. L. (2009). A fast compact algorithm for cubic spline smoothing. *Computational Statistics and Data Analysis*, 53(4):932–940.
- [72] Werger, M. (1978). *Biogeographical Divisions of Southern Africa*. W. Junk, The Hague.
- [73] Wouthuysen, S. A. (1952). On the excitation mechanism of the 21-cm (radio-frequency) interstellar hydrogen emission line. *The Astrophysical Journal*, 57:31–32.
- [74] Zhang, Y., Tiňo, P., Leonardis, A., and Tang, K. (2021). A Survey on Neural Network Interpretability. *IEEE Transactions on Emerging Topics in Computational Intelligence*, 5:729–742.

Appendix A

Supplementary Data

Instrumentation

Switch name	Model (Mini-Circuits)	Connection
MS1	12V MSP8TA-12-12D+	Calibration sources
MS2	24V MSP6TA-12D+	VNA path/calibration components
MS3	UNKNOWN	2 metre cable terminations
MS4	UNKNOWN	10 metre cable terminations
MTS	24V MTS-18XL-B+	Spectrometer/VNA signal path

Table A.1 Switch model number and connections from within the receiver front-end for reference.

Switch	Position	Contents
MS1	1	Antenna
MS1	2	Heated 50Ω load
MS1	3	Reference noise source (diode)
MS1	4	Ambient 50Ω (cold) load
MS1	5	Ambient 25Ω load
MS1	6	Ambient 100Ω load
MS1	7	2 metre calibration cable
MS1	8	10 metre calibration cable
MS2	1	MTS position 1 (towards calibration sources)
MS2	2	MTS position 3 (towards spectrometer path)
MS2	3	VNA calibration short
MS2	4	VNA calibration open
MS2	5	VNA calibration 50Ω load
MS2	6	VNA verification 50Ω test load
MS3	1	36Ω load
MS3	2	27Ω load
MS3	3	69Ω load
MS3	4	91Ω load
MS4	1	Open termination
MS4	2	Shorted termination
MS4	3	10Ω load
MS4	4	250Ω load
MTS	1	MS2 position 1 (calibration sources to VNA)
MTS	2	MS1 (towards calibration sources)
MTS	3	MS2 position 2 (LNA to VNA)
MTS	4	Towards LNA (sources to spectrometer)

Table A.2 The content of each switch position for easy reference. This chart represents the receiver component positions at the time of the December 2022 deployment.

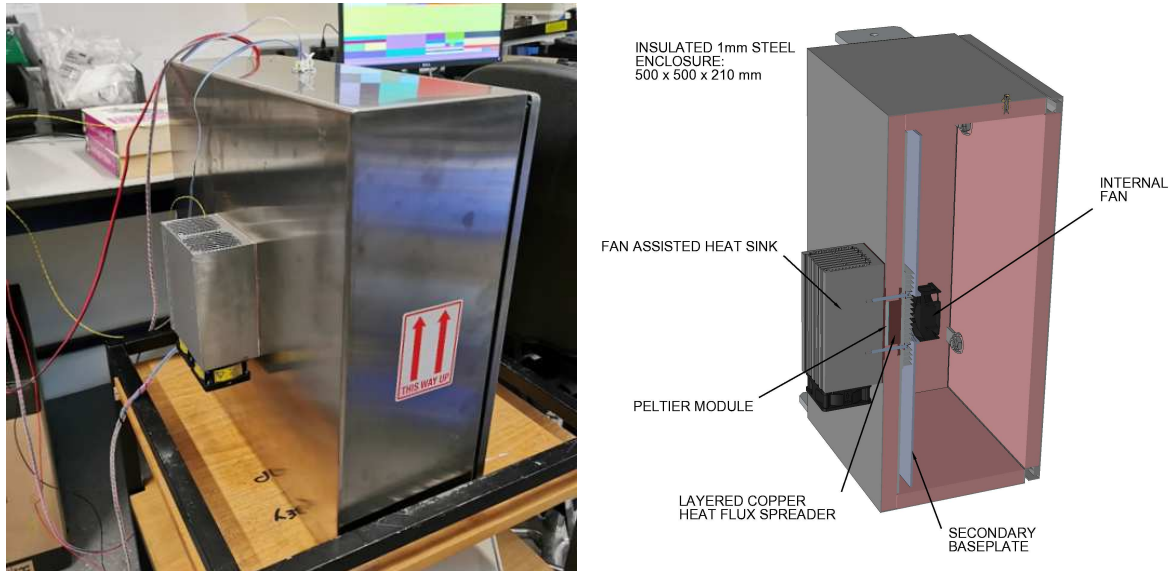


Fig. A.1 The completed front-end thermal enclosure is shown on the left. A 3D-rendered cross section in a similar orientation is shown on the right depicting the internal fan, baseplate, Peltier module and heat sink configuration.

Power supply	Switchable	Component
3.3 V	No	Teensy 3.5 Development Board
5 V	No	Fibre to USB converter
6 V (A)	Yes	Low noise amplifier
6 V (B)	Yes	Low noise amplifier
12 V	Yes	VNA, RF switches
24 V	Yes	Internal fan, RF switches
28 V	Yes	Noise source diode

Table A.3 Power supply considerations for the front-end receiver managed by the micro-controller unit. The ability to toggle the 5 V supply was disabled at the hardware-level in order to prevent accidental user activation which would result in a (catastrophic) completely non-responsive instrument.

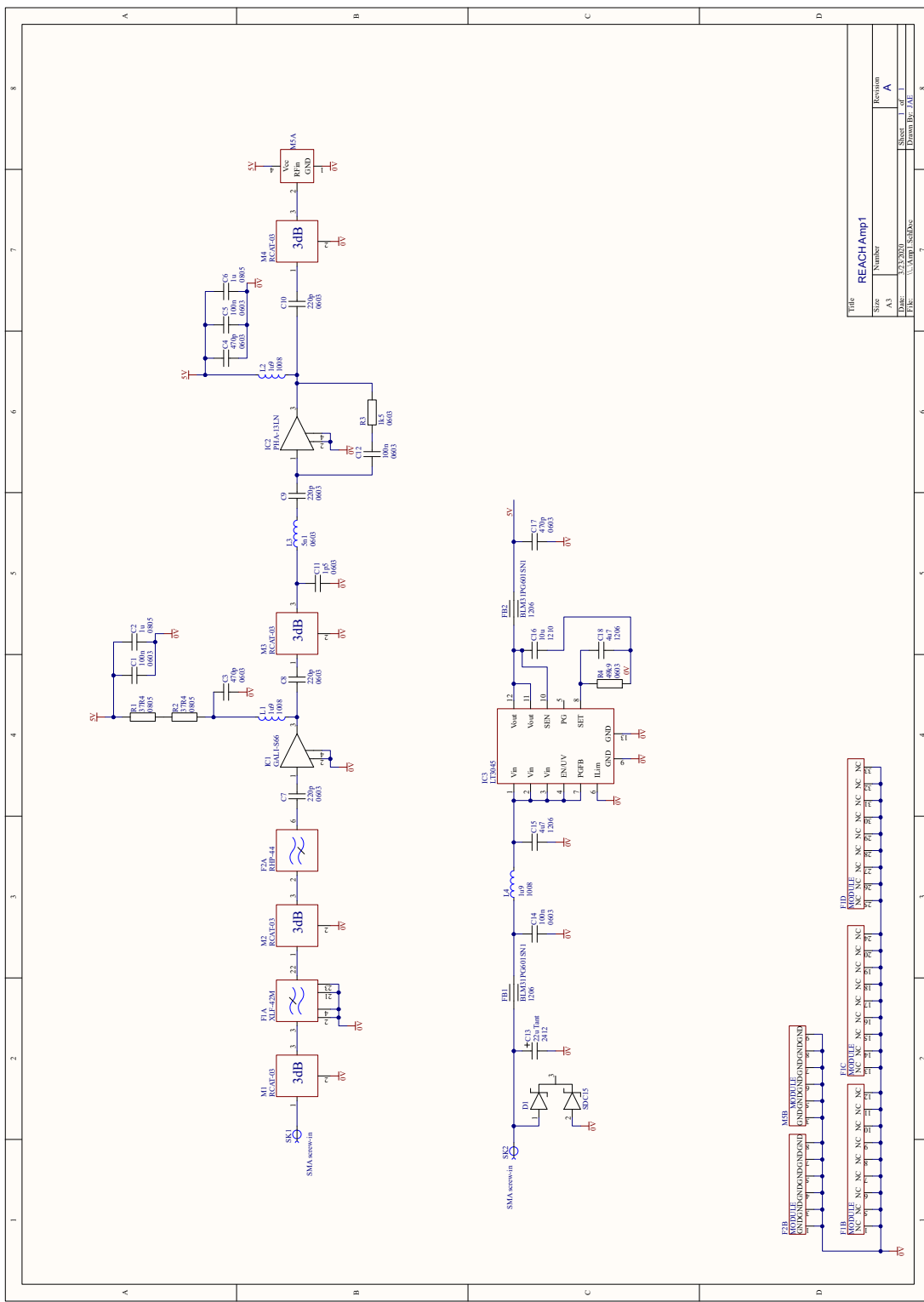


Fig. A.2 Full circuit diagram for amplifier #1 in the REACH receiver front-end. Credit: John A. Ely and Nima Razavi-Ghods.

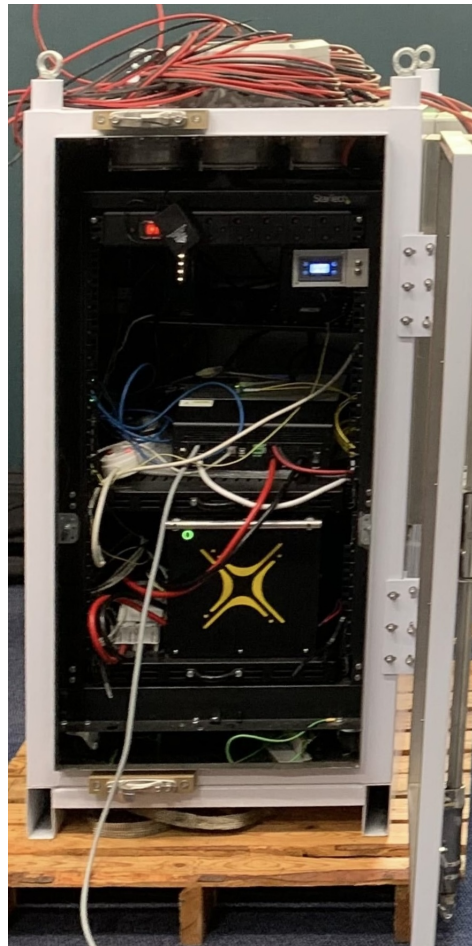


Fig. A.3 The smaller RF-EMC chamber accompanying the receiver back-end. This chamber houses various additional units for overnight power storage from the solar panels. The black module adorned with the yellow "X" symbol is the Solar MD SS202 Lithium Iron Phosphate battery.

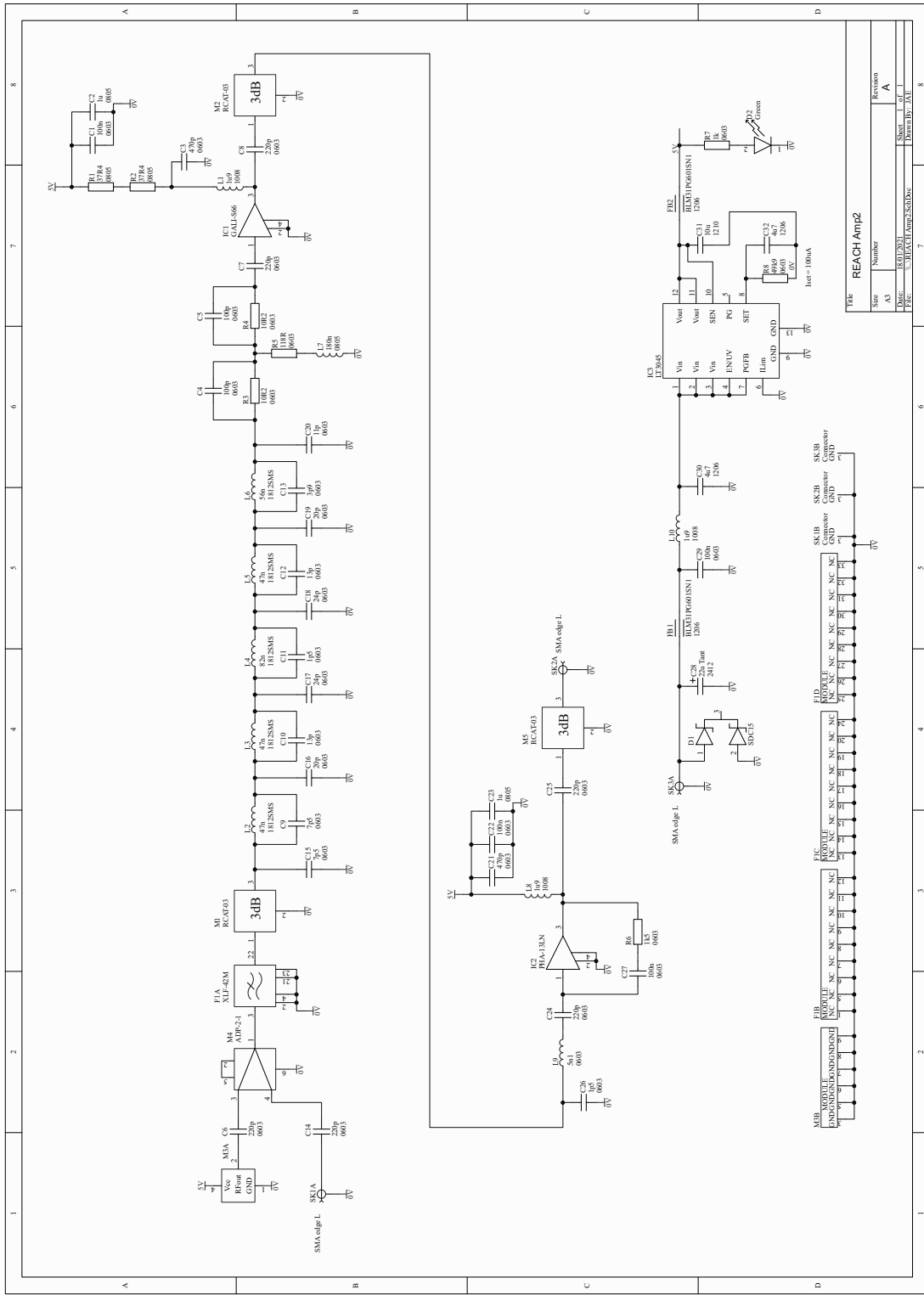


Fig. A.4 Full circuit diagram for amplifier #2 in the REACH receiver back-end. Credit: John A. Ely and Nima Razavi-Ghods.

Port Number	Device
7–24 V DC GND	
Port 0	Penn Elcom FT01-Q Cooling rack
Port 1	Lenovo ThinkCentre server
Port 2	ATEN CL6700 MW KVM module
Port 3	Netgear ProSafe M4100-D12G Ethernet switch
Port 4	Icron 2244 USB Ranger
Port 5	Unused
Port 6	Unused
Port 7	Readout system TEC controller USB connection
Port 8	Unused
Port 9	Unused
Port 10	Unused

Table A.4 Receiver back-end StarTech USB hub connections.

Port Number	Device
Port 1	Unused
Port 2	Readout system Ethernet output
Port 3	Unused
Port 4	Unused
Port 5	Unused
Port 6	Unused
Port 7	Lenovo ThinkCentre Ethernet input
Port 8	Unused
Port 9	Unused
Port 10	Unused
Port 11	Unused
Port 12	Tripp Lite PDUMH15HVNET power distribution unit

Table A.5 Receiver back-end Netgear ProSafe M4100-D12G Ethernet switch connections.

Port Number	Device
Port 1	Penn Elcom FT01-Q cooling rack
Port 2	Netgear ProSafe M4100-D12G Ethernet switch (power connection)
Port 3	Lenovo ThinkCentre
Port 4	Icron 2244 USB Ranger
Port 5	Trimble Thunderbolt E GPS disciplined clock
Port 6	Readout enclosure power
Port 7	Second back-end power distribution unit
Port 8	ATEN CL6700 MW KVM module
Ethernet port	Netgear ProSafe M4100-D12G Ethernet switch (Ethernet connection)

Table A.6 Receiver back-end Tripp Lite PDUMH15HVNET power distribution unit connections.

Frequency	Magnitude
100 MHz	71 dB
200 MHz	69 dB
500 MHz	61 dB
1 GHz	48 dB
2 GHz	32 dB
3 GHz	23.5 dB
4 GHz	15.5 dB

Table A.7 Voltage gain (S_{21}) for the custom built low noise amplifier used during initial calibration experiments detailed in section 4.1.

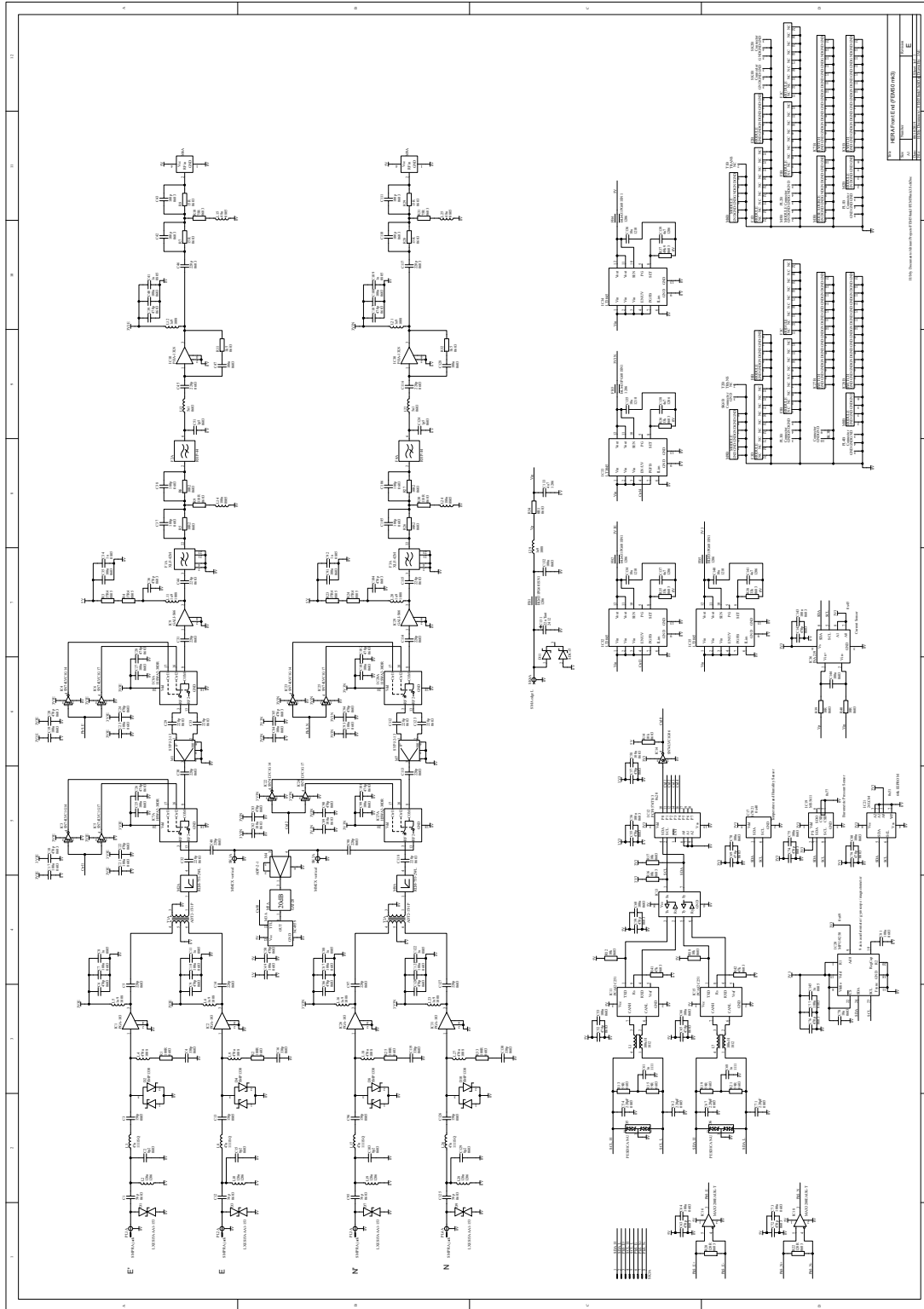


Fig. A.5 Full circuit diagram for the HERA Front End Module mk III shown for reference.
Credit: John A. Ely and Nima Razavi-Ghods.

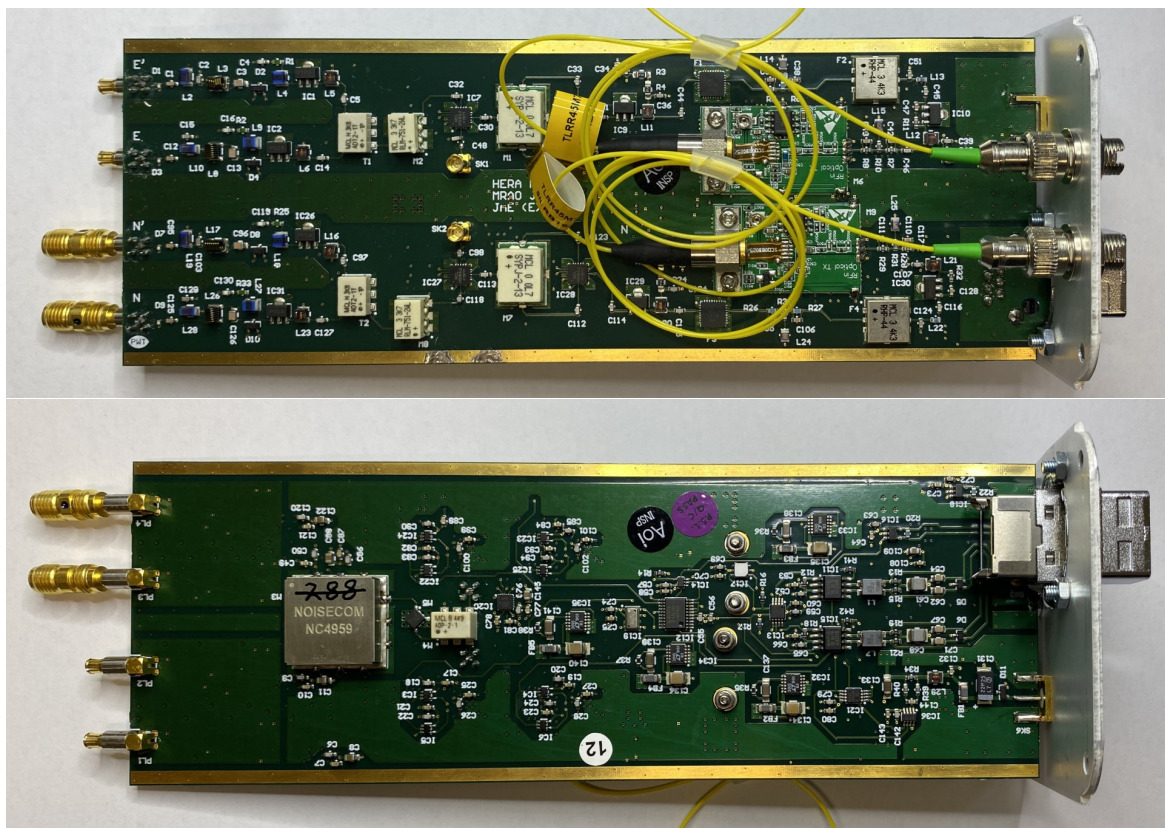


Fig. A.6 The front and back of an unaltered HERA FEM board without its housing.